Numerical prediction of nanoparticle formation in flames

Dissertation

zur Erlangung des akademischen Grades

Doktoringenieur

(Dr.-Ing.)

von **M.Tech. Thirumalesha Chittipotula**

geb.am 02 July 1980 in Bhongir, Indien

genehmigt durch die Fakultät für Verfahrens- und Systemtechnik

der Otto-von-Guericke-Universität, Magdeburg

Gutachter: Prof. Dr.-Ing. Dominique Thévenin
Prof. Dr.-Ing. Fabian Mauß
Prof. Dr.-Ing. Mirko Peglow

Promotionskolloquium am : 26^{th} Oct. 2012

To my

Mother

Acknowledgement

It gives me immense pleasure to thank everyone who have directly and indirectly helped and motivated me all through the journey of my PhD. I extend my heartfelt gratitude to Prof. Dominique Thévenin, an inspiring personality and one of the best guides I happened to come across. I have learnt much more things by merely observing him than speaking to him. His outstanding guidance and support in technical as well as in my career prospects has been extremely helpful.

I convey my sincere thanks to Dr. Gábor Janiga who is easily accessible. His help in all technical applications including CFD was extremely beneficial, particularly during initial stages of my work. I extend my sincere thanks to Prof. Peglow, Prof. Marchisio and Dr. Alper Öncül for the thought-provoking discussions and for their help on PBE, QMOM and DQMOM. I am thankful to all my fellow doctoral colleagues both from LSS and IMPRS for all the lively discussions.

I thank the Faculty of Process and Systems Engineering of the Otto-von-Guericke-Universität, Magdeburg for providing all the facilities required to carry out my research. My sincere thanks to International Max Planck Research School (IMPRS) in Magdeburg for financing my doctoral study. The life would not have been so easy as it is now without Dr. Barbara Witter. I would like to acknowledge her help in all IMPRS matters and VISA related works.

It always gives me a sense of happiness and responsibility when I recollect all the support and the contribution of my family members. I am greatly indebted to my mother Jayamma, brother Sridhar, vadina (Suvarna), sisters (Sumathi, Srivani) and brothers-in-law (Narsimha, Upender). I am sure that my gratitude shown here would not be sufficient to equate their warm-hearted embrace all the way of my journey. I thank God for all the invaluable smiles of wonderful kids in our family.

I am very thankful to Satya Sekhar, Kasyap and Gayathri for proof reading a few chapters of my thesis. I thank all my friends here in Magdeburg, India and in the US for their best wishes. Anil, Bablu, Raj Kumar, Kanthu, Sambu, Subbu, Chitti kanna, Swami Rao, Koti, Suku, Santhosh, Polu, Manju, Raman, Ashok, Jim, Ganesh, Rayees, Subbru, Yash, Luis, Subba Rayudu, Naresh babu, Dileep and Rokkam with whom I always enjoyed the company and warmth of their friendship.

Finally, I would like to thank my wife Lakshmi for her love, support and caring hand.

Abstract

Objective of the present study is to accurately model nanoparticle formation in flames and improve existing physico-chemical models involved in the particulate phase. First and major part of the current study involved prediction of soot particle formation in turbulent ethylene/air non-premixed flames. In a second part, synthesis of TiO_2 nanoparticles is investigated in methane/oxygen diffusion flames with titanium tetraisopropoxide (TTIP) as precursor.

When considering soot formation in practical burners, semi-empirical models are mostly used. But existing soot models for non-premixed ethylene/air flames often do not satisfactorily predict soot volume fraction (f_v), the key engineering quantity for most applications. Due to intense energy exchange by radiative heat transfer, this leads to a situation where even basic scalar fields like temperature are inaccurately described. The objective of the present study is to develop an enhanced soot prediction model for such flames, valid for a wide range of flow and operating conditions. The emphasis in this work is specifically on the particulate phase and not on gas-phase kinetics.

The evolution of soot particles is described by physical models accounting for nucleation, surface growth, aggregation and oxidation. The Direct Quadrature Method of Moments (DQMOM) is employed to solve the Population Balance Equations (PBE) in a computationally efficient manner, assuming a mono-variate PBE with particle diameter as internal coordinate.

The original soot model is optimized numerically by using Genetic Algorithms coupled with Computational Fluid Dynamics (CFD). The values of three model parameters, associated with nucleation, oxidation and soot particle radiation are optimized through comparison with recent experimental results. Two objective functions are formulated based on the difference between experimental and simulation results for temperature and f_v. After obtaining an optimal parameter set, the resulting model is further tested against three experimental configurations, leading to a good agreement and thus demonstrating a high level of generality. Nevertheless, a shift in the peak soot position towards the burner was systematically observed at first. This issue could be finally solved by refining the description of turbulence/chemistry coupling

using a flamelet model and adding another optimization parameter.

Radiative heat transfer is highly significant in combustion processes, especially for those involving soot. Due to the tight coupling of soot models with the temperature, it is essential to take into account radiative heat transfer associated with soot particles as well as with key gaseous species while keeping acceptable numerical complexity. In the present project, three simple soot radiation models based on grey gas and optically thin approximation have been analyzed, compared and optimized in an effort to further improve the particulate models previously developed. The final results are in slightly better agreement with all measured fields, demonstrating that optimization based on flow simulations can efficiently support the development of optimal physico-chemical models.

The second objective of the present numerical analysis is to investigate the production of TiO_2 nanoparticles with tailored mean properties in turbulent diffusion flames burning CH_4 in O_2, with titanium tetraisopropoxide (TTIP) as precursor and argon as carrier gas. Gas-phase chemistry is represented by considering a detailed CH_4-O_2 combustion mechanism with 17 species and 41 reactions. The Eddy Dissipation Concept (EDC) model is used to handle turbulence-chemistry interaction. A Monovariate Population Balance Equations (PBE) describing the TiO_2 nanoparticle evolution is implemented, taking into account nucleation, molecular growth and aggregation as source terms. The Quadrature Method of Moments (QMOM) is employed to solve this PBE.

Initially, simulations are performed for 3 different oxygen flow rates (2, 4, 6 L/min) to validate employed models and numerical approach against the experimental data presented in [1]. Peak value of temperature and consequently peak values of TTIP and TiO_2 concentrations are shifted towards the burner with increase in O_2 flow rate. It is also observed that as the O_2 flow rate increases, the peak value of temperature, decomposition rate of TTIP and TiO_2 nanoparticle diameter are systematically decreased.

The influence of various parameters involved in a published experimental configuration is then investigated in order to identify numerically the best possible set-up, delivering nanoparticles with lowest mean diameter (d_{mean}), highest volume fraction (f_v) and lowest standard deviation (narrowest size dis-

tribution, σ_g). For this purpose numerous simulations were performed, first interchanging the position of Ar, CH_4 and O_2 injections in the computational domain while keeping the burner configuration unchanged. In the second step, the best flow configuration identified in the first step has been kept whereas the burner dimensions (internal diameters) have been varied around their initial values while keeping the same mass flow rates of CH_4-O_2/TTIP/Ar. Compared to the original configuration, modified burner configurations are finally identified that produce lower particle mean diameter, higher volume fraction and narrower particle size distribution. It appears therefore possible to optimize nanoparticle generation in flames using numerical studies to obtain tailored properties.

For all numerical simulations, the industrial CFD solver *Ansys-Fluent* is used to solve the gas-phase governing equations, whereas the PBE is solved with in-house user-defined functions (UDF) coupled to the CFD solver.

Zusammenfassung

Gegenstand der vorliegenden Arbeit ist die exakte Modellierung der Nanopartikelformation in Flammen und die Verbesserung bestehender physikalisch-chemischer Modelle, die an der partikulären Phase beteiligt sind. Der erste Teil der Arbeit, der gleichzeitig den Schwerpunkt darstellt, behandelt die Vorhersage der Rußpartikelbildung in nicht vorgemischten turbulenten Ethylen-Luft-Flammen. Im zweiten Teil wird die Synthese von TiO_2 Nanopartikeln mit Titanium-Tetraisopropoxiden (TTIP) als Precursor in Methan-Sauerstoff Diffusionsflammen untersucht.

Bei der Berücksichtigung der Rußbildung in Brennern kommen hauptsächlich halbempirische Modelle zum Einsatz. Die existierenden Modelle für nicht vorgemischte Ethylen-Luft-Flammen sagen den Rußvolumenanteil (f_v), der als Schlüsselparameter in den meisten Anwendungen gilt, oft nicht sehr zufriedenstellend voraus. Aufgrund von sehr hohem Energieaustausch durch Wärmestrahlung kommt es zu einem Zustand, in dem selbst grundlegende Skalarfelder wie das der Temperatur sehr ungenau beschrieben werden. Die Zielstellung dieser Arbeit ist die Entwicklung eines verbesserten Rußvorhersagemodells, das für ein großes Spektrum an Flammen und Umgebungsbedingungen gültig ist. Der Schwerpunkt der Arbeit wird dabei eindeutig auf die partikuläre Phase und nicht auf die Gasphase gelegt.

Die Entwicklung von Rußpartikeln wird mit physikalischen Modellen beschrieben, in denen Keimbildung, Wachstum, Aggregation und Oxidation berechnet werden. Die Direct Quadrature Method of Moments (DQMOM) wird eingesetzt, um Populationsbilanzgleichungen (PBE) numerisch zu lösen, wobei eine mono-variate PBE angenommen wird, in der der Partikeldurchmesser als Ausgangsgröße dient. Das originale Rußmodell wird numerisch unter Nutzung von generischen Algorithmen optimiert, wobei diese mit Methoden der numerischen Strömungsmechanik (CFD) gekoppelt sind. Die Werte von drei Modellparametern, bezogen auf die Keimbildung, Oxidation und Rußpartikelstrahlung werden auf Grundlage eines Vergleichs mit experimentell verfügbaren Daten optimiert. Zwei Zielfunktionen werden formuliert, die sich auf die Differenzen der Temperatur und f_v zwischen experimentellen und simulierten Ergebnissen beziehen. Nach Erhalt eines optimalen Parametersatzes wird

das erzeugte Modell erneut an drei experimentellen Konfigurationen getestet. Dabei kann eine gute übereinstimmung und gleichzeitig ein hohes Maß an Allgemeingültigkeit gezeigt werden. Dennoch wurde zunächst eine Verschiebung des Rußscheitelwertes gegenüber dem Brenner beobachtet. Diese Problematik konnte schließlich durch eine Verfeinerung des Flammenmodells behoben werden, indem ein zusätzlicher Optimierungsparameter hinzugefügt wurde.

Wärmeübertragung durch Strahlung ist bei Verbrennungsprozessen von hoher Bedeutung, speziell bei solchen, in denen Ruß involviert ist. Durch die enge Kopplung zwischen den Rußmodellen und der Temperatur ist es notwendig die Wärmestrahlung bezogen auf die Rußpartikel und die die wichtigen Gasarten zu berücksichtigen. Dabei sollte die numerische Komplexität stets handhabbar gehalten werden. Im vorliegenden Projekt wurden drei einfache Rußstrahlungsmodelle analysiert, verglichen und zur Verbesserung des bereits entwickelten Modells optimiert. Die Ergebnisse weisen eine etwas bessere übereinstimmung mit allen gemessenen Feldern auf, wodurch gezeigt werden kann, dass mithilfe von Strömungsoptimierung die Entwicklung optimaler physikalisch chemischer Modelle möglich ist.

Die zweite Zielstellung dieser numerischen Analyse ist die Erforschung der Produktion von TiO_2 Nanopartikeln mit angepassten gemittelten Eigenschaften von turbulenten Diffusionsflammen, die CH_4 in O_2 verbrennen. Dabei dient Titanium Tetraisopropoxid (TTIP) als Precursor und Argon als Trägergas. Die Gasphasenchemie wird durch einen detaillierten CH_4-O_2 Verbrennungsprozess repräsentiert, wobei 17 Stoffe und 41 Reaktionen involviert sind. Das Wirbel-Dissipationskonzept (EDC) wird eingesetzt, um die Turbulenz-Chemie-Wechselwirkung zu berücksichtigen. Eine mono-variate Populationsbilanzgleichung (PBE), welche die TiO_2 Nanopartikelentwicklung beschreibt, wird implementiert, wobei die Keimbildung, das molekulare Wachstum und die Aggregation als Quellterme berücksichtigt werden. Die Quadrature Method of Moments (QMOM) kommt zum Einsatz, um die PBE zu lösen.

Anfangs werden die Simulationen mit drei verschiedene Sauerstoffvolumenströmen (2, 4, 6 L/min) durchgeführt, damit die numerischen Approximationen der entwickelten Modelle mit den in [1] präsentierten Experimentaldaten validiert werden können. Die Höchstwerte der Temperatur und daraus

abgeleitet die Höchstwerte TTIP- und TiO_2-Konzentration zeigen eine Verschiebung gegenüber dem Brenner mit steigendem O_2-Volumenstrom. Außerdem wird beobachtet, das mit zunehmenden O_2-Volumenstrom sich der Höchstwert der Temperatur, die Zersetzungsrate von TTIP und der TiO_2 Nanopartikeldurchmesser abnehmen.

Der Einfluss unterschiedlicher Parameter, die in einer experimentellen Konfiguration veröffentlich wurden, wird untersucht, um numerisch das bestmögliche Konzept zu identifizieren, das Nanopartikel mit dem niedrigsten mittleren Durchmesser (d_{mean}), dem höchsten Volumenanteil (f_v) und der geringsten Standardabweichung (kleinste Größenabweichung, σ_g) liefert. Zu diesem Zweck wurden zahlreiche Simulationen durchgeführt, wobei zunächst die Positionen der Ar, CH_4 und O_2 Injektionen unter gleichbleibender Brennerkonfiguration variiert wurde. Im zweiten Schritt wurde die beste aus Schritt 1 identifizierte Injektionskonfiguration verwendet, um die Brennerabmessungen zu verändern (interne Durchmesser). Dabei wurden die Volumenströme von CH_4-O_2/TTIP/Ar konstant gehalten. Verglichen mit der originalen Konfiguration wurden schließlich modifizierte Konfigurationen identifiziert, die Partikel mit einem geringeren mittleren Durchmesser, einem höheren Volumenanteil und einer schmaleren Größenverteilungen produzieren. Es scheint somit möglich zu sein, die Nanopartikelentwicklung in Flammen mithilfe von numerischen Methoden zu optimieren, um angepasste Eigenschaften zu erhalten.

Bei allen numerischen Simulationen wurde der industrielle CFD-Solver *Ansys-Fluent* verwendet, um die Gasphasengleichungen zu lösen. Für die Berechnung der PBE kam eine hauseigene benutzerdefinierte Funktion (UDF) zum Einsatz, die mit dem CFD-Solver gekoppelt wurde.

Nomenclature

Latin Symbols

A	particle surface area concentration, [m^2 m^{-3}]
a	source term for weights, [-]
a_s	absorption coefficient, [m^{-1}]
b	source term for abscissas, [-]
C	concentration, [mol m^{-3}]
C_0	radiation proportionality factor, [m^{-1} K^{-1}]
C_μ	$k-\epsilon$ model constant, 0.09 [-]
C_τ	EDC model parameter: time scale constant, [-]
C_γ	EDC model parameter: volume fraction constant, [-]
Da	Damköhler number, [-]
D_f	fractal dimension, [-]
D_i	internal nozzle diameter, [mm]
d	matrix of source terms of size 4×1 (in DQMOM), [-]
E	error for soot volume fraction, [-]
e	error for temperature, [-]
f	number density function, [m^{-3}]
f_v	soot volume fraction, [m^3 m^{-3}]
G_g, G_o	molecular & oxidation growth rates, [m s^{-1}]
g	acceleration due to gravity, [m s^{-2}]
ΔH	relative difference in peak values, [-]
h	specific enthalpy, [J kg^{-1}]
$\mathscr{J}$	enthalpy diffusive flux, [W m^{-2}]
J	nucleation rate, [m^{-3} s^{-1}]

Kn	Knudsen number, [-]
k	order of the moments, [-]
k_b	Boltzmann constant, [1.380×10^{-23} J K^{-1}]
k_f	fractal pre-factor, [-]
k_g	nucleation rate constant for TiO_2 particles from TTIP, [s^{-1}]
k_{ove}	overall rate constant for TTIP decomposition, [s^{-1}]
k_s	surface rate constant for TiO_2 particles from TTIP, [m s^{-1}]
k_v	characteristic shape pre-factor, [-]
L	abscissa of quadrature approximation (length), [m]
M	molecular weight, [kg kmol^{-1}]
$\dot{m}$	mass flow rate, [g/s]
m_k	kth moment of PSD, [variable]
N	number of quadrature nodes, [-]
N_A	Avogadro's number, [6.023×10^{23} mol^{-1}]
N_s	number of delta functions or internal co-ordinates, [-]
$OF1$	first objective function, [-]
$OF2$	second objective function, [-]
p	pressure, [Pa]
Q	heat, [W m^{-2}]
Q_{rad}	radiative heat transfer, [W m^{-3}]
R_c	particle collision radius, [m]
Re	Reynolds number, [-]
S	Source term, [-]
Sc	Schmidt number, [-]
T	temperature, [K]
t	time, [s]
u_i	ith component of fluid velocity, [m s^{-1}]
u_i	fuel injection velocity, [m/s]
u_i', u_i''	ith component of fluctuation velocity, [m s^{-1}]
V	volume, [m^3]
v	particle volume as internal coordinate for TiO_2, [m^3]
vp_0	initial monomer volume of TiO_2, [m^3]
w	weight of quadrature approximation, [-]

X	mole fraction, [-]
Y	mass fraction, [-]
Z, Z^*	mixture fraction, [-]
Z''^2	mixture fraction variance, [-]

Greek symbols

α	Planck mean absorption coefficient, [atm^{-1} m^{-1}]
β	aggregation kernel, [m^3 s^{-1}]
Γ	diffusivity, [m^2 s^{-1}]
δ	Kronecker delta, [-]
ϵ	turbulent dissipation rate, [m^2 s^{-3}]
ε	(maximum) size of nuclei, [34 nm (soot)], [1 nm^3 (TiO_2)]
ζ	weighted abscissa, [variable]
λ, ν	eigen values and eigen vectors respectively, [-]
μ	dynamic viscosity, [kg m^{-1} s^{-1}]
μ_k	kth moment of PSD, [variable]
ν	kinematic viscosity, [m^2 s^{-1}]
ξ	internal co-ordinate, [variable]
ρ	density, [kg m^{-3}]
σ	Stefan-Boltzmann constant, [W m^{-2} K^{-4}]
τ	shear stress, [Pa]
τ_α	chemical reaction time scale, [s]
τ_ϕ	flow time scale or turbulent mixing time scale, [s]
ϕ	mean value of scalar quantity, [-]
ϕ''	fluctuation value of scalar quantity, [-]
Φ	variable matrix of size 4×1 (in DQMOM), [-]

Subscripts

0	primary particle
i, j	spatial components
n	nucleation

g	molecular growth
rad	radiation
s	soot
t	turbulence, total
α	node in DQMOM, αth species
$TTIP$	titanium-tetraisopropoxide

Superscripts

agg	aggregation
$growth$	growth
n	iterative index
nuc	nucleation

Abbreviations

BC	Black Carbon
CFD	Computational Fluid Dynamics
CFD-O	CFD-based Optimization
DQMOM	Direct Quadrature Method of Moments
DNS	Direct Numerical Simulation
EDC	Eddy Dissipation Concept
LE	Laser Extinction
LII	Laser Induced Incandescence
NDF	Number Density Function
PAH	Polycyclic Aromatic Hydrocarbons
PBE	Population Balance Equations
PDF	Probability Density Function
PM	Particulate Matter
PSD	Particle Size Distribution
QMOM	Quadrature Method of Moments
SMOM	Standard Method of Moments
TEM	Transmission Electron Microscopy

TTIP	Titanium-tetraisopropoxide
UDF	User Defined Function
UDS	User Defined Scalar

Contents

Nomenclature **viii**

1 Introduction & literature review **1**

1.1 Why this study ? 1

1.2 Soot formation and modeling in turbulent combustion systems: literature synthesis

1.3 Literature on the synthesis of TiO_2 nanoparticles in flames . . 12

1.4 Application of QMOM/DQMOM in different physical and chemical processes 18

2 Population Balance Equation and Moment based methods **23**

2.1 Introduction 23

2.2 Solution of population balance equations 25

2.3 Solution of population balance equations using QMOM 26

2.3.1 Mathematical formulation 27

2.3.2 Source term evaluation for the different processes . . . 28

2.3.2.1 Nucleation (J): 28

2.3.2.2 Molecular growth (G) and Oxidation (O): . . 29

2.3.2.3 Aggregation: 29

2.3.3 Steps involved in QMOM solution procedure 31

2.4 Solution of population balance equations using DQMOM . . . 34

2.4.1 Mathematical formulation 35

2.4.2 Source terms evaluation for the different processes . . . 38

2.4.3 Steps involved in DQMOM 38

2.5 Numerical results with QMOM/DQMOM 38

3 Employed numerical models **44**

3.1 Gas phase models 44

3.1.1 Computational Fluid Dynamics (CFD) 44
3.1.2 Non-premixed turbulent combustion 47
3.1.3 Gas phase chemistry 48
3.1.4 Equilibrium combustion model 49
3.1.5 Laminar flamelet combustion model 50
3.1.6 Eddy Dissipation Concept Model (EDC) 50
3.2 Dispersed phase chemical and physical models 52
3.2.1 Particle phase models : Soot 52
3.2.1.1 Nucleation, Growth and Oxidation rates . . . 53
3.2.2 Particle phase models : TiO_2 55
3.2.2.1 Overall rate: 55
3.2.2.2 Growth rate: 56
3.2.2.3 Nucleation rate: 56
3.2.2.4 Expressions for nucleation, growth and aggregation 56
3.2.3 Heat of reaction of TTIP decomposition 57
3.3 Radiative heat transfer 57
3.3.1 Gas-phase radiation in soot modeling 57
3.3.2 Soot radiation models 58
3.3.2.1 Radiation model I 59
3.3.2.2 Radiation model II 59
3.3.2.3 Radiation model III 59
3.3.3 Gas-phase radiation in TiO_2 production 60

4 CFD-based Optimization (CFD-O) 61
4.1 Objective functions 61
4.1.1 Objective function-1 ($OF1$): 62
4.1.2 Objective function-2 ($OF2$): 62
4.2 Experimental uncertainties 64
4.3 Numerical optimization strategy 65
4.3.1 Computational procedure: 66

5 Improved soot prediction models for turbulent non-premixed ethylene/air flam
5.1 Configuration 68
5.2 Results with original soot models 69

5.2.1 Effect of fractal dimension 70
5.3 Optimization-Case I 74
5.3.1 Optimization parameters 75
5.3.2 Results & Discussion on generality 76
5.4 Optimization-Case II 84
5.5 Parameters and objective functions 84
5.5.1 Results & discussion 84
5.5.1.1 Optimal soot models for optimization Case II-1 87
5.5.1.2 Optimal soot models for optimization Case II-2 90
5.6 Optimization-Case III 95
5.6.1 Models for radiative heat transfer 95
5.6.2 Results & Discussion 96
5.6.2.1 Radiation model I (Eq. 3.29) 97
5.6.2.2 Radiation model II (Eq. 3.30) 98
5.6.2.3 Radiation model III (Eq. 3.31) 98
5.6.2.4 Optimal model combination 99
5.7 Summary 100

6 Modeling TiO_2 nanoparticle formation in CH_4-O_2 diffusion flames 104
6.1 Introduction 104
6.2 Configuration 104
6.3 Computational details 105
6.4 Employed models 107
6.5 Results & Discussion 108
6.5.1 Effect of reaction mechanism 109
6.5.2 Effect of EDC model parameter (C_τ) 110
6.5.3 Results with TiO_2 nanoparticles 110
6.6 Parametric study 112
6.6.1 Exchanging injections for a fixed geometry 112
6.6.2 Effect of change in burner diameter 113

7 Conclusions 121

Bibliography 124

Chapter 1

Introduction & literature review

1.1 Why this study ?

The present research work is centered around modeling of nanoparticles in turbulent diffusion flames. The first and major part of this work is devoted to soot particle modeling in ethylene/air diffusion flames. The second part is devoted to modeling of TiO_2 nanoparticles synthesis in methane/oxygen diffusion flames with titanium tetraisopropoxide as precursor.

Ever since environmental regulations became more and more stringent, the limit on particulate matter (PM) emissions from engines have been dramatically reduced due to their adverse effects on human health and environment. Table 1.1 depicts the European emission limits (g/km) for PM of passenger cars. The equivalent norms in India for light duty vehicles are shown in Table 1.2 (source: Wikipedia). Among these emitted particulate matters from engines, the "soot" particles contribute the major part [2]. Soot is also known as Black Carbon (BC). Soot particles are fractal-like aggregated products of small spherical particles constituted with elementary and organic carbon. They are important and inevitable products of combustion processes (fuel-rich, incomplete combustion).

The main sources of soot or Black Carbon are depicted in the pie chart (Fig. 1.1). Most of the soot is produced through open biomass burning followed by automobiles engines, residential uses (e.g., cooking stoves) and from industries [3].

Although soot has several adverse effects, in some practical combustion

Tier:	Euro 1	Euro 2	Euro 3	Euro 4	Euro 5	Euro 6
Year:	1992	1996	2000	2005	2009	2014
PM (g/km):	0.14	0.08	0.05	0.025	0.005	0.0025

Table 1.1: PM emission standards for passenger cars in Europe

Tier:	Euro 1	Euro 2	Euro 3	Euro 4
Year:	2000	2005	2010	2010*
PM (g/km):	0.14 - 0.25	0.08 - 0.17	0.05 - 0.10	0.025 - 0.06

Table 1.2: PM emission standards for light duty vehicles in India (* indicates only selected cities)

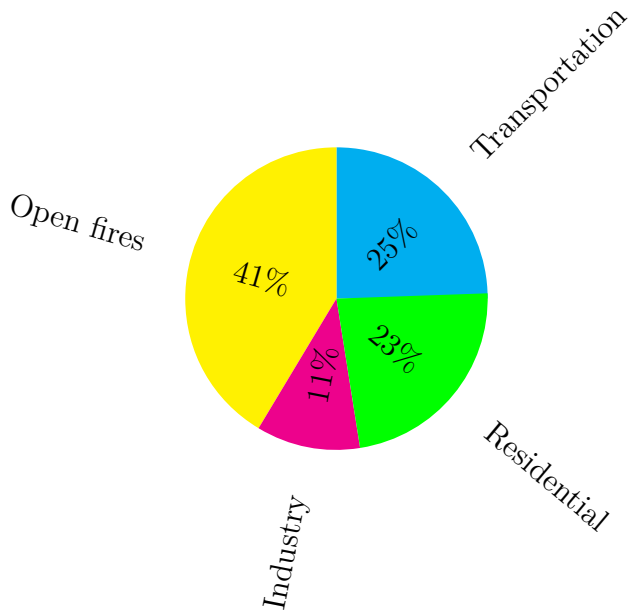

Figure 1.1: Share of global black carbon in 2000 by various sources [3]

systems such as in glass furnaces soot formation is useful and important since it enhances the heating through radiation. The distinction between soot or black carbon and carbon black is vague in literature. Most types of commercially produced carbon black contain more than 97% elemental carbon, whereas soot/black carbon usually contains a lesser percentage of elemental carbon. Carbon black is currently one most commercially significant product with an annual production of 8.1 million tons. It finds its applications in automobile tires, rubber, plastic products and in printing inks. More recent applications include the use of carbon nanoparticles as a catalyst or catalyst support [4].

On the negative side, the recent research findings blame BC (soot) as one of the significant contributors to global warming immediately after CO_2, and any measure to control the emission of soot will have an immediate effect on the global warming since the life time of soot is shorter (a few days) than that of CO_2 [5] (several years). In Fig. 1.2 the percentage of global warming ascribed to different green house gases and BC is shown [6, 7]. The Intergovernmental Panel on Climate Change (IPCC) estimates rank both BC and methane on same level in their contribution to global warming (BC$\approx$0.448; methane$\approx$0.498 W/m^2). In recent years scientists increasingly believe that BC contribution may be very high (0.913 W/m^2) and that the exact quantitative measure of BC content in the atmosphere is difficult (values shown in Fig. 1.2 are for 2005).

There have been numerous studies during the last decades to understand soot formation and its evolution. Nevertheless, many questions remain unsolved due to the tremendous complexity of this process, involving gas-phase and surface kinetics, coupled with turbulence, large heat transfer by radiation and intricate interactions between the particles. There has been significant improvement in isolated modeling aspects of soot formation. Several studies aiming at quantitative prediction of soot particles were successful, at least for simple fuels. Prediction of soot from complex fuels and in complex process conditions such as in automobile engines is still extremely difficult, demanding tremendous amount of modeling and computational efforts.

The existing phenomenological descriptions still do not explain completely the sooting phenomena. For e.g., models for soot nucleation, evolution of the

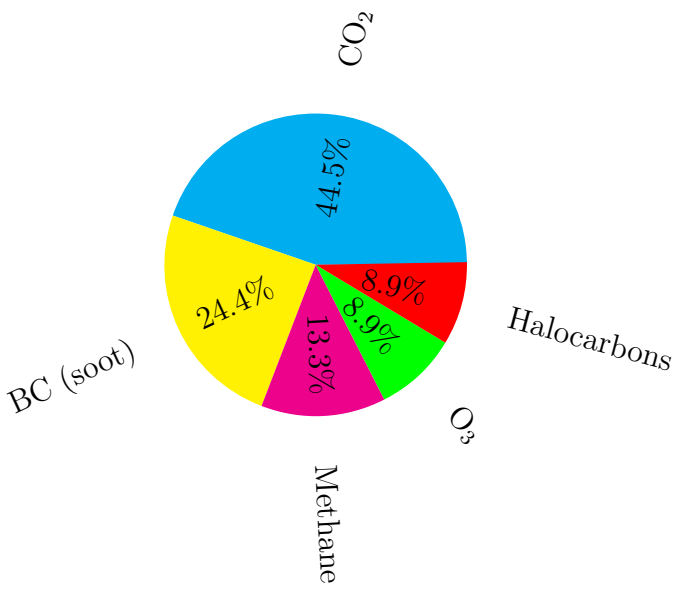

Figure 1.2: Global warming contribution of green house gases and the BC (soot)

chemical structure of soot and gas-surface reactions are still at an elementary level [8]. Wang goes on to claim that the much celebrated HACA mechanism may be incomplete to describe the soot formation process, because the mass growth of soot may proceed without the presence of H atoms [8]. Recent studies points out that the structure of nascent soot could be drastically different from that of mature soot particle. Cain et al. show evidence for the presence of aliphatic HC in nascent soot investigated in premixed ethylene flames [9]. The authors claim that mature soot typically contains C/H atomic ratio ranging from 8:1 to 12:1, whereas in nascent soot the ratio could be as small as unity. The nascent soot particles (< 10 nm) appear to be in a liquid-like structure, therefore the mass density is approximately 1.5 g/cm^3, which is notably smaller than that of mature soot, 1.8-2.0 g/cm^3 [9].

Detailed precursor kinetics are also highly difficult. On the other hand, the modeling approach with semi-empirical correlations is simple, computationally affordable and hence it is an attractive choice. Therefore, semi-empirical correlations are widely used in soot modeling. There is a growing demand for more accurate models that can be applicable to a variety of cases. Considering the complexity of soot production, if the developed models are applicable

for well-defined flow conditions and for a given, simple fuel then this is already a valuable contribution. Therefore, the first and the prime objective of the present research work is to develop such semi-empirical soot models for turbulent ethylene/air flames by using Computational Fluid Dynamics (CFD) and optimization (CFD-O).

The second objective of this work is to predict the formation and evolution of TiO_2 nanoparticles. For this purpose turbulent methane/oxygen/Ar diffusion flames are considered with titanium-tetraisopropoxide (TTIP) as precursor. TiO_2 nanoparticles have a wide range of applications such as in pigments (white), photo-catalysis, sunscreens and solar cells. The flame synthesis of nanoparticles such as TiO_2 involves introduction (injection) of a precursor dopant, in a gaseous or liquid state to the combustion system (flame) with the help of a carrier gas. The precursor decomposes at given flame conditions and forms nuclei (a few nanometers in size). Depending on process conditions the further evolution of nanoparticles occurs due to molecular growth, oxidation and aggregation.

The question may arise how these two processes (soot and TiO_2) are related? The mechanisms controlling formation and evolution of both soot and the commercial nanoparticles share common similarities. Both involve the formation of a condensed phase material, nucleation, surface growth of the particles and the subsequent aggregation into fractal structures. As a consequence the employed modeling approach is also similar. In fact, the considerable experience gained in soot modeling helped many researchers to advance in the modeling of commercial nanoparticles. Experimentally, both processes have been investigated with the same diagnostic techniques such as laser induced incandescence (LII) and transmission electron microscopy (TEM) [8]. Therefore, it is appropriate to study them together.

The present numerical study employs systematically the CFD solver *Ansys-Fluent* for solving the gas-phase governing equations. The particle-phase Population Balance Equations (PBE) are transformed to moment transport equations and solved through moment-based methods. These methods are implemented in our group into the CFD solver by using in-house user-defined functions (UDF). The detailed description of the gas-phase and the particle

phase models employed in the present work are presented in Chapter 3.

The evolution of the particle phase (soot or TiO_2) PBE is handled by Quadrature Method of Moments (QMOM) and Direct Quadrature Method of Moments (DQMOM). Moment-based methods have been proven to be accurate for predicting the first moments of a variety of particle size distributions (PSD). Additionally, they require much less computational time compared with a direct solution of the PBE or with sectional methods. QMOM/DQMOM appear very attractive since optimization can only be carried out when each individual simulation is relatively fast (at most a few hours of computing time). A complete description of the moment-based methods employed in the present work is given in Chapter 2.

Initial studies involved the use of semi-empirical soot models from literature. These models, which are called "original soot models" throughout this study are tested on 4 different turbulent ethylene/air flames. Comparisons are presented with published experimental data. It is shown later that these original models were not capable of predicting accurately the soot volume fraction (f_v). These models are improved in this work through CFD-based optimization (see Chapter 5). This numerical optimization relies on Computational Fluid Dynamics to find the best possible model parameters. CFD-based optimization (CFD-O [10]) has been successfully applied to different configurations involving heat transfer and flames within our research group in the past [11, 12]. Based on this experience, a Genetic Algorithm (GA) coded in the in-house optimization library OPAL (OPtimization ALgorithms) has been combined with the industrial CFD solver *Ansys-Fluent* for the present study. All details about CFD-O can be found in Chapter 4.

CFD-O has been performed in several cases starting with the simplest gas-phase chemistry i.e., with equilibrium approximation. The predictions could be improved in this case when compared to the original models, but were still not satisfactory. Hence, in subsequent steps optimizations are performed by considering more refined turbulent combustion models and considering soot radiation. The finally obtained, optimized set of models leads to a significant improvement of the predictions. The detailed analysis of the results is presented in Chapter 5.

The numerical results concerning TiO_2 nanoparticle formation in turbulent CH_4-O_2 flames are presented in Chapter 6, before concluding. In the following sections a brief literature review is proposed concerning the formation of soot and TiO_2 nanoparticles in flames.

1.2 Soot formation and modeling in turbulent combustion systems: literature synthesis

Due to the adverse effects of soot on human health as a carcinogenic [13, 14] and on the environment as one major global warming component [15, 16] with a high impact on cloud cover and visibility [17], there have been numerous studies during the last decades to understand soot formation and its evolution.

In spite of this the chemical mechanism of soot formation is still not very clearly understood. The overview of the literature shows that the most ambiguous process in soot modeling is nucleation on which much focus needs to be made. Different soot inception routes can be found. Among them HACA mechanism (H-abstraction/C2H2-addition: PAH[1] route) is the most widely accepted assumption in the literature. Some PAH molecules decompose and form small aliphatic HCs which in turn form acetylene molecules. These PAH molecules further grow in their size in 3-dimensional structure due to the sequential chain reaction with the acetylene molecules and form nascent soot particles. These acetylene molecules also provide major contribution for further growth of the soot particles. Shock tube experiments are typically used to analyse the chemical mechanisms of soot formation.

Frenklach and co-workers discussed the chemical mechanism of soot formation in several articles. Accordingly, the formation of first aromatic ring in the non-aromatic fuels (e.g., ethylene as in the present study) begins usually with vinyl addition to acetylene [18]. Once the first aromatic ring is formed, they grow in their size by a sequential two-step: H-abstraction which activates the aromatic molecules, and acetylene addition which propagates molecular growth and cyclization of PAHs as depicted in Fig. 1.3. Now these

[1] polycyclic aromatic hydrocarbons

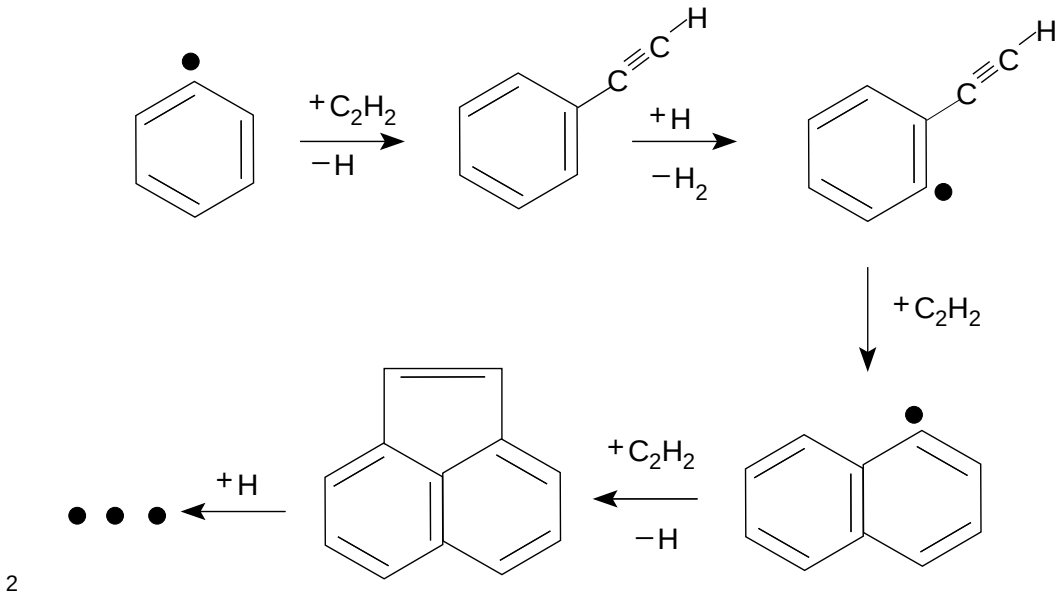

Figure 1.3: H-abstraction-C2H2-addition reaction pathway of PAH growth taken from [18]

formed macro molecules (PAH) in turn coagulate and form dimers, trimers and tetramers and so on in three dimensional structures. Beginning with the dimers the forming clusters were assumed to be in solid phase (nuclei) and allowed to add and lose mass by surface reaction (growth and oxidation) [18, 19].

The widely accepted soot formation and evolution model as depicted in [20] is shown in Fig. 1.4. This mechanism builds on top of that described by Frenklach and co-workers [18].

Soot models are often classified into 3 different groups [21]: i) empirical ii) semi-empirical and iii) kinetic soot models. While empirical models do not allow detailed predictions, kinetic soot models are obviously best suited to describe all the complex pathways leading from the fuel to the final particles. A detailed modeling of soot formation based on polycyclic aromatic hydrocarbon (PAH) concentration is given for instance in [22]. Nevertheless, such models are difficult to be employed in real, three-dimensional flames of practical interest, due to the considerable computational time required by the simulations [23]. As a consequence, semi-empirical models are mostly used at present and are therefore the target of this work. They involve less computational effort by simplifying all kinetic aspects. Usually, one single chemical species is deemed

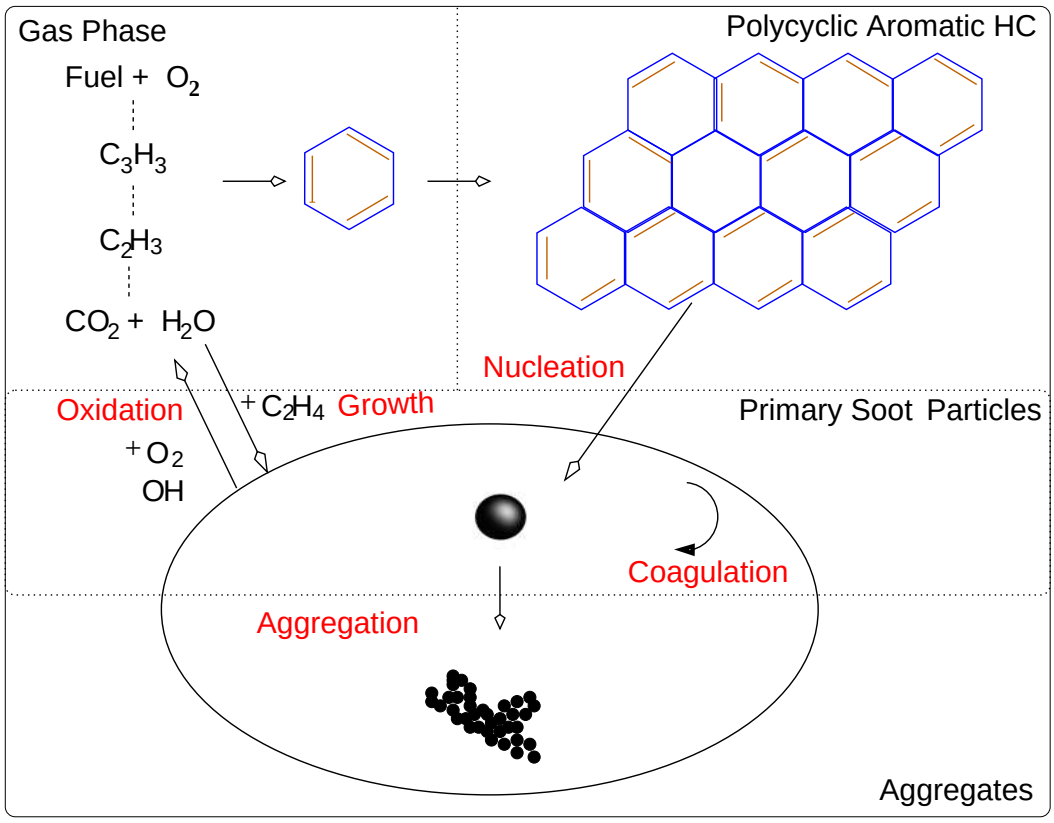

Figure 1.4: The four most important physico/chemical processes responsible for soot formation [20]

responsible for soot nucleation and rate equations are developed based only on this species. For example, acetylene [24, 25], benzene, naphthalene or PAH [26] are considered to be responsible for soot inception in ethylene/air flames. In some instances more than one species is ascribed responsible for nucleation, e.g., diacetylene and naphthalene in [27]. In this manner, the key processes controlling soot formation and evolution of the solid phase are then nucleation, surface growth, aggregation and oxidation [28, 29]. They must be described by suitable physical models, together with radiative heat transfer. As in the present work, molecular growth of the soot particles is mostly associated with acetylene in ethylene/air flames, while oxidation rates are usually computed from local oxygen concentration.

In the past, several authors tried to propose suitable combinations of particle phase models in order to predict soot production. For instance, Ma *et al.* tried different combinations of inception, growth, oxidation and aggre-

gation models in order to determine the best parameters for a non-premixed ethylene/air flame [26]. Three different kinds of inception models (acetylene inception route, the PAH inception route, and the naphthalene inception route), three types of surface area functions for growth, three different coagulation constants and finally three expressions of soot oxidation were investigated. Zucca *et al.* proposed another model combination for the same type of flames, again validated against experimental results [30]. Being more recent, the model formulation presented in [30] has been retained as initial solution for the optimization process described in what follows. Even if such studies have led to a significant improvement in understanding and predicting soot formation, available models have yet to yield satisfactory comparisons against all available experimental data [31, 32]. There is thus a clear need for more accurate prediction models, applicable to a wide range of flow and operating conditions. First computational studies in our group concerning predictions of soot volume fraction [33] have demonstrated that the nucleation and oxidation models play a first-order role for typical flame configurations, followed by molecular growth and finally aggregation processes. Therefore, nucleation and oxidation parameters are first retained in the following optimization.

Radiative heat transfer is significant in most combustion processes. Due to the diversity of involved combustion products, to the complexity of obtaining their radiative properties and to the coupling with turbulent flows, the development of suitable radiation models is a challenge [34]. Selected gaseous species (notably H_2O and CO_2) and particles (here soot) are the major contributors to radiation. Among those, soot particles are by far the most important radiating product in sooting flames, emitting in a continuous spectrum in the visible and infrared regions [35].

As explained earlier, when modeling soot formation in practical systems, semi-empirical approaches are mostly used. Involved particulate models (nucleation, growth...) are all non-linear functions of temperature. Due to this strong two-way coupling between soot and temperature, it is important to model radiative heat transfer with a sufficient accuracy, while keeping acceptable computational times. However, this is a real challenge since accurate radiation models require a large amount of computing times, while simple models,

as considered in the present study, do not always lead to correct predictions.

An accurate evaluation of radiative heat transfer in turbulent flames is extremely difficult due to three main challenges. First, it is difficult to obtain numerically a correct solution of the radiative transfer equation (RTE), a five-dimensional integro-differential equation. Secondly, the spectral behavior of the radiating species and the spectral integration of the equations lead to many problems. Finally, the evaluation of turbulence/radiation interactions is unsolved, in particular for steady RANS simulations [36]. Additionally, the soot particle size distribution (PSD) impacts radiation in sooting flames, but this PSD is mostly not known with a good accuracy. The shape of the soot particles also influences radiation [37], even if they are usually assumed spherical. All these open issues lead to implementation difficulties in existing CFD codes. Even with a successful implementation, the resulting computational times prevent using truly accurate models for most practical configurations of interest. As a consequence, it has been a common practice in the past to invoke the optically thin approximation and to assume the medium to be grey [19, 25, 38] when simulating turbulent burners, and we will keep the same hypothesis.

An analysis of existing soot radiation models (e.g., [39, 40]) shows that there is still a high level of uncertainty concerning the most appropriate model description. As a consequence, this aspect is taken as well into account in the optimization process. The detailed description about the various soot radiation models considered in the present study can be found in Chapter 3

For the later optimization three different but simple soot radiation models found in the literature and based on a grey medium and optically thin approximation have been considered and compared. All three are implemented for the simulation of nonpremixed turbulent ethylene/air flames. Four different published experimental works (see Table 5.1, on page 69) are used to compare the quality of the numerical predictions.

The particulate phase must always be solved in a coupled manner together with the reactive Navier-Stokes equations. For this purpose, Netzell *et al.* used sectional method for calculating PSD of soot in turbulent diffusion flames [41]. The authors considered in total 100 sections and emphasized the advantage

of this method as it delivers a PSD. Monte Carlo based methods have been employed in many publications (see [42–45]) for modeling soot formation in different flame configurations. Certainly, Monte Carlo methods also demand high computational times. As an alternative, Method of moments (MOM) can be used with interpolative closure for modeling soot formation in laminar and turbulent flames [19, 20, 46, 47]. In order to obtain a computationally efficient solution, QMOM/DQMOM have been coded for the present study into *Ansys-Fluent* using User-Defined Functions. The quadrature approximation [48] used in QMOM/DQMOM solves the closure problem associated with nonlinearities in source terms such as growth and aggregation. With DQMOM, the PBE simplifies into a set of algebraic equations with few additional transport equations [49]. For example, if we consider 2 nodes for the quadrature approximation as in the present project, only 4 transport equations must be solved in both QMOM/DQMOM thus speeding up the computations compared to a direct solution of the PBE.

Four different turbulent non-premixed ethylene/air flames [50–53] have been considered for validation purposes in this work. The first flame [50] is employed to determine the optimal set of model parameters by comparing the obtained fields of temperature and soot volume fraction. The generality of optimal model is then checked by comparison with three other flames [51–53]. All results concerning optimization and validation for soot predictions are discussed in Chapter 5

1.3 Literature on the synthesis of TiO_2 nanoparticles in flames

The scientific and commercial interest in the manufacture of nanoparticles has increased many folds since the importance of nanoparticles is now well documented for numerous applications. The special properties of nanoparticles make their use attractive in several regards. These special properties are mainly due to the large surface to volume ratio of nanoparticles. For a particle of about 4 nm, half of the molecules forming the nanostructure are actually at

the surface with consequences for the lattice structure. This causes dramatic changes in the physical and chemical properties (like melting point, magnetic and optical properties) of nanomaterial compared to the same bulk material [54].

Extensive research is going on in varied fields of science to analyse the applicability of nanoparticles. Nanoparticles are excellent catalysts and have been used in synthesis of several components. Major applications of nanoparticles are summarized as follows:

- Ceramics - TiO_2, Al_2O_3, Fe_2O_3
- Catalysis - VaO_2-TiO_2, $Pt/Ba/Al_2O_3$, $DeNO_x$, TiO_2-SiO_2 epoxide catalysts, Pd/Al_2O_3, KF/CaO (in bio-diesel production), TiO_2
- Fiber optics - SiO_2
- Nano-magnetic material, data storage - Fe_2O_3
- Super conducting materials - Sn, Al, $CeCo_2$,
- Fuel cells - with nano-catalysts, electrolyte (gadolinia for solid oxide fuel cell), nano-composites for gas barriers, Carbon nano tubes (CNT)
- Electronics - sensors SnO_2, titania based
- Chemical - mechanical polish and in coatings
- Medical applications - drug delivery and diagnostics - polymer nanoparticles for oral anticancer drug delivery, pulmonary vaccines, diabetic, orthopaedic, dental and nutritional products
- Pigments - TiO_2, carbon black
- Flowing aids - SiO_2 for pharmaceuticals and cosmetics
- Inorganic membranes and sunscreens - ZnO, TiO_2
- Solid rocket propellants - Al particles

Despite the wide spread applications of nanoparticles, adverse effects of fine particles on health and environment are also worthy of special research. A clear knowledge on health/environment effects of nanoparticles is still limited. Several studies document the adverse effects of different nanoparticles [55–57].

Gas-phase flame synthesis processes are often chosen to produce nanoparticles, in large quantities as it is in general cleaner, more energy-efficient, environmentally cleaner and easier [58, 59]. This process also does not involve expensive steps of solid-liquid separation, washing and drying as in wet chemistry processes. As a consequence flame reactors are one of the most common methods used for the production of high-purity nanoscale powders in large quantities, especially for silica, titania, and alumina. There are several industrial-scale plants operated world wide that already produce several million tons of nanoparticles per year. For instance, Degussa (now Evonik) has developed to maturity the large-scale production of nanostructured zinc oxide, based on gas-phase synthesis for use as a UV filter in sunscreens.

The flame synthesis of nanoparticles involves introduction (injection) of a precursor dopant in a gaseous or liquid state in to the combustion system (flame) with the help of a carrier gas. This precursor decomposes (mostly due to oxidation) at given flame conditions and forms nuclei (a few nanometers in size). Depending on process conditions further evolution of nanoparticles occurs due to molecular growth, oxidation and aggregation. When formation process of commercial nanoparticles is compared with soot formation, the oxidation is found to be rarely significant in the former case. The basic steps of particle formation and growth from gas to particle conversion in a flame are shown in Fig. 1.5.

Flame synthesis of various nanoparticles, like SiO_2, TiO_2, and SnO_2, mixed oxides or nanocomposites such as V_2O_5/Al_2O_3, Fe_2O_3/SiO_2 have been discussed by several authors in recent years, for instance in [54, 58, 60]. Process chemistry, transport phenomena, particle dynamics and nanoparticle applications have been discussed in detail in these works. Accordingly, process variables such as material properties, flame configuration, precursor type, temperature, oxidant composition, mixing, are known to play an essential role for final product characteristics. According to the literature, process temperature

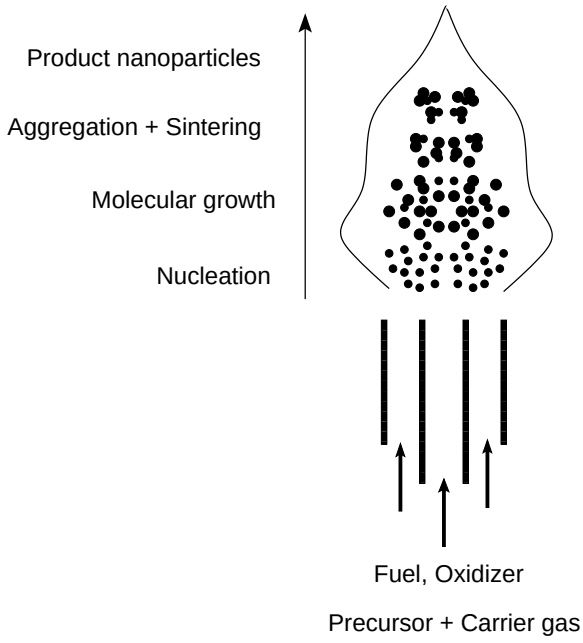

Figure 1.5: Important physico/chemical processes for flame synthesis of nanoparticle

is most significant.

An extensive literature analysis shows that significant progress has been made concerning experimental synthesis of nanoparticles [54, 61–67]. Concerning more specifically the process considered in the present project, synthesis of non-aggregated titania nanoparticles from oxidation of TTIP ($Ti(C_3H_7O)_4$) in atmospheric pressure diffusion flames has been studied by [68]. Two different flame configurations were investigated in a diffusion burner with various flow rates of O_2. The influence of process parameters on primary particle size, specific surface area and morphology was discussed. The authors showed that an increase in O_2 flow rate increases the BET (Brunauer-Emmett-Teller) equivalent diameter and the degree of aggregation due to changes in residence time and temperature. Ma and Yang also studied experimentally the production of TiO_2 nanoparticles from TTIP [69]. The authors investigated the effect of various combinations of feed flow rates on the final particle characteristics and its morphology (anatase and rutile fractions). The characteristics of TiO_2 nanoparticle produced from premixed and a diffusion flames (from modified Hencken burner) were compared, showing the advantage of the newly developed Hencken burner [70].

Pratsinis and co-workers discussed in many publications the experimental synthesis and modeling of various nanoparticles. TiO_2 production has been documented more particularly in [1, 62, 71]. Coflow burners of 3 different dimensions have been used for various precursors, fuel and oxidizer flow rates. Synthesis of TiO_2 nanoparticles using TTIP as precursor was investigated experimentally and numerically by [72]. Using a sectional method, particle size distribution (PSD), average primary particle size and geometric standard deviation were analyzed for a wide range of process parameters and validated by experiments. Sunsap *et al.* studied experimentally in a diffusion flame reactor the effect of oxidizer, fuel flow rates and filter position on specific surface area, primary and secondary particle sizes, morphology, phase composition and crystallite size of TiO_2 nanoparticles [73]. The same authors have studied computationally the influence of process parameters (various flow rates of O_2 and CH_4) on production (deposition rate) of TiO_2 nanoparticles in the diffusion flame reactor during CH_4 combustion.

The focus of many experimental investigations found in the literature is mainly set on studying the influence of selected process parameters such as flow rates of fuel/precursor/oxidizer and flow configuration on final particle characteristics for a fixed burner. This experimental process optimization is quite costly and time-consuming. A similar optimization based on simulations would be more cost effective and faster, if efficient and accurate physicochemical and numerical models and available to describe the target properties of TiO_2 particles.

In [74], the production of TiO_2 nanoparticles in CH_4-air diffusion flames using $TiCl_4$ as precursor is considered, while [75] investigates a premixed flame with TTIP as precursor. The numerical results are found in fair agreement with experimental data in both studies. In both studies the authors employed the CFD solver *Ansys-Fluent*, as done here. Synthesis of TiO_2 nanoparticles by TTIP oxidation in a premixed methane-oxygen flame has been studied in [76]. A moving sectional method is employed accounting for gas phase chemical reactions, coagulation, surface growth and sintering. Influence of surface shielding and surface energy on growth mechanisms during titania generation has been modeled in the oxidation of $TiCl_4$ by [77].

Yu *et al.* combined Computational Fluid Dynamics with particle kinetics to study the effect of precursor loading on non-spherical TiO_2 nanoparticle synthesis from TTIP in a diffusion flame reactor [59]. Same authors described numerical evaluation of TiO_2 nanoparticle synthesis from $TiCl_4$ in diffusion flame under similar lines to the earlier work [78]. Sung et al. studied the TiO_2 nanoparticle production from a non-premixed flame configuration with $TiCl_4$ as precursor [79] by taking into account the nucleation and aggregation. In the present study, the molecular growth effect is additionally taken into account.

TiO_2 formation by oxidation of TTIP and $TiCl_4$ has been studied numerically for producing narrower PSD of aerosols by controlling the reactions on the particle surface in [80]. The authors explored the effect of various process parameters such as pressure, temperature and initial precursor molar fraction on surface growth reaction of titania particles. Volume-based size and standard deviations (σ_g) were compared for all the cases. It is shown that increasing either process temperature, pressure or initial precursor molar fraction enhanced surface growth, which resulted in a narrower PSD. According to these authors further improvements are possible until obtaining nearly monodisperse PSD ($\sigma_g < 1.3$).

Although there is good progress in developing and commercially producing different nanoparticles for various applications through experimental analysis, the modeling approach is still poorly developed. Much kinetic and thermochemical data is still missing. While modeling nanoparticle formation in flames, one usual but important assumption is the decoupling of the gas-phase chemistry from the particle-phase chemistry, thus avoiding the complications associated with heterogeneous kinetic data between the phases [58]. Including detailed particle phase kinetics in the modeling is of course desirable and should give more accurate predictions. But, at the same time it involves huge computational efforts. In most cases, authors assume a single-step, global reaction to describe nuclei formation from the precursor solution. This is also the approach retained here.

All these studies rely on a manual, trial-and-error strategy in order to improve the process. Moreover, they always consider a fixed burner geometry. Optimizing particle properties on a short time scale, with a higher efficiency

and taking all relevant parameters into account (including burner and flame configuration) is still very challenging. For this, coupling simulations with optimization techniques would be far more efficient [10, 12]. Applying this optimization technique for producing nanoparticles from flame reactors is the ultimate purpose of this project. As a first step, in the present work, a manual optimization of process conditions and geometries is attempted, with the objective of obtaining a lower mean diameter (d_{mean}), a higher volume fraction (f_v) and a narrower PSD (minimizing σ_g, tending towards a monodisperse case).

In the following section, a review of literature on application of moment-based methods (specifically QMOM and DQMOM) in various fields of science is given.

1.4 Application of QMOM/DQMOM in different physical and chemical processes

The complete description of these moment-based methods (QMOM and DQMOM) is given later in Chapter 2. In this section only the application of these methods to different fields from literature is discussed. As stated earlier the evolution of the solid phase is handled by PBE and needs to be solved along with Navier-Stokes equations in a variety of chemical engineering problems. QMOM and DQMOM have been applied and validated in a wide range of applications such as fluidization, crystallization, precipitation, combustion, etc.

For instance, QMOM/DQMOM has been implemented to study polydispersed gas-solid fluidized beds. DQMOM was used by Fan et al. to model the aggregation and breakage process in fluidized bed and has been coupled to a CFD code for this purpose [81]. In this case each quadrature node represents a distinct solid phase and thus is convected with its own velocity, as a multi-fluid CFD code is employed. Therefore, it is an important improvement when compared with QMOM. The authors have studied the effect of the number of nodes N (2, 3 and 4) and compared the results. From the results the authors

recommend the kinetic theory kernel and 3 quadrature nodes ($N = 3$) for fluidized bed reactors.

The importance of particle mixing and segregation were studied for a binary system with a continuous PSD by Fan and Fox [82]. In this work, the authors used a multi-fluid model based on the Euler-Euler approach and DQMOM to describe particle segregation in polydispersed fluidized beds. Model predictions are validated with available experimental and simulation data. The results showed that, when the PSD is narrow or the superficial gas velocity is high, less nodes are needed. For a wide PSD with significant segregation, at least 3 quadrature nodes are needed for accurate results. One important limitation of QMOM/DQMOM was recently highlighted by Mazzei [83]. The author studied the dynamics of two inert polydisperse fluidized suspensions which are initially segregated (dense system). The author reveals an important limitation, that QMOM/DQMOM fails to properly model the diffusion in real space. This is because diffusion is caused by the particle population being continuously distributed over the internal coordinates; this continuity no longer exists when the NDF is approximated with a quadrature formula, since doing so seperates the distribution into a finite number of classes (in the extreme case of one class, all the particles would have the same internal coordinates, which clearly kills diffusive fluxes) [83].

Zucca et al. validated DQMOM approach in the soot formation modeling of turbulent ethylene/air diffusion flame [30]. In this case the DQMOM algorithm has been implemented in *Ansys-Fluent*. Nucleation, growth, aggregation and oxidation were considered as the particle phase source terms. With a monovariative PBE and 2 nodes of the distribution, just 4 additional scalar transport equations need to be solved. Recently the same authors applied DQMOM to bi-variative PBE with particle volume and area as the internal co-ordinates [84] and demonstrated its simplicity in extending it to multi-variate PBEs. Results are shown considering 2 and 3 quadrature nodes ($N = 2, 3$). Comparisons were also made with Monte-Carlo Method (MCM). A pseudo bivariate PBE was also used to describe the soot formation modeling in turbulent flames by Marchisio under similar lines [84].

The choice of moments also plays a significant role in the accuracy of

moment methods (QMOM/DQMOM) and certain choices of moments will minimize the condition number of matrix A (see Section 2.4.1). QMOM and DQMOM approaches were validated by Upadhyay and Ezekoye [85] using an analytical solution by considering a simplified problem of aerosol settling and diffusion between infinite parallel plates. The authors investigated the accuracy of the solutions by considering different sets of moments of the initial NDF and concluded that the solution to the moment equations depends on the initial choice of moments. Therefore, it is possible to improve the accuracy of the solution by an optimal choice of moments. According to Fox, poor choices for the moment set can lead to non-unique abscissas and even negative weights [86]. According to Zucca et al., proper selection of the moments is necessary for the stability and the lower order moments benefit most from a better condition of the matrix [84].

McGraw and co-workers extended the application of QMOM to bivariate PBE (representing particle volume and area) for modeling particle coagulation and sintering processes [87]. The calculations were performed with $N = 3$ and $N = 12$ nodes. Please note that in the later case one needs to consider 36 moments. Therefore the selection of moments and the calculations become quite challenging. Fox [88] applied DQMOM to the same problem and the published QMOM results were reproduced demonstrating the simplicity of DQMOM over the previously published work on QMOM. It is found that the coagulation and sintering kernels used in this test case are easily handled by lower-order moment methods, and are relatively insensitive to the choice of bivariate moments used for DQMOM.

Moment methods are also increasingly gaining importance in the modeling of commercial nanoparticle products from flame synthesis route. Due to the complex nature of the physico-chemical models involved in the flame synthesis of nanoparticles, moment methods appear attractive as they are simple and less expensive. TiO_2 nanoparticle synthesis has been studied by Yu et al. in CH_4/O_2 diffusion flames with TTIP as the precursor and Ar as the carrier gas. The authors employed QMOM and obtained the first few moments of the NDF, area concentration and the primary particle diameter [59]. The authors also used QMOM in similar lines for the production of TiO_2 particles from CH_4/O_2

diffusion flames with $TiCl_4$ as the precursor and Ar as the carrier gas. They studied the effect of inlet precursor loading on the particle phase properties such as particle number, size, specific surface area (SSA) and shape [78]. Sung et al. studied the TiO_2 nanoparticle production from a non-premixed flame configuration with $TiCl_4$ as precursor [79]. The NDF is tracked by QMOM involving only nucleation and aggregation and ignored the sintering and growth effects. Only monovariate PBE is considered in all these applications.

Sprays are common in many industrial combustion applications such as diesel engines. Fox et al. applied DQMOM and multi-fluid method to solve Williams spray equation and compared the two approaches for various test-cases [89]. The other key point of the study is a detailed description of the limitations associated with each method, thus giving criteria for their use as well as for their respective efficiency. As far as coalescence phenomena are concerned, the efficiency of DQMOM has been shown to be better than the multi-fluid model due to its limited numerical diffusion in the size phase space. The authors have also shown that for the bimodal distribution function and as for as the evaporation process is concerned, DQMOM is comparable to the multi-fluid model. An interesting limitation of the moment methods has been pointed out by Massot et al., [90]. According to the authors, a drift velocity, i.e., the rate of change due to continuous phenomena affecting the internal coordinate, has to be taken into account. It is particularly important when there exists a negative drift velocity, such as evaporation of droplets or oxidation of soot particles. The authors proposed a modified formulation for DQMOM to model such instances. Very recently QMOM was applied to solve bivariate PBE in ethanol-fueled spray combustors [91].

Crystallization is an other application where the particle phase (crystals) co-exists with the mother liquor. Barium sulphate crystallization has been studied in turbulent flows by using SMOM in [92]. In this case the authors assumed a priori a crystal size distribution (CSD) with a Gaussian shape and reconstructed the distribution. PBM has been applied to batch crystallization reactor in CFD codes by Wan and Ring [93]. A simple homogeneous system with temporal variations, only one process at a time (nucleation only, growth only etc.) has been considered. SMOM and QMOM were used to obtain the

first 6 moments and the predictions were compared with an analytical solution. In contrast to this earlier study, several combinations of particulate processes (nucleation, growth and dissolution; aggregation and breakage etc.) have been studied in an ideally mixed batch crystallization reactor by Qamar et al. using QMOM [94].

There are several other moment based methods, for instance the method of moments with interpolative closure (MOMIC) and the Finite size domain Complete set of trial functions Method Of Moments (FCMOM). MOMIC was widely used by Frenklach for soot particle formation in hydrocarbon combustion flames [47, 95–97]. In MOMIC the fractional order moments are obtained through interpolation among known whole-order moments. MOMIC was also successfully implemented recently in a CFD code for the modeling of TiO_2 nanoparticles evolution from $TiCl_4$ oxidation [98]. FCMOM was applied and validated for monovariate PBE [99, 100] and for bivariate PBE [101]. In FCMOM, the method of moments is formulated in a finite domain of the internal coordinates and the particle size distribution function is represented as a truncated series expansion by a complete system of ortho-normal functions. The authors claim that FCMOM has several advantages. The solution of the PBE obtained through the FCMOM provides both the moments and also the reconstructed particle size distribution through a simple relation. The later can be particularly important as the reconstruction of the PSD is a complex issue.

After having discussed the importance of soot and TiO_2 nanoparticles and existing literature on the subject, the next chapters present the computational methods and models employed in the present project.

Chapter 2

Population Balance Equation and Moment based methods

2.1 Introduction

Solution of the Population Balance Equation (PBE) is always a crucial step in multiphase systems where the dispersed phase usually consists of solid or liquid droplets. It is nearly impossible to get an analytical solution for practical problems, although there exist analytical solutions for very simple, academic processes [102]. Due to this, great amount of research is now being carried out on solution techniques for the PBE in order to accelerate computations. Several methods have been proposed by different researchers in this regard. To list some of them : Method of classes or sectional methods, Monte Carlo (MC), moment-based methods such as Quadrature Method Of Moments (QMOM) or Direct Quadrature Method of Moments (DQMOM). There exist many other methods like Finite Element Approach to PBE, that are not discussed here. Every researcher has some reason to substantiate his or her approach and some points that find loopholes in other methods. In the present chapter the mathematical formulation and the application of moment-based methods are discussed.

Population Balance Equation (PBE) is a continuity statement for the particle number density function (f). This f is a function written in terms of internal and external co-ordinates [102]. Internal co-ordinates $\boldsymbol{\xi}$ come from the property of the dispersed phase, such as particle diameter (length), area,

volume, colour etc. External co-ordinates are physical space $\mathbf{x}$ (here bold phase of 'x' signifies that $\mathbf{x}$ is a vector) and time t.

The PBE is as shown below [49]

$$\frac{\partial f\left(\boldsymbol{\xi};\mathbf{x},t\right)}{\partial t}+\frac{\partial}{\partial x_i}\left[u_i f\left(\boldsymbol{\xi};\mathbf{x},t\right)\right]-\frac{\partial}{\partial x_i}\left[\Gamma\frac{\partial f\left(\boldsymbol{\xi};\mathbf{x},t\right)}{\partial x_i}\right]=S\left(\boldsymbol{\xi};\mathbf{x},t\right) \tag{2.1}$$

Here $\boldsymbol{\xi}$ is internal coordinate vector.

- u_i is the particle phase velocity.
- $S\left(\boldsymbol{\xi};\mathbf{x},t\right)$ is the source term (contains all the transformations such as nucleation, molecular growth, aggregation and breakage etc.)
- Γ is the diffusion coefficient.

The basic idea in moment-based methods is that the PBE can be transformed into a set of moment transport equations [103] and solved afterwards. The solution of PBE by Method of Moments is the most simple, straightforward and computationally efficient because one needs to solve only a small set of transport equations. It is proved that these methods are very easy to integrate and use in CFD codes. In my research work these moment-based methods have been implemented into commercial CFD solver *Ansys-Fluent* for modeling soot particle formation in turbulent ethylene/air flames and for the synthesis of titania (TiO_2) nanoparticles from methane flame reactors. Complex User Defined Functions (UDF) have been developed for QMOM and DQMOM. The User Defined Scalar transport equations (UDS) functionality in *Ansys-Fluent* enables to represent them as moment-transport equations in QMOM or as transport equations of weights and weighted abscissas in DQMOM.

On the other hand, there are several arguments which motivate the researchers to find alternative methods to moment methods, as the only information available here is the moments of PSD. There could be in principle many particle size distributions (PSD) that satisfy the same set of moments [104, 105]. Therefore the PSD is not unique for given moments. Reconstruction

of the PSD can be cumbersome. Several studies have successfully validated the accuracy of the first few moments of the PSD [48, 93, 106, 107]. The accuracy of higher order moments is still a subject of scientific discussion. Since the objective of my research work is to successfully predict the mean properties of the particle phase, in particular such as particle size and volume fraction f_v, the first moments should be sufficient to obtain these mean particle properties with acceptable accuracy. If the internal co-ordinate is the diameter of the particle, then the mean particle diameter is obtained through $(\frac{\mu_1}{\mu_0})$ and the third moment (μ_3) directly gives the volume fraction f_v, where μ_i represents the ith moment. Hence, higher moments are not needed.

2.2 Solution of population balance equations

Among all the moment based methods, the standard method of moments (SMOM) initially developed by Hulburt and Katz [103] is very simple but it is only valid to specific cases. It is only valid when the transformed moment transport equations are in closed form, i.e., all the terms in the transport equation are described by known moments. Due to this it does not require any additional approximation on the shape of the Particle Size Distribution (PSD). For example if a "constant" growth rate or coagulation rate is assumed, the moment transformation leads to a system of equations which are closed. This means that the value of a given moment of the distribution is only related to the value of lower order moments. In reality, real processes lead to unclosed terms in most cases [48]. Due to this, the moment transformation results in unclosed system of equations for which we need additional a priory approximations on the shape of the PSD. These unclosed terms are very common in practical applications since most of the processes are non-linear in nature. Therefore, the difficulty in moment-based methods lies in representing this closure approximation in an acceptable manner. Since SMOM is not used in this work apart for initialization, it is not described in more details. A description of at least a few frequently used methods is the subject of the present chapter.

In practice, the proper choice of an initial guess is always very important for the numerical stability of the solver. It is indeed well known that the mo-

ments of the initial number density function (NDF) are a significant factor for obtaining accurate and stable solutions from QMOM and DQMOM [85]. Therefore, following our own analysis, it is highly recommended that for all complex processes where the system of equations are not closed initially, an initial solution should be obtained with SMOM assuming corresponding simplifications. Now, use this solution in the next step for initialisation of other methods like QMOM/DQMOM. In this way it is possible to obtain suitable and stable initial values. For example, when considering only nucleation and molecular growth for soot/TiO_2 particles as shown later, the moment transformation results in a closed set of equations, which can be solved easily with SMOM. Now, this initial solution makes a good guess to QMOM/DQMOM, when we include the complex aggregation phenomena even if the system is not closed now. In all the calculations of the present work this initialization method has been employed.

In the subsequent sections the mathematical description of QMOM and DQMOM are discussed. Applications of these moment-based methods for various engineering problems has been discussed by citing examples from the literature in Section 1.4.

2.3 Solution of population balance equations using QMOM

McGraw first introduced QMOM, through which the moments of the PSD are tracked in similar lines with SMOM. Initially, he used QMOM to describe the sulphuric acid-water aerosol dynamics [48]. The method was later widely applied and validated by Fox & Marchisio [106, 108–111]. QMOM was also extensively used by other researchers for various problems [93, 94, 112].

In QMOM and DQMOM the number density function (NDF) f is represented with numerical quadrature, i.e., the distribution function is regarded as the weight function [48]. This eliminates the closure problem associated with moment transformation of the PBE involving complex terms (such as Brownian aggregation kernel). Here, the unknown NDF is approximated with

Gaussian quadrature rule, which involves the approximation of a function (f) by a summation of its function values at some points. The parameters involved in the quadrature approximation are known as weights (w_i) and abscissas (ξ_i), see Eq. (2.2). The advantage of the Gaussian quadrature rule is its freedom to choose not only the weights but also the abscissas at which the function is evaluated (i.e., abscissas are not necessarily equally spaced) [94].

2.3.1 Mathematical formulation

The quadrature approximation reads:

$$f\left(\boldsymbol{\xi};\mathbf{x},t\right)=\sum_{\alpha=1}^{N}w_{\alpha}\left(\mathbf{x},t\right)\bar{\delta}\left[\boldsymbol{\xi}-\boldsymbol{\xi}_{\alpha}\left(\mathbf{x},t\right)\right] \tag{2.2}$$

where, N is the number of delta functions and $w_{\alpha}\left(\mathbf{x},t\right)$ is the weight of node α, and

$$\bar{\delta}\left[\boldsymbol{\xi}-\boldsymbol{\xi}_{\alpha}\right]=\prod_{j=1}^{N_s}\delta\left(\xi-\xi_{j\alpha}\right) \tag{2.3}$$

Here $\boldsymbol{\xi}_{\alpha}\left(\mathbf{x},t\right)$ is the property vector of node α and of length N_s. If $N_s=1$ the distribution is mono-variate and if $N_s=2$ the distribution is bivariate. By using Eq. (2.2) any integral expression involving the distribution $f\left(\boldsymbol{\xi};\mathbf{x},t\right)$ can be transformed into a summation and the closure problem is trivial. This is the common element between QMOM and DQMOM, as said earlier. They only differ in the procedure used to obtain weights (w_{α}) and abscissas (ξ_{α}). For the monovariate case QMOM is just like SMOM where the weights and abscissas are computed by simply forcing them to agree with an independent set of lower-order moments [48].

The kth moment (μ_k) of a particle size distribution is defined as:

$$\mu_k=\int_0^{+\infty}\xi^k f\left(\xi\right)d\xi=\sum_{\alpha=1}^{N}w_{\alpha}\xi_{\alpha}^k. \tag{2.4}$$

Consider a monovariate PBE for simplicity, since only monovariate prob-

lems are considered later. Then, the moment transformation of the PBE (Eq. 2.1) gives

$$\frac{\partial \mu_k}{\partial t} + \frac{\partial}{\partial x_i}\left[u_i \mu_k\right] - \frac{\partial}{\partial x_i}\left[\Gamma \frac{\partial \mu_k}{\partial x_i}\right] = \int_0^\infty S\left(\xi; \mathbf{x}, t\right) \xi^k d\xi = \bar{S}_k \tag{2.5}$$

The right hand side of Eq. (2.5) includes all the mechanisms that bring change in the number density function (f). For e.g., in the case of soot formation in hydro-carbon flames, these processes are nucleation, molecular growth, oxidation and aggregation, where as in the case of TiO_2 nanoparticles synthesis from flames, oxidation is not considered since it is negligible.

2.3.2 Source term evaluation for the different processes

2.3.2.1 Nucleation (J):

For nucleation, a uniform distribution of particles of size $0 \leq \xi \leq \varepsilon$ has been initially assumed, where, ε is the maximum size of the nuclei. The earlier experimental studies from literature on ethylene diffusion flames which are aimed at determining the soot primary particle size and volume fraction show the possible range as $\approx$ 15 nm to $\approx$ 40 nm [113–115]. In the present work ε, which is the maximum possible particle diameter of the nuclei is assumed to be 34 nm for soot particle modeling (as in a similar numerical study, [30]). For the case of TiO_2 particles modeling ε is approximated to be 1 nm^3 after mannual testing (please note that internal co-ordinate is volume in this case). Recently, for TiO_2 particles modeling in the group of Prof. Fox, authors assumed the following range for particle nucleation $0.07 \leq \xi \leq 0.2$ (ε) [79]. From the definition of uniform distribution of size range $a \leq \xi \leq b$ is equal to $\frac{1}{b-a}$. From the uniform distribution definition, Eq. (2.33) and from the nucleation rate $J\left(\mathbf{x}, t\right)$:

$$\bar{S}_k \approx \bar{S}_k^{(N)} = \int_0^\varepsilon \xi^k \, \frac{1}{\varepsilon} \, J\left(\mathbf{x}, t\right) d\xi \tag{2.6}$$

$$\bar{S}_k = \frac{\varepsilon^k}{k+1} J\left(\mathbf{x}, t\right) \tag{2.7}$$

2.3.2.2 Molecular growth (G) and Oxidation (O):

Please note that oxidation is relevant only in soot particle modeling. Here, growth and oxidation are evaluated together. During the oxidation acting on soot particle, its size reduces. Hence, oxidation is considered as negative source term:

$$G = G_{mg} - G_{ox}$$

If $G(\xi)$ is the rate of continuous change of the particle size ξ, the source term for molecular growth can be written from Eq. (2.5) as:

$$\bar{S_k} = \int_0^\infty \xi^k \frac{\partial}{\partial \xi} \left[G\left(\xi\right) f\left(\xi\right) \right] d\xi \tag{2.8}$$

Integrating by parts:

$$\bar{S_k} = k \int_0^\infty \xi^{k-1} G\left(\xi\right) f(\xi) d\xi \tag{2.9}$$

and applying the quadrature approximation.

$$\bar{S_k} = k \sum_{\alpha=1}^{N} w_\alpha \xi_\alpha^{k-1} G\left(\xi_\alpha\right) = k\, \mu_{k-1} G\left(\xi_\alpha\right) \tag{2.10}$$

2.3.2.3 Aggregation:

As the particle sizes in the present investigation are very small (usually smaller than 1 μm), Brownian aggregation phenomena is considered here. Brownian motion is the main aggregation process when the particles are small enough to be entrained by the turbulent eddies, and thus are not affected by velocity gradients (shear rate); they come into contact because of their random motion within the eddy, as a consequence of thermal agitation [116].

While modeling soot formation we have considered the particle diameter as the internal coordinate. If the internal co-ordinate is particle diameter then the Brownian aggregation rate is defined in terms of the collision radius (R_c) of the aggregates involved in the collision event. Birth (B)/Death(D) of particles due to collision of particles of size L_1 and L_2 are shown below:

$$\mathrm{B} = \frac{1}{2}\int_0^\infty \int_0^\infty \left(L_1^3 + L_2^3\right)^{\frac{k}{3}} \beta\left(R_{c1}, R_{c2}\right) f\left(L_1\right) f\left(L_2\right) dL_1 dL_2 \quad (2.11)$$

$$\mathrm{D} = \int_0^\infty \int_0^\infty L_1^k \beta\left(R_{c1}, R_{c2}\right) f\left(L_1\right) f\left(L_2\right) dL_1 dL_2 \quad (2.12)$$

Where, $\beta\left(R_{c1}, R_{c2}\right)$ is the frequency (kernel) of aggregation of two particles with collision radius R_{c1} and R_{c2}. Since $\bar{S_k} = \mathrm{B} - \mathrm{D}$
Applying the quadrature approximation gives:

$$\overline{S_k} = \frac{1}{2}\sum_{\alpha=1}^{N}\sum_{\gamma=1}^{N}\left(L_\alpha^3 + L_\gamma^3\right)^{\frac{k}{3}} \beta_{\alpha\gamma} w_\alpha w_\gamma - \sum_{\alpha=1}^{N}\sum_{\gamma=1}^{N} L_\alpha^k \beta_{\alpha\gamma} w_\alpha w_\gamma \quad (2.13)$$

where $\beta_{\alpha\gamma} = \beta\left(R_{c\alpha}, R_{c\gamma}\right)$.

Particle volume is considered as the internal coordinate for TiO_2 nanoparticles modeling. Therefore, now the aggregation term is defined in terms of particle volume. Birth (B)/Death(D) of particles due to collision of particles of size v_1 and v_2 are shown below.

$$\mathrm{B} = \frac{1}{2}\int_0^v \beta\left(v - \bar{v}, \bar{v}\right) f\left(v - \bar{v}\right) f\left(\bar{v}\right) d\bar{v} \quad (2.14)$$

$$\mathrm{D} = f\left(v\right)\int_0^\infty \beta\left(v, \bar{v}\right) f\left(\bar{v}\right) d\bar{v} \quad (2.15)$$

$$\text{B-D} = \frac{1}{2}\int_0^\infty \int_0^\infty \left[\left(v + \bar{v}\right)^k - v^k - \bar{v}^k\right] \beta\left(v, \bar{v}\right) f\left(v\right) f\left(\bar{v}\right) dv d\bar{v} \quad (2.16)$$

Applying the quadrature approximation gives:

$$\overline{S_k} = \frac{1}{2}\sum_{\alpha=1}^{N}\sum_{\gamma=1}^{N}\left[\left(v_\alpha + \bar{v}_\gamma\right)^k - v_\alpha^k - \bar{v}_\gamma^k\right] \beta\left(v_\alpha, v_\gamma\right) w_\alpha w_\gamma \quad (2.17)$$

where, $k = 0, 1, 2, ...2N - 1$

As discussed earlier nucleation and molecular growth do not require any a priory knowledge of the NDF in the present calculation. This is clearly

visible from Eq. (2.7) and Eq. (2.10). On the other hand the aggregation term contains the integral in its original form (see Eq. 2.12 and Eq. 2.15) and thus needs information about all weights and abscissas (see Eq. 2.13 and Eq. 2.17). Therefore, QMOM can only be reduced to SMOM in the special case when aggregation is neglected. Now, the solution obtained from SMOM in this case can be used to start QMOM simulations. The same applies to DQMOM, as explained in Section 2.4.

QMOM uses the well known Product Difference (PD) algorithm to find the weights and abscissas by inverting the moments. The detailed mathematical description of the PD difference algorithm is shown below [48].

2.3.3 Steps involved in QMOM solution procedure

Figure 2.1 shows the general solution procedure used for QMOM in combination with CFD (here *Ansys-Fluent*). The details of the PD algorithm are not shown in the diagram but the step by step procedure is explained in the following text. Please note that all the steps outlined below have been coded in our research group as a complex User Defined Function (UDF) in **C**.

Step 1 Normalize the PSD (division of all the moments with zeroth moment, μ_0). Without loss of generality, the final distributions (or weights) can always be multiplied by the correct value of μ_0.

Step 2 Construct a matrix (P) of order $2N+1$ from the normalized moments as shown below (when $N = 2$, P matrix is of order 5; with $N = 3$, P matrix is of order 7). Please note that only the first row of the P matrix is sufficient for the moment inversion.

$$P(i,1) = \delta_{i1} \tag{2.18}$$

$$P(i,2) = (-1)^{i-1}\,\mu_{i-1} \tag{2.19}$$

$$P(i,j) = P(1,j-1)P(i+1,j-2) - P(1,j-2) \times P(i+1,j-1) \tag{2.20}$$

where $\delta_{i1} = 0$ for $i \neq 1$ and $\delta_{i1} = 1$ for $i = 1$; $P(1,2) = \mu_0 = 1$ (as normalized with μ_0).

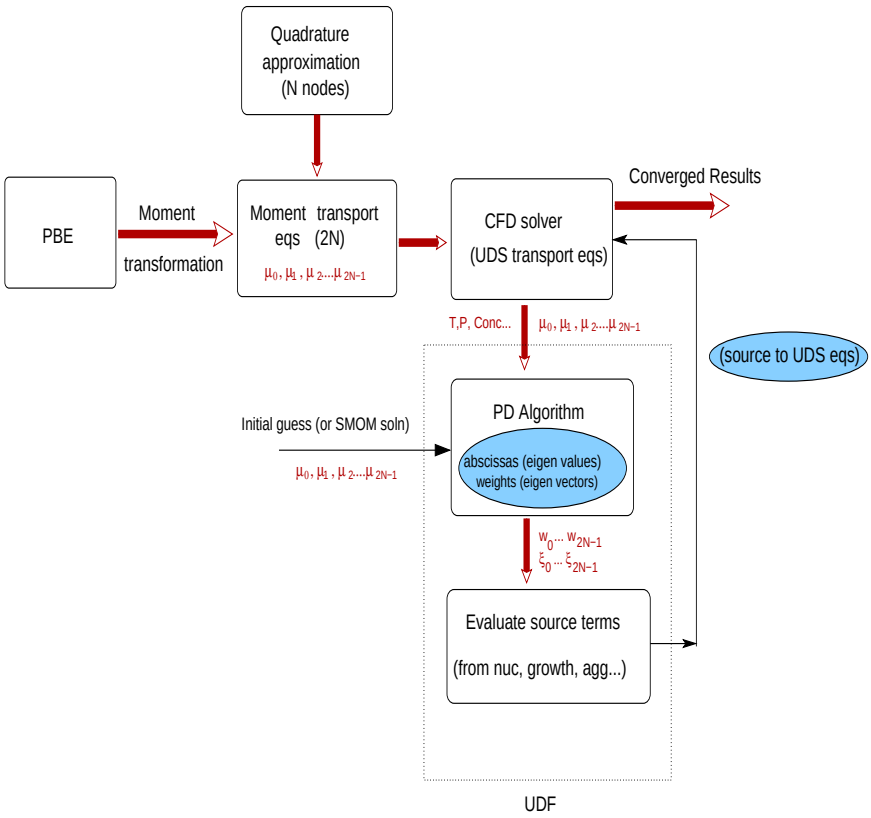

Figure 2.1: A general flow diagram of QMOM in combination with CFD solver

Step 3 Generate the α vector from the elements of P matrix (see Eq. 2.22):

$$\alpha(1) = 0 \tag{2.21}$$

$$\alpha(i) = \frac{P(1,i+1)}{[P(1,i)P(1,i-2)]} \quad \forall i \geq 2 \tag{2.22}$$

Step 4 Evaluate the diagonal a_1, $a_2 ... (a_{2N})$ and off-diagonal elements b_1, $b_2 ... (b_{2N-1})$ from the α vector, see Eq. (2.24):

$$a(i) = \alpha(2i) + \alpha(2i-1) \tag{2.23}$$

$$[b(i)]^2 = \alpha(2i+1)\alpha(2i) \tag{2.24}$$

Step 5 Construct the Jacobi matrix (J) from the diagonal and the co-diagonal elements. Please note that the order of the Jacobi matrix would be equal to the number of quadrature nodes N. Now, this Jacobi matrix is tridiagonal and symmetric, hence all the eigenvalues are real. This completes the PD algorithm.

$$\mathbf{J} = \begin{bmatrix} a_1 & b_1 & 0 \\ b_1 & a_2 & b_2 \\ 0 & b_2 & a_3 \end{bmatrix}$$

Step 6 Find out the eigenvalues (λ) and eigenvectors ($\boldsymbol{\nu}$) of this Jacobi matrix.

Step 7 The eigenvalues are directly the abscissas of the quadrature approximation, and the eigenvectors give the weights of the quadrature approximation, see Eq. (2.26).

$$\xi(i) = \lambda_i \tag{2.25}$$

$$w(i) = \mu_0 \nu_{i1}^2 \tag{2.26}$$

Step 8 Evaluate the source terms for the moment transport equations.

Step 9 Push these source terms into CFD solver as the source terms to UDS transport equations.

Step 10 With the CFD solver, evaluate the new set of moments.

Step 11 Repeat the Step 2 to Step 10 till the solution converges.

2.4 Solution of population balance equations using DQMOM

The Direct Quadrature Method of Moments (direct QMOM or DQMOM) is conceptually similar to QMOM, but the solver formulation is different. Solving the moment transport equations in QMOM is similar to that of SMOM, but the weights and abscissas are obtained from the PD algorithm. DQMOM does not solve for the moments, instead, it solves directly the variables appearing in the Quadrature approximation i.e., the weights and abscissas. Thus, DQMOM does not use the PD algorithm. Therefore, in DQMOM, the weights and the abscissas are transported in the computational domain with their own velocities. Thus, it leads to a strong coupling between internal co-ordinates and phase velocities.

Pioneering research work on DQMOM has been done by Marchisio and Fox [49], with a clear mathematical description and applications to various industrial problems including combustion, fluidized beds, precipitation, etc. [30, 81, 88, 107]. There are two main reasons for choosing DQMOM over QMOM, as discussed by authors. When the internal co-ordinates are integrated out to transform the PBE into its moment equations (as in QMOM), the strong coupling between the internal co-ordinates and the phase velocities is not accounted for in QMOM, while in DQMOM this coupling is retained. Secondly, the extension of QMOM to bivariate or higher PBE is quite cumbersome when NDF (f) depends on two or more internal co-ordinates [87, 111]. The main difficulty in this case is the lack of efficient numerical algorithms to invert the moments into w_i and ξ_i, like PD algorithm. Instead, DQMOM solves the transport equations of w_i and ξ_i directly in the domain and thus lowers the computational costs drastically. However, it now appears that DQMOM

has several stability issues and the choice between QMOM and DQMOM is a still a subject of controversy in the scientific literature. DQMOM has been applied in several cases to bivariate PBE and thus demonstrated its simplicity for such cases [84, 88]. Otherwise QMOM and DQMOM both appear very promising to combine with CFD codes.

2.4.1 Mathematical formulation

As explained earlier, the PBE is rearranged for DQMOM into a set of transport equations of weights (w_α) and weighted abscissas ($w_\alpha \xi_\alpha = \zeta_\alpha$). Substituting Eq. (2.2) in Eq. (2.1) and rearranging results in the following expressions (please see [49] for the detailed mathematical description on DQMOM):

$$\begin{aligned}
&\sum_{\alpha=1}^{N} \delta\left(\xi-\xi_\alpha\right)\left[\frac{\partial w_\alpha}{\partial t}+\frac{\partial}{\partial x_i}\left(u_{i\alpha} w_\alpha\right)-\frac{\partial}{\partial x_i}\left(\Gamma \frac{\partial w_\alpha}{\partial x_i}\right)\right] \\
&-\sum_{\alpha=1}^{N} \delta'\left(\xi-\xi_\alpha\right)\left\{\frac{\partial \zeta_\alpha}{\partial t}+\frac{\partial}{\partial x_i}\left(u_{i\alpha} \zeta_\alpha\right)-\frac{\partial}{\partial x_i}\left(\Gamma \frac{\partial \zeta_\alpha}{\partial x_i}\right)\right. \\
&\left.-\xi\left[\frac{\partial w_\alpha}{\partial t}+\frac{\partial}{\partial x_i}\left(u_{i\alpha} w_\alpha\right)-\frac{\partial}{\partial x_i}\left(\Gamma \frac{\partial w_\alpha}{\partial x_i}\right)\right]\right\} \\
&-\sum_{\alpha=1}^{N} \delta''\left(\xi-\xi_\alpha\right)\left[\Gamma \frac{\partial \xi_\alpha}{\partial x_i} \frac{\partial \xi_\alpha}{\partial x_i} w_\alpha\right]=S_\xi\left(\xi\right)
\end{aligned} \tag{2.27}$$

This can be rewritten:

$$\begin{aligned}
\sum_{\alpha=1}^{N}\left[\delta\left(\xi-\xi_\alpha\right)+\delta'\left(\xi-\xi_\alpha\right) \xi_\alpha\right] a_\alpha-\sum_{\alpha=1}^{N} \delta'\left(\xi-\xi_\alpha\right) b_\alpha \\
=\sum_{\alpha=1}^{N} \delta''\left(\xi-\xi_\alpha\right) C_\alpha+S_\xi\left(\xi\right)
\end{aligned} \tag{2.28}$$

Where,

$$\begin{aligned}
\frac{\partial w_\alpha}{\partial t}+\frac{\partial}{\partial x_i}\left(u_{i\alpha} w_\alpha\right)-\frac{\partial}{\partial x_i}\left(\Gamma \frac{\partial w_\alpha}{\partial x_i}\right) &= a_\alpha \\
\frac{\partial \zeta_\alpha}{\partial t}+\frac{\partial}{\partial x_i}\left(u_{i\alpha} \zeta_\alpha\right)-\frac{\partial}{\partial x_i}\left(\Gamma \frac{\partial \zeta_\alpha}{\partial x_i}\right) &= b_\alpha
\end{aligned} \tag{2.29}$$

and

$$C_\alpha = \Gamma \frac{\partial \xi_\alpha}{\partial x_i} \frac{\partial \xi_\alpha}{\partial x_i} w_\alpha \tag{2.30}$$

$u_{i\alpha}$ is the characteristic velocity associated with the delta function (or dispersed phase) α. This means that each delta function is convected in physical space with its own velocity. This provides a more suitable description of polydisperse multiphase systems than assuming that the velocity is identical for all phases. This is one of the main advantages of DQMOM discussed in [49].

It is important to know the delta function properties for further derivation.

$$\begin{aligned} \int_{-\infty}^{+\infty} \xi^k \delta\left(\xi - \xi_\alpha\right) d\xi &= \xi_\alpha^k, \\ \int_{-\infty}^{+\infty} \xi^k \delta'\left(\xi - \xi_\alpha\right) d\xi &= -k\xi_\alpha^{k-1} \\ \int_{-\infty}^{+\infty} \xi^k \delta''\left(\xi - \xi_\alpha\right) d\xi &= k\left(k-1\right)\xi_\alpha^{k-2} \end{aligned} \tag{2.31}$$

Now let us apply moment transformation to the above Eq. (2.28):

$$\left(1-k\right)\sum_{\alpha=1}^{N} \xi_\alpha^k a_\alpha + k\sum_{\alpha=1}^{N} \xi_\alpha^{k-1} b_\alpha = \bar{S}_k^{(N)} + \bar{C}_k \tag{2.32}$$

Here,

$$\bar{S}_k^{(N)} = \int_{-\infty}^{+\infty} \xi^k S_\xi\left(\xi\right) d\xi \tag{2.33}$$

and

$$\bar{C}_k = k\left(k-1\right)\sum_{\alpha=1}^{N} \xi_\alpha^{k-2} C_\alpha \tag{2.34}$$

For $N = 2$, as considered in what follows, Eq. (2.32) results in 4 unknowns for which we need 4 independent equations. These equations can be solved easily to determine a_α and b_α. If we consider 4 integer moments ($k = 0, 1, 2, 3$) we will end up with 4 algebraic equations ($k = 2N$). Knowing a_α and b_α, we can determine from Eq. (2.29) the new weights and abscissas with the known initial conditions. Solving for a_α and b_α is very simple in *Ansys-Fluent* CFD tool as this is in the general form of a transport equation. One needs to activate 4 scalar transport equations (UDS). These equations have source

terms a_1, a_2, b_1 and b_2. A simple matrix inversion (using a dedicated UDF) of Eq. (2.32) gives us these values, which are pushed back into CFD as the source terms for UDS transport equations (Eq. 2.29). Now the CFD solver enforces the transport equations of weights and abscissas with a_1, a_2, b_1 and b_2 as source terms. The detailed step by step procedure is shown in what follows.

We write the Eq. (2.32) in matrix notation: $\mathbf{A}\Phi = \mathbf{d}$. Here matrix $\mathbf{d}$ is the source term that holds all the processes responsible for the birth and death of the particles. Most of the time these processes are highly non-linear which makes the system unclosed. The linear system can be solved numerically at each grid node and at every time step to find $a(\mathbf{x}, t)$ and $b(\mathbf{x}, t)$. In some cases the rank of matrix A is not full $2N$, or it could be ill-conditioned. For instance this occurs when the abscissas ξ_α are non-distinct, leading to singularities and difficulties in convergence. Hence, one has to be careful during the calculation and check that the matrices involved do not become singular. As told earlier, the overall stability of DQMOM is still an issue and the subject of many scientific discussions.

For $N = 2$ the general matrix construction looks as shown below

$$\mathbf{A} = \begin{bmatrix} 1 & 1 & 0 & 0 \\ 0 & 0 & 1 & 1 \\ -\xi_1^2 & -\xi_2^2 & 2\xi_1 & 2\xi_2 \\ -2\xi_1^3 & -2\xi_2^3 & 3\xi_1^2 & 3\xi_2^2 \end{bmatrix}$$

$$\Phi = \begin{bmatrix} a_1 & a_2 & b_1 & b_2 \end{bmatrix}^T$$

$$\mathbf{d} = \begin{bmatrix} \overline{S_0} & \overline{S_1} & \overline{S_2} + \overline{C_2} & \overline{S_3} + \overline{C_3} \end{bmatrix} \tag{2.35}$$

2.4.2 Source terms evaluation for the different processes

In the case of DQMOM the source terms are all similar to that employed for QMOM. The interested reader should look back at Section 2.3.2.

2.4.3 Steps involved in DQMOM

Figure 2.2 is the general solution procedure used for the solution of DQMOM in combination with CFD solver. The sequence of steps used in DQMOM is explained below.

Step 1 Formulate the PBE into set of transport equations of weights and weighted abscissas (see Eq. 2.29) by rearranging and using moment transformation.

Step 2 Evaluate the source terms (see Eq. 2.33), start first with an initial guess/SMOM solution.

Step 3 Solve the system of equations using any efficient matrix inversion algorithm (by using a UDF) to obtain $a_1, a_2, ...b_1, b_2....$ (see Eq. 2.32).

Step 4 Push these values into CFD-solver, as these are the source terms for the user defined scalar transport equations (UDS, see Eq. 2.29).

Step 5 Using these values CFD-solver gives new set of weights and weighted abscissas in the next iteration.

Step 6 Repeat from Step 2 to Step 5 till the solution converges.

2.5 Numerical results with QMOM/DQMOM

Certainly, the number of quadrature nodes determines to some extent the accuracy of the solution. Published results from the literature show that quadrature methods with 2 or 3 nodes are usually sufficient to obtain the most important moments with the desired accuracy [107]. Of course, increasing the number of nodes leads in principle to improved predictions, but also to a rapid increase in computational time.

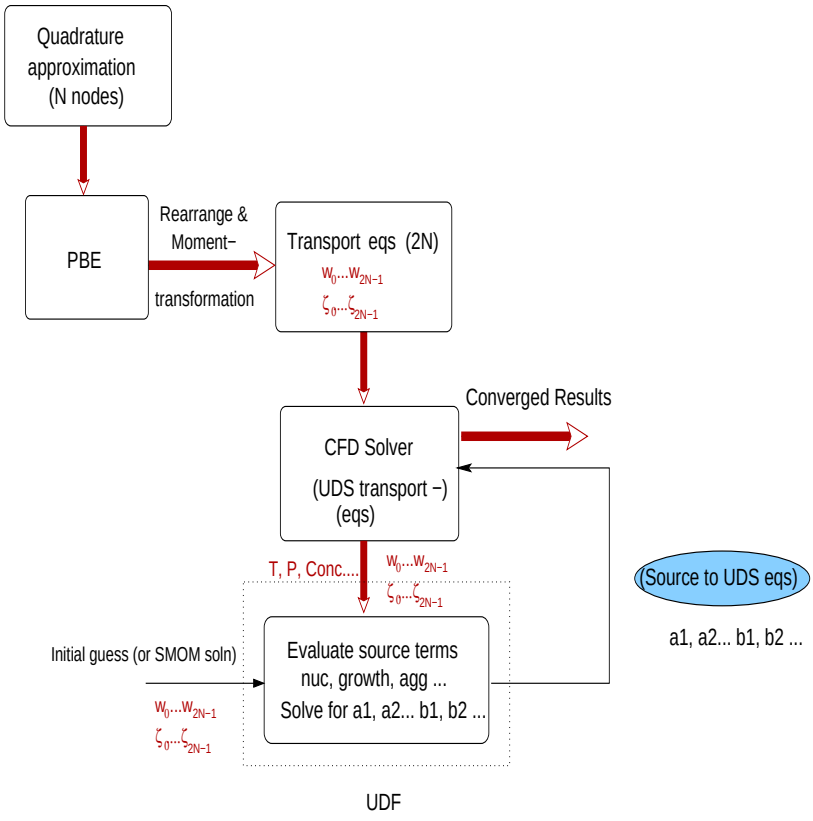

Figure 2.2: A general flow diagram of DQMOM in combination with CFD solver

The following discussion is solely aimed at understanding QMOM/DQMOM in dealing with the particulate problems considered here. The results are evaluated for few test problems and the modeling details are not discussed now, they will be given in later Chapters. The emphasis in the following results is only on the application of QMOM/DQMOM in describing nanoparticle (soot, TiO_2) evolution in typical flame configurations.

Figure 2.3 shows the first 4 moments of the NDF (f) of soot particles along the axis of a turbulent ethylene/air diffusion flame. Nucleation, molecular growth, oxidation and aggregation have been considered in the calculations. The calculations are performed with $N = 2$ nodes for QMOM and DQMOM, $N = 3$ nodes with QMOM. As seen in these figures the QMOM and DQMOM predicted the same behaviour and the results are almost identical for the first moments (μ_0, μ_1). As explained earlier both methods only differ in the implementation and should yield in principle identical results for uni-variate problem. However, a small difference is noticed in the moments predicted by both methods, becoming more visible for higher moments like μ_3. This is due to the differences in the numerical methods employed. The issue becomes more serious for higher moments due to bad conditioning. The dotted line in the figure is evaluated with 3 quadrature nodes. The results obtained with 3 nodes for this configuration do not differ very much from those obtained with 2 quadrature nodes, confirming statements from the literature. The relative difference for the only important quantities μ_0, μ_1 and μ_3 (almost identical, hence the curves are overlapped) is below 1%, and hence finally acceptable for practicle applications. Therefore, 2 nodes have been retained throughout this project in order to speed-up corresponding computations.

Figure 2.4 shows the contour plots of the first 4 moments of soot NDF obtained with QMOM and DQMOM for the flame configuration of [52]. The PBE is represented here with 2 quadrature nodes and particle length as internal co-ordinate. As seen in these figures, the predictions are almost identical with QMOM and DQMOM in qualitative as well as in quantitative behavior, with relative differences in peak values below 4% for the first moments.

Due to higher stability, QMOM has been also successfully implemented in the present study to predict TiO_2 nanoparticle evolution in turbulent $CH_4/O_2/Ar/TTIP$

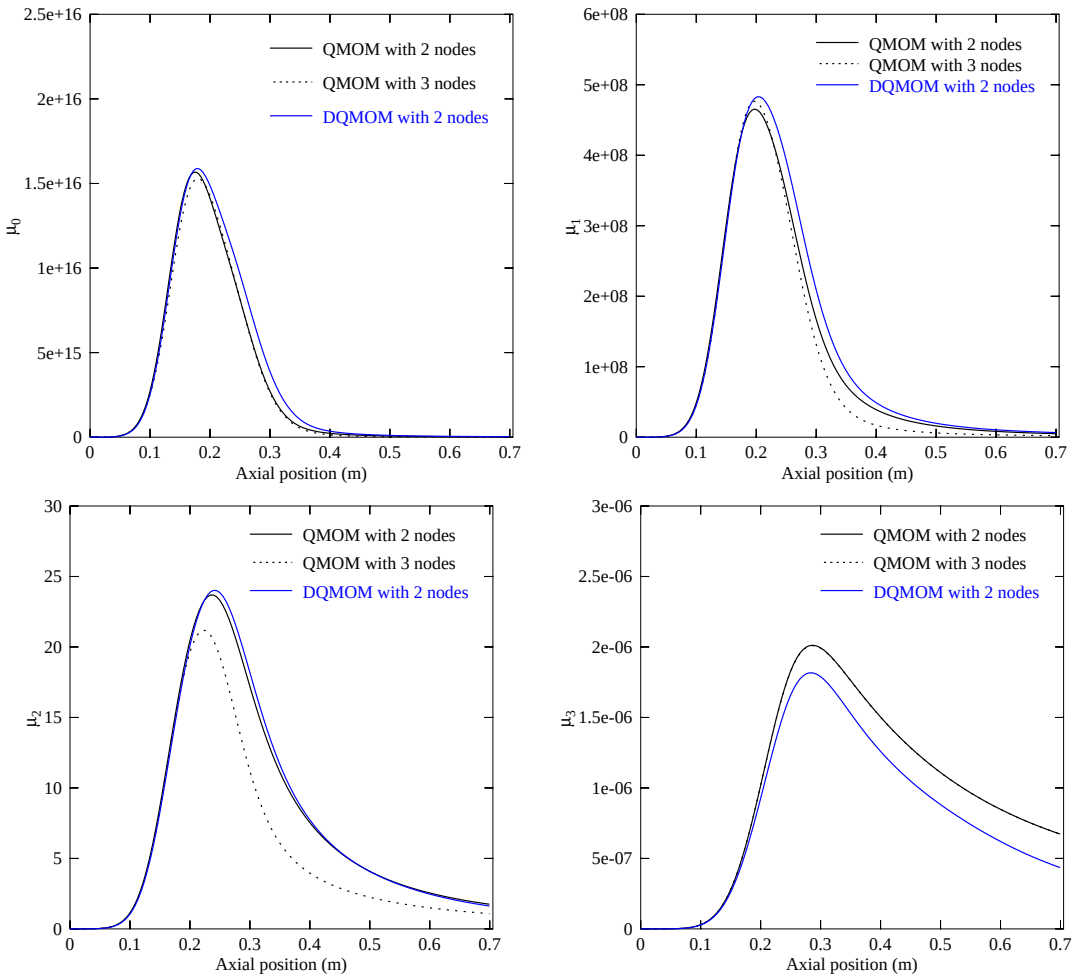

Figure 2.3: Comparison of moments of the NDF obtained with QMOM/DQMOM for the soot particle formation in turbulent ethylene/air flame [52]. Note the highly different y-scales. For μ_3 using 2 and 3 nodes the results are almost identical with QMOM, hence the curves are overlapped.

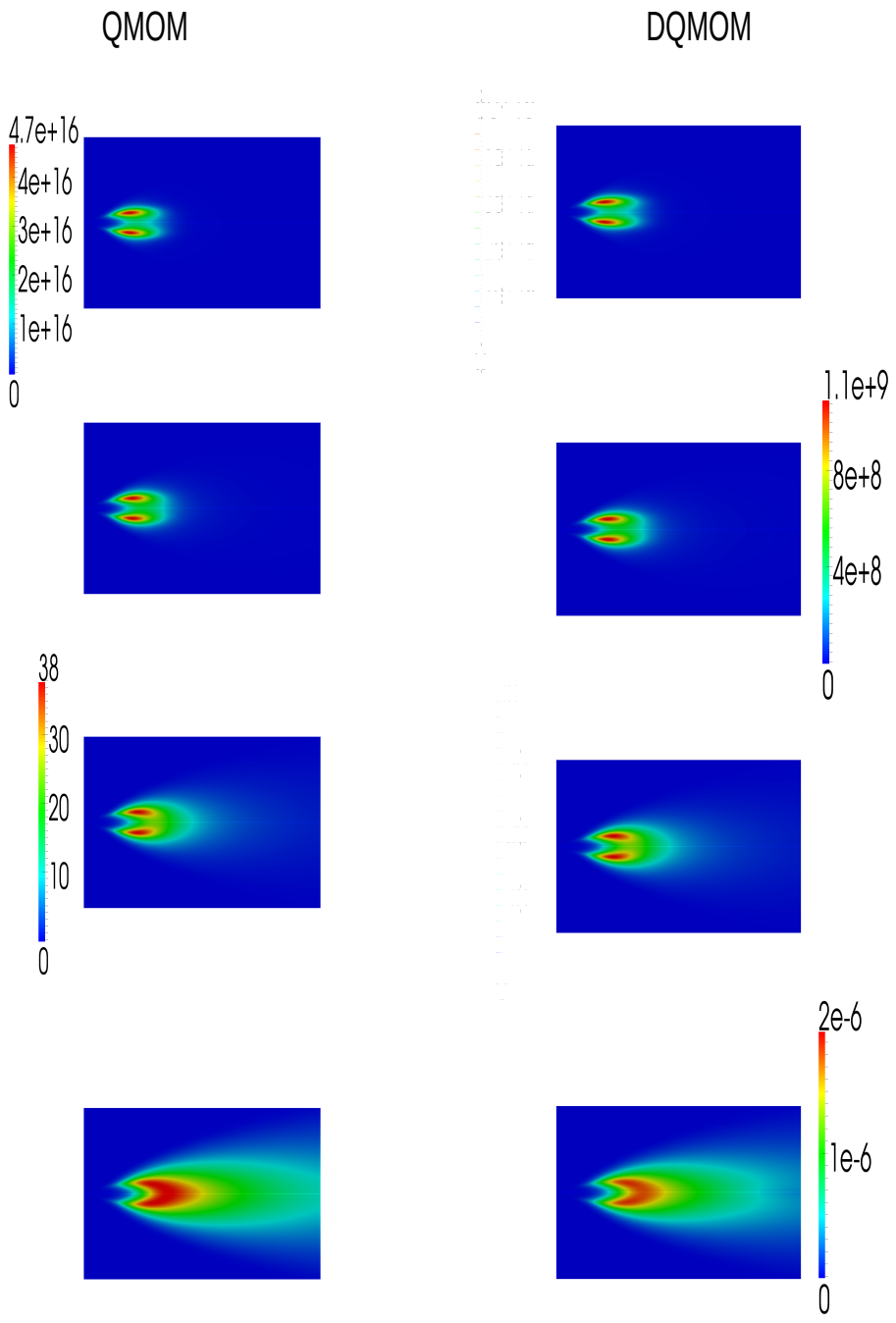

Figure 2.4: Contour plots of first 4 moments (from top μ_0 in $1/m^3$, μ_1 in m/m^3, μ_2 in m^2/m^3, μ_3 in ppm) of soot PSD obtained with QMOM and DQMOM for turbulent ethylene/air flame configuration of [52]

diffusion flame. In this case QMOM with 2 quadrature nodes has been considered and the source term includes nucleation, molecular growth and aggregation.

Chapter 3

Employed numerical models

The present chapter discusses the computational models used in various stages of this research work. As the investigations here involve particle phase and gas-phase simultaneously, the models are classified into two main groups called 'gas-phase models' and 'particle phase models'.

The governing equations and the models used in the present study are depicted in Fig. 3.1. The industrial CFD solver *Ansys-Fluent* is employed to solve all the gas-phase transport equations. *Ansys-Fluent* is a finite-volume based numerical solver and solves here the so-called Favre-averaged Navier-Stokes equations. The evolution of the particle phase is represented with population balance equations (PBE) solved with moment based methods (QMOM / DQMOM), as described in the previous chapter.

3.1 Gas phase models

3.1.1 Computational Fluid Dynamics (CFD)

Computational fluid dynamics (CFD) provides solution for a wide range of engineering problems by solving governing mathematical equations such as conservation of mass, momentum, energy, species, etc., which describe the given system. In turbulent flows all the flow properties vary in a random and chaotic way. Direct numerical simulation (DNS) is limited to very simplified cases, where the time and length scales present in the system are small. One way of handling this is to solve for the mean flow field by averaging the balance

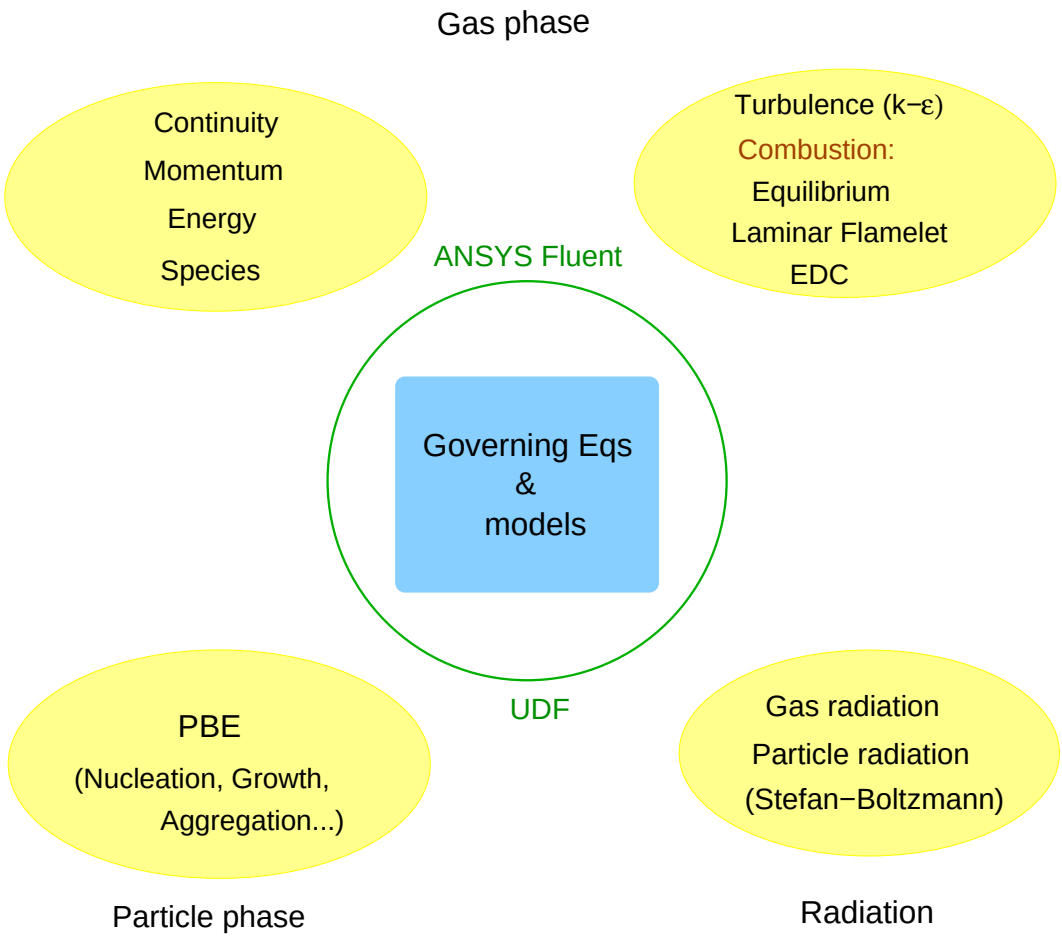

Figure 3.1: Governing equations and employed models

equations. The complete velocity can be decomposed into a mean value and a fluctuating value. So, at a given time, the instantaneous velocity is the sum of the mean value and the fluctuating value: $u(t) = \bar{u} + u'$, where $\bar{u}$ is the mean velocity and u' is the fluctuating velocity. Using this time averaging in the Navier-Stokes (N-S) equations is called Reynolds-averaging technique. It results in unclosed terms (e.g. Reynolds stresses, $\overline{u_i' u_j'}$). To close these equations one needs to define a suitable model. Reynolds Averaged Navier-Stokes (RANS) modeling is a good approach for flows where there is no appreciable change in density (incompressible flows). In turbulent flames, fluctuations of density also exist because of the thermal heat release. Reynolds-averaging would then induce additional terms, which must be modeled explicitly. This is an additional difficulty. To avoid that, Favre (or mass-weighted) averaging is instead employed [117]. Favre average on a component is shown with '$\sim$' over

it : $u(t) = \tilde{u} + u''$, and $\tilde{u} = \frac{\overline{\rho u}}{\bar{\rho}}$. This averaging results in similar equations to that appearing in Reynolds-averaging of incompressible flows. The unclosed Reynolds stresses are similarly closed with appropriate turbulence models. The simplified Favre-averaged balance equations for the present problem are shown below.

Continuity equation :

$$\frac{\partial \bar{\rho}}{\partial t} + \frac{\partial \bar{\rho}\tilde{u}_i}{\partial x_i} = 0 \tag{3.1}$$

Momentum equation :

$$\frac{\partial \bar{\rho}\tilde{u}_i}{\partial t} + \frac{\partial \bar{\rho}\tilde{u}_i\tilde{u}_j}{\partial x_i} = -\frac{\partial \bar{p}}{\partial x_i} + (\nu + \nu_t)\frac{\partial^2 \bar{\rho}\tilde{u}_i}{\partial x_j \partial x_j} + \frac{\partial \widetilde{\bar{\rho}u_i''u_j''}}{\partial x_i} + \bar{\rho}g \tag{3.2}$$

Scalar transport equation for the αth component :

$$\frac{\partial \bar{\rho}\tilde{\phi}_\alpha}{\partial t} + \frac{\partial \bar{\rho}\tilde{\phi}_\alpha\tilde{u}_i}{\partial x_i} = (\Gamma + \Gamma_t)\frac{\partial^2 \bar{\rho}\tilde{\phi}_\alpha}{\partial x_i \partial x_i} + \frac{\partial \widetilde{\bar{\rho}\phi_\alpha''u_i''}}{\partial x_i} + \widetilde{S(\phi)} \tag{3.3}$$

Energy equation in terms of total enthalpy $\tilde{h}_t$, with $h_t = h + \frac{u_i u_i}{2}$:

$$\frac{\partial \bar{\rho}\tilde{h}_t}{\partial t} + \frac{\partial \bar{\rho}\tilde{h}_t\tilde{u}_i}{\partial x_i} = \frac{\partial \bar{p}}{\partial t} - \frac{\partial \widetilde{\bar{\rho}u_i''h_t''}}{\partial x_i} + \frac{\partial}{\partial x_i}\left(\overline{\mathscr{J}_i^h} + \overline{u_i\tau_{ji}}\right) + \overline{u_iF_i} + \widetilde{S(h)} \tag{3.4}$$

where $\bar{\rho}$ and $\bar{p}$ are the mean density and pressure, respectively, $\tilde{u}_i$ is the Favre-averaged value of the ith component of the fluid mean velocity, u_i'' is the ith component fluctuation velocity. $\bar{\phi}$ and ϕ'' are the mean and fluctuating concentration of the αth scalar, ν, ν_t are kinematic and turbulent viscosities respectively; Γ, Γ_t are molecular and turbulent diffusivities respectively; $\widetilde{S(\phi)}$ is Favre-averaged chemical source term, $\tilde{h}_t$ is Favre-averaged total enthalpy, h_t'' is its fluctuating component, $\overline{\mathscr{J}_i^h}$ is averaged enthalpy diffusive flux, $\overline{u_i\tau_{ji}}$ and $\overline{u_iF_i}$ denote respectively the averaged power due to viscous and body forces, $\widetilde{S(h)}$ is Favre-averaged heat source. In the present case this source is due to radiative heat transfer, is evaluated through a User Defined Function (UDF) and provided as a source term to energy transport equation in *Ansys-Fluent*. Repeated indices imply summation.

The Reynolds stresses in Eq. (3.2) are closed by $k - \epsilon$ turbulence model. The simplest models for turbulent flows are those based on the concept of tur-

bulent viscosity (μ_t) and turbulent diffusivity (Γ_t). We have always used $k-\epsilon$ turbulence model, one of several available models from the literature. This model is very simple, very widely used, requires moderate computational time and has been successfully validated for the present flow problem (non-swirling jet flows) [118]. According to this model, Γ_t is evaluated from turbulent kinematic viscosity (ν_t).

$$\nu_t = C_\mu \frac{k^2}{\epsilon} \tag{3.5}$$

Here, $C_\mu = 0.09$, k, ϵ are turbulent kinetic energy and turbulent dissipation rate respectively, and $\Gamma_t = \frac{\nu_t}{\mathrm{Sc}_t}$, where Sc_t is the turbulent Schmidt number (ratio of momentum diffusivity to mass diffusivity, $\frac{\nu_t}{\Gamma_t}$), assumed equal to 0.7 as usual.

3.1.2 Non-premixed turbulent combustion

In non-premixed combustion fuel and oxidizer are not mixed a priory. Instead they enter seperately into combustion zone. Later, the mixing takes place due to convection, turbulent and molecular interdiffusion. Since diffusion is the rate-controlling process, this configuration is often known as diffusive combustion and the corresponding flames are known as diffusion flames. Since the time needed for turbulent mixing (τ_ϕ) is typically much larger than the time needed for combustion (τ_α) the assumption of infinitely fast chemistry (or local chemical equilibrium) usually appears to be appropriate. This assumption introduces an important simplication in modeling turbulent non-premixed flames [119], as detailed in later sections.

In the present work, first studies of soot production in turbulent/ethylene flames use equilibrium chemistry approximation. In later cases, a considerably refined description of gas-phase chemistry has been achieved by employing laminar flamelet modeling and describing chemical kinetics with 36 species and 219 chemical reactions [120]. Then turbulence and chemistry interactions are modeled through presumed PDF approach. For single mixture fraction cases, *Ansys-Fluent* uses an assumed shape β-function, since it accurately represents experimentally observed PDFs of mixture fraction.

When modeling later TiO_2 particles in CH_4-O_2-Ar diffusion flames, Eddy Dissipation Concept (EDC) model has been applied. In the following sections, a short description of these combustion models are given.

3.1.3 Gas phase chemistry

Due to the complexity of turbulent flows and chemical kinetics, as well as their interaction, it is extremely difficult to obtain direct numerical solutions by DNS. Consequently the interaction between turbulence and chemistry must be usually modeled [121]. In turbulent combustion modeling, the chemical source term is the main closure difficulty. Good amount of research has been done and is still going on to develop better models for this closure. Approximate closure depends on range of chemical (τ_α) and turbulent (τ_ϕ) time scales. It is proved in the literature that, in the equilibrium-chemistry limit an accurate closure can be developed by using the mixture fraction (Z) PDF. Mixture fraction is the scaled mass fraction of unburnt fuel (C, H) in the local mixture with $Z = 1$ in pure fuel and $Z = 0$ in pure oxidizer. The problem can be greatly simplified when we reformulate the problem in terms of the mixture fraction (Z) under the assumption of equilibrium-chemistry limit. Here, it is assumed that all the chemical species reach their equilibrium values much faster than the characteristic time scales of flow, i.e $\tau_\alpha \ll \tau_\phi$ (large Damkhöler number, Da=$\frac{\tau_\phi}{\tau_\alpha}$). One additional assumption made in the derivation is that the molecular diffusion coefficients are equal for all species. This assumption results in a unique mixture fraction definition. Thus, under these assumptions the reacting scalars can be represented through the mixture fraction. The only PDE that must be solved is that of the mixture fraction. Please note that mixture fraction is a conserved scalar quantity, therefore its governing equation does not have any chemical source term in it [117, 122].

The Favre-averaged mixture fraction transport equation is shown below:

$$\frac{\partial(\bar{\rho}\tilde{Z})}{\partial t} + u_i \frac{\partial(\bar{\rho}\tilde{Z})}{\partial x_i} = (\Gamma + \Gamma_t) \frac{\partial^2(\bar{\rho}\tilde{Z})}{\partial x_i x_i} \tag{3.6}$$

Now the numerical simulation of turbulent combustion is greatly simplified to a simple mixing problem and the difficulties associated with closing non-

linear mean reaction rates are avoided. Temperature, composition and density will be calculated at different points knowing mixture fraction PDF. Since the mixture fraction PDF is not known a priory, it must be modeled by solving an appropriate transport equation or by assuming a functional form. The most widely used approach is the presumed PDF method, in which a known distribution function is chosen to represent the mixture fraction PDF. For a one-component mixture fraction vector a β-PDF is often employed. A chemical look-up table is created and the mean values of temperature, mole fraction and density are saved at different values of mixture fraction in this table. This is the common solution procedure for both the equillibrium combustion model and the laminar flamelet combustion model.

3.1.4 Equilibrium combustion model

When we assume that chemical reactions are infinitely fast ('mixed is burnt') then the equilibrium combustion model can be used. In this case all the species tranport equations can be reduced to transport a single equation of mixture fraction (Z).

As already explained previously, the emphasis of the present work is not set on the extremely difficult issue of gas-phase or surface kinetics. Therefore, gas-phase chemistry is described very simply in first simulations by using a mixture fraction approach with equilibrium chemistry approximation, while turbulence/chemistry interactions are modeled through a presumed β-PDF approach, solving transport equations for mixture fraction $\tilde{Z}$ and for its variance $\widetilde{Z''^2}$ [117]. Twenty chemical species (C_2H_4, O_2, H_2, CO, CH_4, CO_2, H_2O, C_2H_2, OH, H, O, C_6H_6, C_4H_2, C_2N_2, C_4H, C_3H_2, H_2CCCCH, C_2H_6, C_2N, N_2) are taken into account in the equilibrium calculation.

During this study, it appeared that equilibrium chemistry was sometimes insufficiently accurate. Further improvement in the gas-phase chemistry was achieved through laminar flamelet modeling. The main advantage of the flamelet approach is that it takes into account finite-rate kinetic effects.

3.1.5 Laminar flamelet combustion model

When the chemical reactions are fast (Da $>$ 1), but not infinitely fast (Da $\gg$ 1) the laminar flamelet approach is used instead. The laminar flamelet approach is based on a representation of a turbulent flame as an ensemble of streched laminar flame elements embeded in a turbulent flow and interacting with it. This model may be viewed as a direct improvement of the infinitely fast chemistry model, since it uses the same formalism, but with an additional parameter, the scalar dissipation rate (χ), thereby including finite rate chemistry effects [117]. Laminar flamelet combustion models allow to include detailed chemical mechanism and finite rate effects. A flamelet table must first be generated.

One key parameter of the flamelet structure is the scalar dissipation rate χ (see Eq. 3.7), which controls the reactant fluxes to the reaction zone and is related to the flow velocity gradients.

$$\chi = 2\Gamma|\nabla Z|^2 \tag{3.7}$$

In *Ansys-Fluent* the turbulence-chemistry interactions are modelled with a presumed β-PDF. The advantage of the flamelet combustion model is that it is still computationally efficient as it solves only two tranport equations (mean mixture fraction and its variance), but simultaneously incorporates finite-rate chemistry.

We have systamatically employed 10 flamelet profiles into the flamelet look-up table for all calculations employing laminar flamelet modeling in the present study.

3.1.6 Eddy Dissipation Concept Model (EDC)

Magnussen first developed the Eddy Dissipation Concept Model (EDC) for describing chemical reations in a turbulent flow. The turbulence energy cascade model is the basis for EDC. The model is developed on the fact that the molecular mixing between reactants, which is associated with the turbulence dissipation ϵ, takes place in concentrated, isolated regions (dissipative) that occupy only a small fraction of the total volume of the fluid [121]. Within these

small-scale regions, small-scale structures are found whose dimension is of the same magnitude as the Kolmogorov microscale. Within these structures, one can assume that the reactants are mixed homogeneously at molecular level. These structures thus create the reaction space for non-uniformly distributed reactants and now act as a well-mixed reactor. In this case, chemical reaction kinetics determine the speed of the process. Outside these small scales the reactants are not mixed and hence do not react. Therefore, in order to be able to treat these reactions within this space it is necessary to know the reaction volume and the mass transfer rate between the fine structures and the surrounding fluid. These dissipative regions and the mass transfer rates into surrounding fluid are solely determined by turbulence theory, thus enabling fast and accurate calculations of turbulent reactive flows, in particular turbulent combustion. Now, each reactive cell is split into reactive volume fraction (γ^3) and an inert fraction ($1-\gamma^3$). The volume fraction of the reactive portion is modelled as [123, 124]:

$$\gamma^3 = C_\gamma \left(\frac{\nu\epsilon}{k^2}\right)^{3/4} \tag{3.8}$$

where, C_γ is volume fraction constant and it is evaluated using model constants $C_{D1} = 0.134$ and $C_{D2} = 0.5$ as:

$$C_\gamma = \left(\frac{3C_{D2}}{4C_{D1}^2}\right)^{1/4} = 2.1377 \tag{3.9}$$

The time scale for the mass transfer (τ) from the small-scale structures to the surrounding fluid is [123, 124] :

$$\tau = C_\tau \left(\frac{\nu}{\epsilon}\right)^{1/2} \tag{3.10}$$

where, C_τ is a time scale constant which is equal to:

$$C_\tau = \left(\frac{C_{D2}}{3}\right)^{1/2} = 0.4083 \tag{3.11}$$

The advantage of the EDC model is that it can incorporate some amount of detailed chemistry and both fast and slow chemical reactions can be treated simultaneously allowing to describe extinction [125].

In order to make detailed chemistry calculations more efficiently *Ansys-Fluent* uses In Situ Adaptive Tabulation (ISAT). ISAT can accelerate the chemistry calculations by up to $2-3$ orders of magnitude [124], thereby reducing the computational time. The fine scales are represented as isobaric, perfectly stirred reactors in *Ansys-Fluent*.

However, it is shown in Chapter 6 that the default EDC model parameters over predicted the temperature field for the considered configurations. Therefore, a parameter analysis has been carried out to find better values. For all later simulations EDC parameters are finally taken as $C_\gamma = 2.1377$ (standard value) and $C_\tau = 3.4$.

In the following section particle phase models employed for modeling soot and TiO_2 are described.

3.2 Dispersed phase chemical and physical models

The detailed literature analysis of Chapter 1 shows that, the main processes are nucleation, surface growth, aggregation and possibly oxidation.

3.2.1 Particle phase models : Soot

As explained previously, the model combination proposed and validated in [30] has been retained as original model combination for initial predictions and as starting point for the optimization. As a consequence, the nucleation model introduced in [126] and the molecular growth model presented in [127] have been retained, both acetylene-based. Oxidation results only from O_2 molecules, as proposed in [38].

3.2.1.1 Nucleation, Growth and Oxidation rates

The rates of nucleation J, molecular growth G_g and oxidation G_o are finally written:

$$J = N_A \rho^2 T^{\frac{1}{2}} 6\ 10^6 \exp\left(-\frac{T_n}{T}\right) X_{C_2H_2} \tag{3.12}$$

$$G_g = \frac{6}{D_f \rho_s}\left(\frac{R_c}{R_{c0}}\right)^{\frac{3-D_f}{3}} 2\ M_s\ 6 \exp\left(-\frac{T_g}{T}\right)[C_2H_2] \tag{3.13}$$

$$G_o = \frac{p}{D_f \rho_s} T^{-\frac{1}{2}} 6.5 \exp\left(-\frac{T_o}{T}\right) Y_{O_2} \tag{3.14}$$

Here, X is mole fraction, Y is mass fraction, $M_s = 12$ g/mol is soot molecular weight, N_A is Avogadro's number, $[C_2H_2]$ represents the acetylene concentration. The parameters T_n, T_g and T_o are equivalent activation temperatures for nucleation, growth and oxidation, respectively.

The aggregation kernel β_{12}, which depends on the Knudsen number, $\mathrm{Kn} = \frac{2\lambda}{L}$ (the ratio between the molecular mean free path of gas molecules, λ and the particle radius, $L/2$) is evaluated by the Fuchs interpolation formula [30]:

$$\beta_{12} = 4\pi(D_1 + D_2)(R_{c1} + R_{c2}) \left[\frac{R_{c1} + R_{c2}}{R_{c1} + R_{c2} + (g_1^2 + g_2^2)^{\frac{1}{2}}} + \frac{4(D_1 + D_2)}{R_{c1} + R_{c2} + (c_1^2 + c_2^2)^{\frac{1}{2}}} \right]^{-1} \tag{3.15}$$

where,

$$\begin{aligned} c_i &= \sqrt{\frac{8 k_b T}{\pi m_i}} \\ D_i &= \frac{k_b T}{6\pi\mu R_{ci}} \left[\frac{5 + 4\mathrm{Kn}_i + 6\mathrm{Kn}_i^2 + 18\mathrm{Kn}_i^3}{5 - \mathrm{Kn}_i + (8+\pi)\mathrm{Kn}_i^2} \right] \\ l_i &= \frac{8 D_i}{\pi c_i} \\ g_i &= \frac{(2R_{ci} + l_i)^3 - (4R_{ci}^2 + l_i^2)^{\frac{3}{2}}}{6 R_{ci} l_i} - 2R_{ci} \end{aligned}$$

with m the particle mass and k_b the Boltzmann constant. The parameter R_c is the collision radius, which is defined in terms of the fractal dimension D_f of

the aggregate through

$$R_c = k_f \frac{L_0}{2} \left(\frac{V}{V_0} \right)^{\frac{1}{D_f}} \tag{3.16}$$

with V the aggregate volume. The subscript 0 indicates primary particles, assumed of size 15 nm, and k_f is the fractal prefactor of order unity. The present simulation results are mostly computed by considering a constant fractal dimension $D_f = 1.8$ and $k_f = 1$, since a sensitivity analysis as described later revealed that the predicted soot volume fraction (f_v) is not very sensitive against D_f.

In order to check this issue, fractal dimension D_f has been evaluated as described below for some cases. The evolution of the mean value of the fractal dimension is calculated as a function of characteristic fusion time (t_f, sometimes referred as characteristic restructuring time) and collision time (t_c) and changes its value during particle growth, aggregation, etc. Here, a characteristic number τ is defined, which can be correlated with D_f [128]:

$$\tau = \frac{t_c}{t_f} \tag{3.17}$$

The characteristic time t_c is determined by following approach, explained in [128]:

$$t_c = \frac{1}{\bar{\beta} m_0} \tag{3.18}$$

where, $\bar{\beta}$ is the aggregation kernel calculated with average particle diameter (mean aggregation kernel), m_0 is the number concentration of the particles (i.e, zeroth moment, $m_0 = \mu_0$).

The characteristic fusion/restructuring time t_f can be assumed for soot particles [30] as:

$$t_f = \sqrt{\frac{15\nu_t}{\epsilon}} \tag{3.19}$$

Here, ν_t is turbulent kinematic viscosity and ϵ is turbulent dissipation rate. For different values of τ, D_f is modelled as [128]:

$$D_\mathrm{f} = \begin{cases} D_{f,\min} + (D_{f,0} - D_{f,\max})^{1/\tau^s} & \tau \leq 1, \\ D_{f,\max} - (D_{f,\max} - D_{f,0})^{\tau^s} & \tau > 1, \end{cases} \tag{3.20}$$

If t_f is much smaller than t_c, adherent particles will nearly always be completely fused prior to the next collision event. Therefore, mostly isolated spherical particles will be formed with a fractal dimension $D_f = D_{f,\max} = 3$. In the opposite case, thus if t_c is much smaller than t_f, adherent particles will face their next collision event far before sintering has been terminated. Agglomerates with fractal dimensions around $D_f = D_{f,\min} = 1.8$ as common for cluster-cluster aggregation will be generated then.

Here, s is a parameter which determines the gradient of the above function, $D_{f,0} = D_f(\tau = 1)$ accounts for the fractal dimension at identical characteristic collision and fusion time and is assumed to be equal to the average value between the limiting cases ($D_{f,\min}$ and $D_{f,\max}$), thus equal to 2.4.

It has been shown later in the results that inclusion of variable fractal dimension does not play any noticeable role for the soot volume fraction (f_v) value, the most important quantity for our investigation. Therefore, it has been fixed to a value of 2.0 for all further calculations.

3.2.2 Particle phase models : TiO_2

The last part of the present study deals with the synthesis of TiO_2 nanoparticles from titanium tetraisopropoxide in CH_4-O_2 diffusion flames with Ar as precursor. TiO_2 nanoparticle evolution is represented by taking into account nucleation, growth and aggregation as the source terms. The detailed analysis of literature shows that there is a serious dearth of computational models for evaluating essential parameters and reaction rates. Nevertheless, following rate equations appear to be commonly accepted. Certainly, more and better experimental measurements are needed in the future.

3.2.2.1 Overall rate:

The overall thermal decomposition of titanium tetraisopropaxide ($Ti(OCH(CH_3)_2)_4$) occurs both by homogeneous gas phase reaction and on the surface of TiO_2 particles.

$$\frac{dC_{TTIP}}{dt} = -k_{ov} = -\left(k_g + k_s A\right) C_{TTIP} \tag{3.21}$$

where, C_{TTIP} is concentration (in mol/m^3) of titanium tetraisopropaxide (TTIP). A is the particle area concetration (m^2/m^3). k_{ov}, k_g and k_s are the rate constants of overall TTIP decomposition, nucleation and surface growth respectively. The underlying, global reaction reads:

$$\mathrm{TTIP} \longrightarrow \mathrm{TiO_2} + 4\ \mathrm{C_3H_6} + 2\ \mathrm{H_2O}$$

The overall reaction rate constant k_{ov} (1/s), derived from experimental data as in [129] is:

$$k_{ov} = 3.96\,10^5 \exp\left(\frac{-8479.7}{T}\right) \quad \text{for} \quad T = 500 - 670\ \mathrm{K} \tag{3.22}$$

3.2.2.2 Growth rate:

The surface reaction rate constant k_s (m/s) is obtained from [130]:

$$k_s = 10^9 \exp\left(\frac{-15155}{T}\right) \quad \text{for} \quad T = 660 - 700\ \mathrm{K} \tag{3.23}$$

3.2.2.3 Nucleation rate:

Knowing the overall decomposition rate of TTIP (k_{ov}) and the corresponding surface contribution (k_s), the nucleation rate (k_g in 1/s) is obtained through the following expression.

$$k_g = k_{ov} - A\,k_s \tag{3.24}$$

When the surface reaction rate is neglected, k_s=0 and $k_g = k$. Since both rates have been modeled completely independently, it happens that the surface reaction rate k_s (Eq. 3.23) becomes larger than the overall rate k_{ov}, (Eq. 3.22), which is obviously non-physical. In this case, the surface reaction rate is simply prescribed as $k_s = k_{ov}/A$ and $k_g = 0$, so that the mass balance is correctly preserved, following corresponding recommendations from the literature [80].

3.2.2.4 Expressions for nucleation, growth and aggregation

The rate of nucleation (J, #/m^3) and molecular growth (G, m^3/s) are [59]:

$$J = N_A\, k_g\, C_{TTIP} \tag{3.25}$$

$$G = k_s\, C_{TTIP}\, A_g\, N_A\, v_{p0} \tag{3.26}$$

where, N_A, A_g, v_{p0} are the Avagadro's number, mean particle surface area and initial volume of the titania monomer, respectively.

The employed brownian aggregation kernel $\beta(v_1, v_2)$ of particles of volume (v_1 and v_2) is:

$$\beta(v_1, v_2) = \left(\frac{3}{4\pi}\right)^{1/6} \left(\frac{6k_B T}{\rho_p}\right)^{1/2} \left(\frac{1}{v_1} + \frac{1}{v_2}\right)^{1/2} \times \left(v_1^{1/3} + v_2^{1/3}\right)^2 \tag{3.27}$$

3.2.3 Heat of reaction of TTIP decomposition

The gas-phase decomposition reaction of TTIP is endothermic [70]. Hence, it needs to be considered in the energy balance equation as negative source term. The needed thermochemistry data such as standard state enthalpy and specific heat capacity of all the reactants and the products are taken from [131]. The decomposition temperature has been considered to be 520 K. Note that all these values seem to be associated with a high level of uncertainty.

3.3 Radiative heat transfer

Soot particles are well known to be associated with a high level of radiation, but radiative heat transfer might also be important in the gas phase.

3.3.1 Gas-phase radiation in soot modeling

The radiation occuring in the gas-phase is modeled very simply by assuming a grey and optically thin medium. This means that all the emitted radiation leaves without self-absorption or scattering. This basic description is very commonly used in combustion applications [19, 132] as it is very simple and does not involve much computational effort. Obviously, it is only of limited accuracy and it must be checked if it is possible to obtain correct predictions

in general with such a crude description. Only the radiative heat transfer resulting from the gaseous species CO_2 and H_2O has been evaluated while modeling soot formation (Eq. (3.28)) due to their noticeable higher Planck coefficient and concentration. The contributions from all other gaseous species are considered negligible.

$$Q_{rad,\text{gas}} = -(p_{CO_2}\alpha_{CO_2} + p_{H_2O}\alpha_{H_2O})2\sigma\left(T^4 - T_\infty^4\right) \tag{3.28}$$

Here, p represents partial pressure, α is the Planck mean absorption coefficient describing the total emission from the medium. The employed values for α values at different temperatures have been obtained from [133], and are listed in Table 3.1.

T (K)	α_{CO_2} (m atm)$^{-1}$	α_{H_2O} (m atm)$^{-1}$
250	40	100
500	35	22
750	35	8
1000	30	5
1250	20	3
1500	12	2
1750	8	1
2000	5	0.8

Table 3.1: Planck mean absorption coefficient for the gases CO_2 and H_2O at various temperatures [133]

The values shown in Table 3.1 have been compared in recent years with newer estimates of the Planck mean absorption coefficient [134] and are found to be in good agreement for the case of H_2O while only slight differences are noted for CO_2. The value of α at any temperature is obtained by linear interpolation between the data of Table 3.1.

3.3.2 Soot radiation models

Considering the possible importance of this issue, three different but simple soot radiation models found in the literature and based on a grey medium and optically thin approximation have been considered and compared. All three are

implemented for the simulation of nonpremixed turbulent ethylene/air flames and are function of f_v, the main quantity evaluated with the particle phase models.

3.3.2.1 Radiation model I

The first radiation model, also employed in [30], reads:

$$Q_{rad,\text{soot}} = -\sigma a_s \left(T^4 - T_\infty^4\right) \tag{3.29}$$

where $a_s = C_0 f_v T$, σ is the Stefan-Boltzmann constant, a_s is the Planck mean absorption coefficient for soot and T_∞ is the surrounding environment temperature (always set to 300 K). The original proportionality coefficient was $C_0 = 2370 \pm 240$ m^{-1}K^{-1} [40].

3.3.2.2 Radiation model II

The second radiation model is taken from [39]:

$$Q_{rad,\text{soot}} = -C_1 f_v \left(T^5 - T_\infty^5\right) \tag{3.30}$$

with the original parameter value $C_1 = 2.77 \times 10^{-4}$ W/m^{3}K^5. This model is based on the optically thin assumption at the scale of computation. Therefore, sufficiently fine grids are necessary to ensure its validity. The fifth power of temperature results from the wavelength dependence of the absorption coefficient of soot.

3.3.2.3 Radiation model III

The third radiation model is taken from [32] but has been originally proposed in [135]:

$$Q_{rad,\text{soot}} = -\sigma f_v a_s \left(T^4 - T_\infty^4\right) \tag{3.31}$$

where $a_s = C_2 \rho_s \left[1 + 4.8 \times 10^{-4} \left(T - 2000\right)\right]$ and $C_2 = 1232$ m^{2}kg^{-1}.

As described in Chapter 5 these three soot radiation models are finally leading to a same optimal radiation model (also see [136]).

3.3.3 Gas-phase radiation in TiO_2 production

Here, only radiation occuring from gaseous species is considered. Gas-phase radiation is again modeled by assuming grey and optically thin medium. The radiative heat transfer resulting from the key gaseous species CO_2, H_2O, CO and CH_4 has been evaluated in this work due to their high Planck coefficient and/or concentration. The contributions from all other gaseous species are considered negligible. The Planck mean absorption coeficients of the considered species are evaluated as described in [137]. Finally the radiative source term reads:

$$Q_{rad,\text{gas}} = -(p_{\text{CO}_2}\alpha_{\text{CO}_2}+p_{\text{H}_2\text{O}}\alpha_{\text{H}_2\text{O}}+p_{\text{CO}}\alpha_{\text{CO}}+p_{\text{CH}_4}\alpha_{\text{CH}_4})2\sigma\left(T^4 - T_\infty^4\right) \quad (3.32)$$

Here again, p represents partial pressure, α is the Planck mean absorption coefficient.

Chapter 4

CFD-based Optimization (CFD-O)

In order to improve published models from the literature, optimization with evaluations obtained from Computational Fluid Dynamics (CFD) will be employed.

The aim of the present chapter is to provide the basic understanding of CFD-based Optimization (CFD-O) and the details concerning its implementation in the present work.

An in-house optimizer, OPAL (OPtimization ALgorithm) has been employed in the present CFD-O [10]. OPAL contains most of the frequently used optimization algorithms, such as Gradient Descent, Simplex and Genetic Algorithms (GA). The present optimization work involves at least 2 concurrent objective functions. Therefore, the multi-objective optimization algorithm based on GA has been chosen.

4.1 Objective functions

In the following, the computation of objective functions by comparison between experimental and simulation data for temperature and soot volume fraction (f_v) are discussed. The experimental flame configuration of Yang *et al.* [50], being recent and carefully characterized is always taken as target flame (flame I) for the optimization. Corresponding axial profiles of temperature and f_v are exemplified in Fig. 4.1 and Fig. 4.2 respectively. Symbols are

experimental data while dashed lines are the simulation results obtained with the original soot model combination of [30].

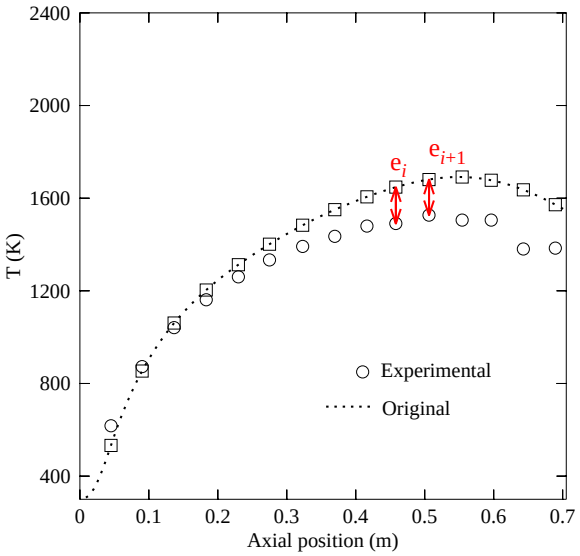

Figure 4.1: Comparison of experimental temperature along flame axis with simulation data obtained using original soot model (dotted line) for Flame I [50]

4.1.1 Objective function-1 ($OF1$):

The square symbols (□) in Fig. 4.1 are simulation data points obtained with the original model combination of [30] and corresponding to the locations where experimental data points (circles) are available. The differences between experimental and simulation results are exemplified in Fig. 4.1 with e_i, e_{i+1}... By adding up all such absolute errors for temperature, one obtains the first objective function, $OF1$, which should be minimized:

$$OF1 = |e_1| + |e_2| + |e_3| + |e_4| + \dots \tag{4.1}$$

4.1.2 Objective function-2 ($OF2$):

In Fig. 4.2 soot volume fractions (f_v) are shown using experimental data obtained from two different measurement methods (Laser Extinction (LE) and

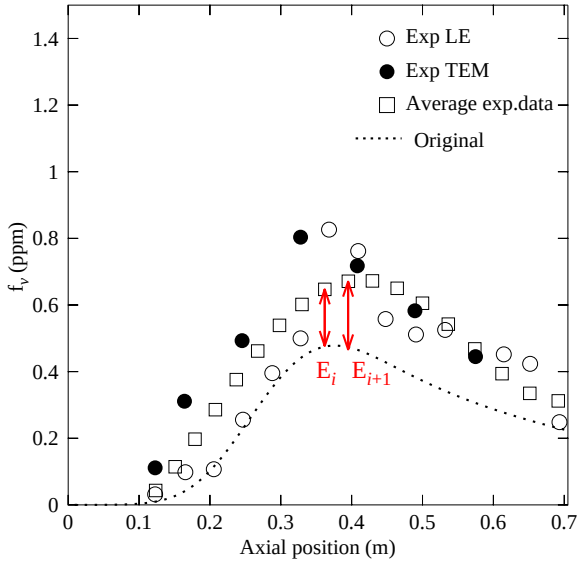

Figure 4.2: Comparison of experimental soot volume fraction f_v along flame axis (different symbols) with simulation data obtained using original model for Flame I [50]

Transmission Electron Microscopy (TEM)). Due to the considerable differences observed from the two measurements, average experimental results have been determined by a best fit of all experimental data points using a 5th order polynomial fit, represented by square symbols. Each simulation result is compared with the fitted experimental curve and absolute errors are again added as exemplified in Fig. 4.2 with E_i, E_{i+1}... This absolute error for soot volume fraction constitutes the second objective function, $OF2$, which should be minimized as well:

$$OF2 = |E_1| + |E_2| + |E_3| + |E_4| + \ldots \tag{4.2}$$

After discussing with specialists of experiments, it appeared that LE measurements should be considerably more accurate to determine f_v in the present case. Hence, in a later optimization step $OF2$ is obtained by comparing the simulation data against LE measurement data instead of average experimental data, as exemplified in Fig. 4.3.

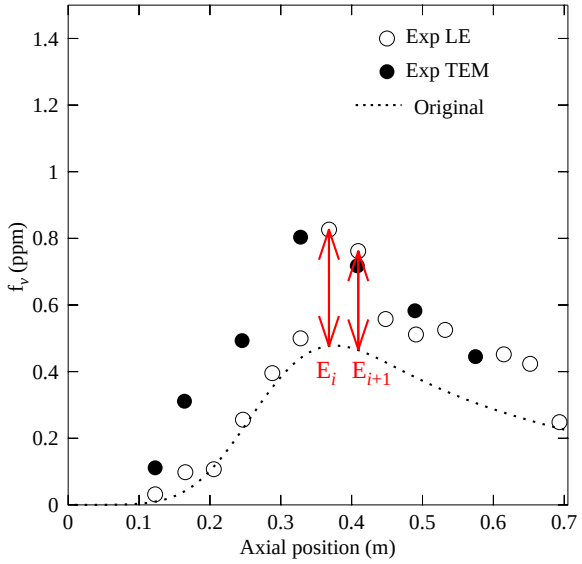

Figure 4.3: Comparison of experimental soot volume fraction f_v along flame axis (symbols) with simulation data obtained using original soot model for Flame I [50]

Optimization parameters

Activation temperatures of soot nucleation, molecular growth, oxidation and radiation model constant have been included in the optimization. The details concerning the number of parameters and the range considered in each optimization case are given in the respective section in Chapter 5.

4.2 Experimental uncertainties

It is important to note that, each data point is associated with some level of experimental uncertainty, in particular for such complex optical techniques. Even if the level of uncertainty is not always explicitly stated in the literature, it should be taken into account in order to avoid an "excessive" optimization, since the procedure will do its best by default to put the simulation results on top of the experimental points. To take into account a realistic level of measurement uncertainty, the experimental data have been associated with a tolerance level of ± 10% for temperature and of ± 20% for soot volume fraction. These ranges are employed to compute penalty points. All simulations leading to results within this range of uncertainty are associated with

a zero penalty and are therefore considered equally optimal. On the other hand, simulations falling outside this range become one penalty point for each corresponding position. This experimental uncertainty check has been only included in the first optimization study (Optimization-Case I in Chapter 5). Due to the additional complexity, and since it did not appear to modify the results, it has been latter deactivated.

4.3 Numerical optimization strategy

Four numerical tools are coupled for the present optimization, as shown in Fig. 4.4. CFD is used to solve flow, energy and species transport for the gaseous phase, coupled through User-Defined Functions with QMOM/DQMOM to obtain simultaneously the properties of the soot particle phase. After obtaining a converged flame and particle solution, MATLAB is used to evaluate the two objective functions, comparing simulation results with published experimental data in an automatic post-processing step. The optimization algorithm (GA) then manipulates the free parameters in an attempt to further minimize the objective functions. A subroutine coded in C manages automatically all the above computational tools in the right sequence.

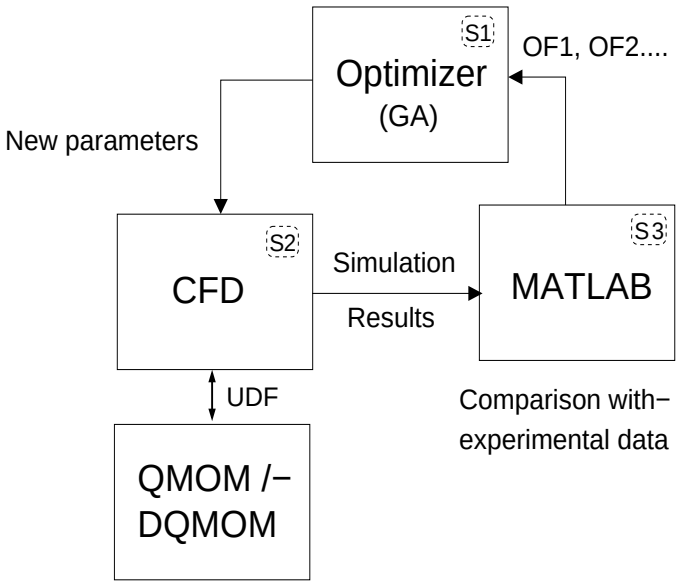

Figure 4.4: Numerical tools employed for the optimization, with calling sequence shown with S1, S2 and S3.

4.3.1 Computational procedure:

The optimization sequence has been shown in Fig. 4.4:

Step 1, S1: the Optimization algorithm (GA) generates the new individuals (i.e., parameter sets) within the given parameter space, from the previous population. In the first generation a quasi random population is generated based on Design Of Experiments (DOE).

Step 2, S2: Using these parameters CFD/QMOM-DQMOM simulations are carried out in order to evaluate the resulting fields.

Step 3, S3: Converged CFD/QMOM-DQMOM results are analyzed by comparison with experimental data and the objective functions $OF1$, $OF2$ (Eqs. 4.1-4.2) are computed using MATLAB.

Loop: These results are transferred back to the GA in order to generate the next generation.

Now, it is time discussing the obtained results.

Chapter 5

Improved soot prediction models for turbulent non-premixed ethylene/air flames

Part of this Chaper has been published in

1. *Chittipotula, T., Janiga, G. and Thévenin, D., Improved soot prediction models for turbulent non-premixed ethylene/air flames. Proceedings of the Combustion Institute, 33, (2011) 559-567.*

2. *Chittipotula, T., Janiga, G. and Thévenin, D., Optimizing soot prediction models for turbulent non-premixed ethylene/air flames. Chemical Engineering Science, 70, (2012) 67-76.*

Existing soot models for non-premixed ethylene/air flames often do not satisfactorily predict soot volume fraction. Due to intense energy exchange by radiative heat transfer, this leads to a situation where even basic scalar fields like temperature are inaccurately described. The objective of the present chapter is to develop an enhanced soot prediction model for such flames, valid for a wide range of flow and operating conditions, using CFD-based optimization. The otpimal models are developed sequentially in 3 steps. Those are referred here after as "Optimization-Case I" to "Optimization-Case III". These cases

differ in the employed models and/or in the parameters considered for the optimization.

5.1 Configuration

All turbulent non-premixed ethylene/air flames considered in this work have a similar geometry, as shown in Fig. 5.1(a). Pure ethylene enters into quiescent air through a nozzle and combustion takes place at atmospheric pressure (open configuration). As the domain is symmetrical with respect to the central axis, simulations are carried out in an axisymmetric configuration (Fig. 5.1(b)).

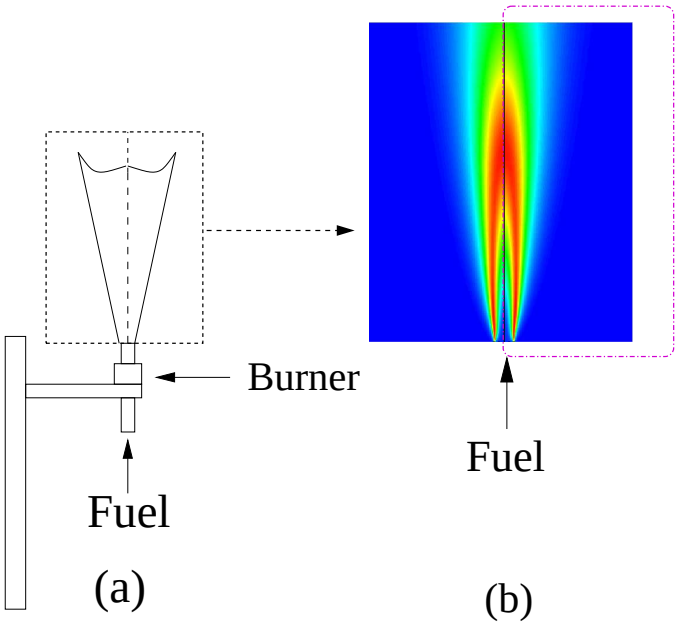

Figure 5.1: General configuration; (a) sketch of experimental set-up, (b) associated adapted computational domain

Grid generation has been carried out using the software Gambit with typically 20 000 grid points, used to discretize an axisymmetric computational domain of 300 mm (width) × 900 mm (length), kept identical for all flames. A non-uniform mesh is employed for all computations, with very fine cells near the axis and coarser cells near domain boundary. The size of the domain and the computational grid have been retained after a systematic study of the dependence of the results on the grid resolution and on the influence of outflow boundary conditions. In this manner, it has been verified that the obtained

fields only depend on the employed physical models.

Four different turbulent non-premixed ethylene/air flames [50–53] have been considered in this work. Internal nozzle diameter (D_i in mm), fuel mass flow rate ($\dot{m}$ in g/s), average exit velocity (u_i in m/s) and associated Reynolds number (Re) of the flames are listed in Table 5.1 (see on page 69).

The results in this chapter are arranged as follows: initial results are obtained from the "original soot models" of Zucca *et al.* [30]. These soot models are improved with CFD-O in following sections and referred as "improved soot models". Corresponding temperature, soot volume fraction contour plots and validations by comparison with experimental data are presented. The first flame [50] is systematically employed to determine the optimal model parameters. These optimal models are then used to determine temperature and soot fields for three other flames [51–53] in order to check their generality, hopefully showing an improved agreement compared to the original models.

Table 5.1: Experimental conditions considered in the simulations

Flame	D_i (mm)	$\dot{m}$ (g/s)	u_i (m/s)	Re	Reference
I	4.6	0.48	25.4	13 500	[50]
II	4.56	0.48	25.8	13 500	[51]
III	3.0	0.419	52.2	14 660	[52]
IV	2.18	0.209	48.7	12 000	[53]

5.2 Results with original soot models

The results in this section are obtained with the original soot models described in [30]. Figure 5.2 depicts the contours of temperature on the left (in K) and soot volume fraction on the right (in ppm). Soot volume fraction f_v and temperature are qualitatively similar. The maximum of f_v is found in regions of high temperature.

Comparison of experimental data with the simulation data along the axis of the flame is shown in Figs. 5.4-5.3. Temperature is over predicted whereas soot volume fraction (f_v) is strongly under predicted with the original model parameters. The peak soot volume fraction is at considerably lower value

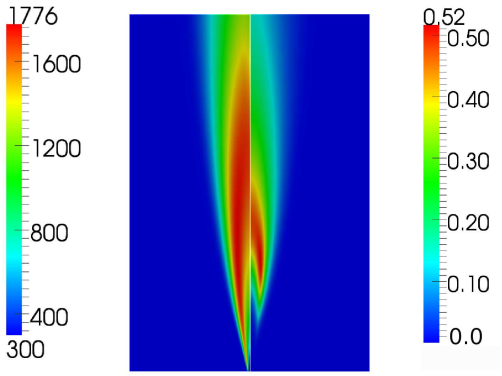

Figure 5.2: Contours of temperature in K (left symmetric half) and soot volume fraction (f_v, in ppm) (right symmetric half) for Flame I , evaluated from original soot models

($\approx$ 0.5 ppm, see Fig. 5.3) when compared with that of the experimental data ($\approx$ 0.8 ppm). The difference between the experimental data and simulation data for temperature is high as well as seen in Fig. 5.4 (more than 100 K). This temperature difference might lead again to strong modifications of f_v.

The observed trend is similar for all the other flames under investigation. Hence the results are not shown here. It can be concluded that the predictions are not satisfactory with the original models. Therefore, in later sections the results are presented for all the flames with improved version of these models, as obtained by CFD-based optimization.

5.2.1 Effect of fractal dimension

Before starting the optimization, the possible impact of the fractal dimension (D_f) is checked. Contours of collision-radius (R_c) for a fixed fractal dimension ($D_f = 1.8$) are first shown in Fig. 5.5. As seen in the figure, R_c is almost constant in the first portion of the flame (till $\approx$ 300 mm from the burner) due to the small influence of nucleation and beginning molecular growth on particle

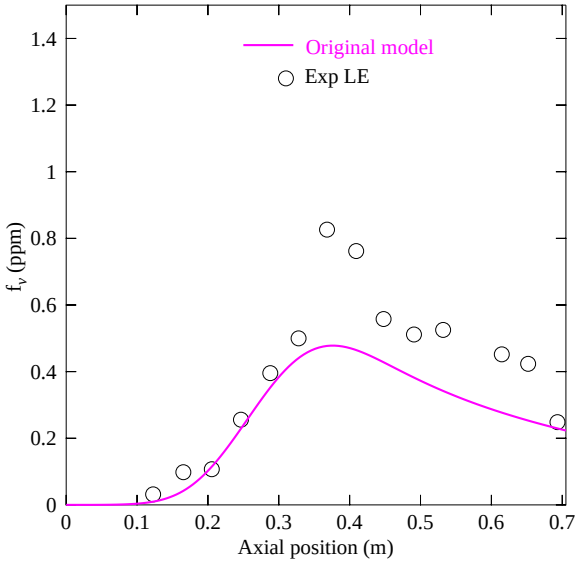

Figure 5.3: Axial profile of soot volume fraction for Flame I evaluated with original soot models from [30], compared to experimental measurements (symbols)

diameter. Afterwards, because of the onset of aggregation mechanism, the average diameter drastically increases. Axial profiles of collision radius are shown in Fig. 5.6 for various values of fractal dimension ($D_f = 1.8, 2.2, 2.6$ and 3.0). The above stated explanation is clearly confirmed by this figure. The rate of increase in collision radius is maximum after $\approx$ 400 mm from the inlet with maximum collision radius noted near the outlet. As seen in the Fig. 5.6, fractal dimension (D_f) has very significant effect on R_c. The increase in collision radius is 6 times greater for $D_f = 1.8$ (maximum $R_c \approx 220$ nm) when compared with $D_f = 3.0$ (maximum $R_c \approx 35$ nm). The higher the fractal dimension of the aggregate, the lower is its radius. It is clear, therefore, that particles with lower fractal dimension are more branched and porous.

Although effect of D_f is very significant on R_c, its effect on f_v is negligible, as shown in Fig. 5.7. Therefore in all further computations D_f has been kept constant ($D_f = 1.8$), since f_v is our variable of interest for practical applications.

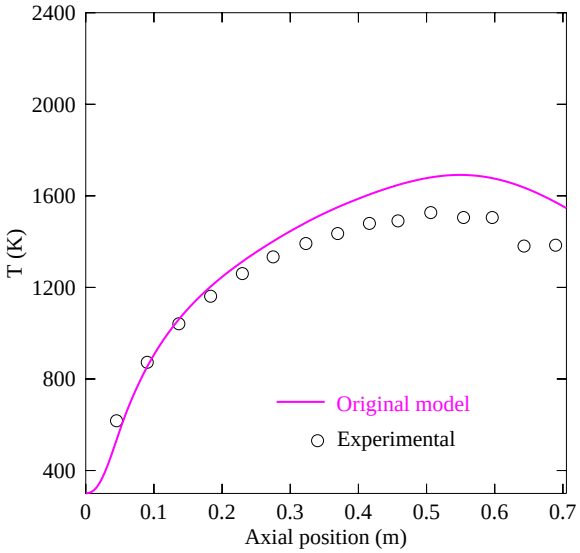

Figure 5.4: Axial profile of temperature for Flame I evaluated from original soot models

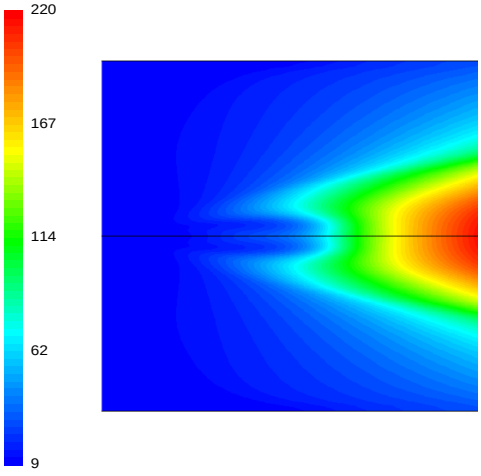

Figure 5.5: Contour plots of collision radius (R_c, in nm) for fixed fractal dimension, $D_f = 1.8$

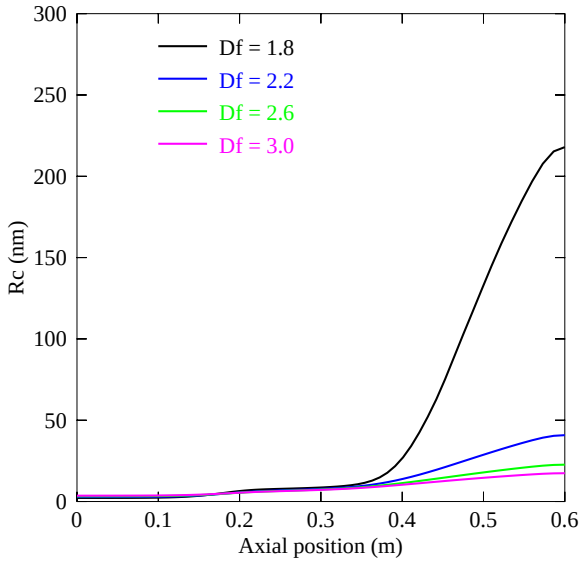

Figure 5.6: Axial profiles of collision radius (R_c, in nm) for different values of fractal dimension (D_f) for flame III

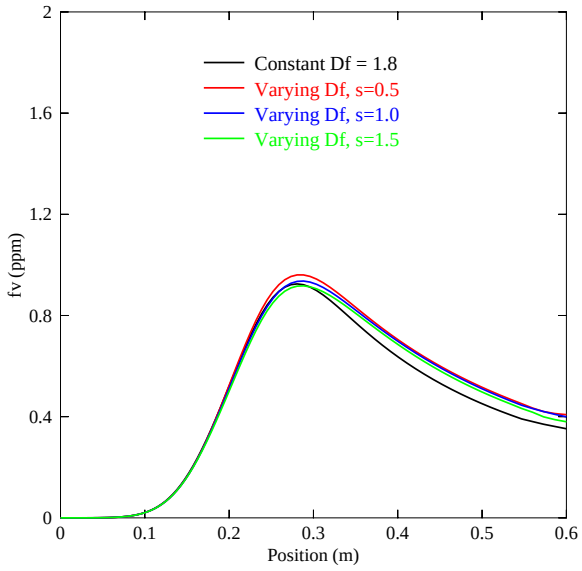

Figure 5.7: Comparision of axial profiles of soot f_v with constant & variable D_f (Eq. 3.20) for flame III

The soot models are now improved in three successive optimization steps. The next sections describe the different optimization cases, which differ mainly in the gas phase combustion model and/or in the optimization parameters. These cases are referred here as Optimization-Case I to Optimization-Case III.

5.3 Optimization-Case I

The emphasis in this case is completely on the particulate phase and not on gas-phase kinetics. Therefore, gas-phase chemistry is simply modeled with a mixture fraction approach combined with equilibrium chemistry, while turbulence-chemistry interactions are taken into account by a presumed β-PDF. The evolution of soot particles is described by physical models accounting for nucleation, surface growth, aggregation and oxidation. The Direct Quadrature Method of Moments is employed to solve the Population Balance Equations in a computationally efficient manner, assuming a mono-variate PBE with particle diameter as internal coordinate. The original soot model is optimized numerically by using Genetic Algorithms coupled with Computational Fluid Dynamics (CFD). The values of three model parameters, associated with nucleation, oxidation and soot particle radiation are optimized through comparison with recent experimental results. Two objective functions are formulated based on the difference between experimental and simulation results for temperature and soot volume fraction. After obtaining an optimal parameter set, the resulting model is further tested against three experimental configurations, leading to a good agreement and thus demonstrating a high level of generality.

The multi-objective optimization is carried out by considering two objective functions and three free model parameters. The two objective functions are the differences between experimental data and simulation results concerning the fields of temperature and of soot volume fraction (see Section 4.1, on page 61). The three free parameters have been selected after a sensitivity analysis of each model parameter appearing in the original formulation [30]. Optimization is based on the experimental results of [50], while three additional flame types are used to further ascertain the generality of the optimized solution.

5.3.1 Optimization parameters

A previous sensitivity analysis performed on all the parameters of the soot particle model (Eqs. 3.12-3.16) and radiation model (Eqs. 3.28-3.29) has demonstrated that nucleation, oxidation and radiation parameters dominate the prediction of soot volume fraction. Therefore, three optimization parameters have been retained in the present section: the activation temperature for nucleation (T_n), for oxidation (T_o) and the soot radiation constant (C_0). After some manual tests, the variation range for the three parameters has been prescribed as $42\,000 \leq T_n \leq 46\,100$ [K], $24\,000 \leq T_o \leq 26\,500$ [K], $2\,400 \leq C_0 \leq 5\,000$ [$m^{-1}K^{-1}$].

The final goal of the optimization is to find the optimal set of parameters T_n, T_o and C_0 within the given parameter space, in such a way that the two objective functions $OF1$ and $OF2$ are simultaneously minimized without any penalty.

Please see Chapter 4 to know about the details concerning the numerical procedure followed in CFD-based optimization (CFD-O). CFD-O is performed completely automatically in batch mode using 6 computing cores in parallel. In this manner, assessing the properties of one generation takes roughly 4 hours of computing time. As a whole, more than 60 different parameter sets have been tested by the optimization procedure. The optimization process has been able to identify a considerably better set of parameters compared to the original model, as documented in Figs. 5.8 and 5.9. The most important variable f_v was severely under predicted with the original model parameters. The predictions are improved significantly with the optimal set. The temperature profile becomes in very close agreement with the experimental data (Fig. 5.8). The peak soot volume fraction is much closer to the peak experimental value ($\approx$ 0.8 ppm), while it was considerably lower with the original model ($\approx$ 0.5 ppm). The profile of f_v is nevertheless slightly shifted towards the burner, a tendency observed in all further simulations as well (see later). The optimal model values are shown in Table 5.2 along with the relative change compared with the original model.

It is now essential to check the generality of the obtained set of parameters. Getting much better values for one configuration (in the present case,

experiment of [50]) would be of little use if other predictions become worse.

Table 5.2: Original and optimal model parameters for Case I

Parameter	Original	Optimal	% Rel. change
T_n [K]	46 100	42 140	−8.59
T_o [K]	26 500	26 218	−1.06
C_0 [$m^{-1}K^{-1}$]	2 485	3 593	44.0

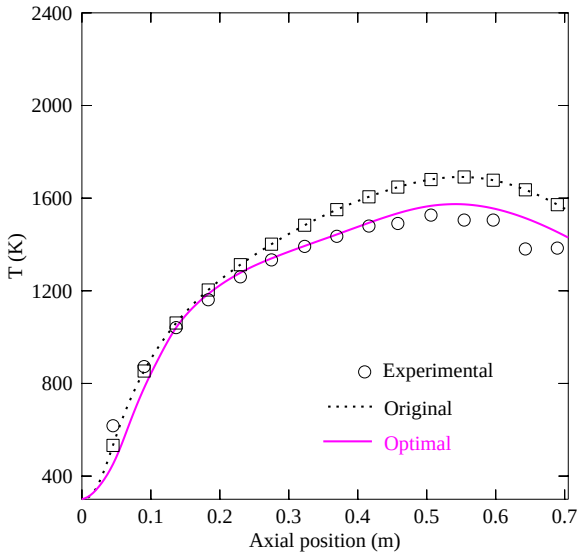

Figure 5.8: Comparison of experimental temperature along flame axis with original and optimal soot model for Flame I (Case I)

5.3.2 Results & Discussion on generality

As a consequence, all four turbulent non-premixed ethylene/air flames shown in Table 5.1 have been computed with the same (optimal) set of parameters. These flames are referred to as Flame I to IV. Flame I has been used to optimize the set of parameters and corresponding comparisons have already been shown in Figs. 5.8 and 5.9. Now, Flames II, III and IV are computed with exactly the same physical models, grid size and computational domain.

The contour plots of acetylene mass fraction, soot nucleation (J in $\#/m^3$) and growth (G in m/s) for Flame I with optimized models are shown in Fig. 5.10. As the soot empirical models for J and G are based on acetylene

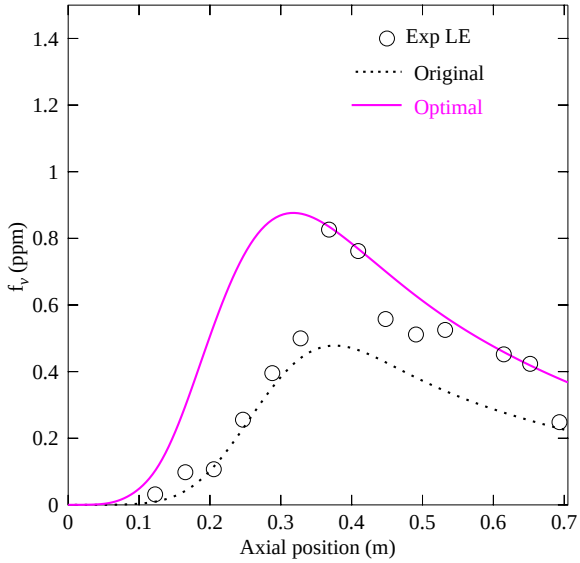

Figure 5.9: Comparison of experimental soot volume fraction f_v along flame axis with original and optimal soot model for Flame I (Case I)

species, they are active in and around the regions of high acetylene mass fraction. The contours of growth rate are observed to follow closely the acetylene concentration.

In Fig. 5.11 axial profiles of soot volume fraction are shown for Flame II. Experimental data are compared with simulation results both with the original and with the optimal model parameters. Using the original model, the predicted peak value of f_v is nearly 40% lower than experimental data. The optimal parameter set predicts almost exactly the peak soot volume fraction, while a slight shift in peak position towards the burner is again observed.

Axial profiles of temperature and soot volume fraction are shown for Flame III in Figs. 5.12 and 5.13, respectively. Once again, the agreement concerning temperature is tremendously better with the optimal model compared to the original formulation (Fig. 5.12). Simultaneously, the peak soot volume fraction is also better predicted with the optimal parameter set, while a shift towards an earlier soot production is again observed (Fig. 5.13). Note that these measurements are more than 20 years old and might therefore be associated with a higher experimental uncertainty, explaining larger differences between measurements and simulations, independently from the retained numerical model.

Figure 5.14 illustrates the contours of temperature (in K) and soot volume

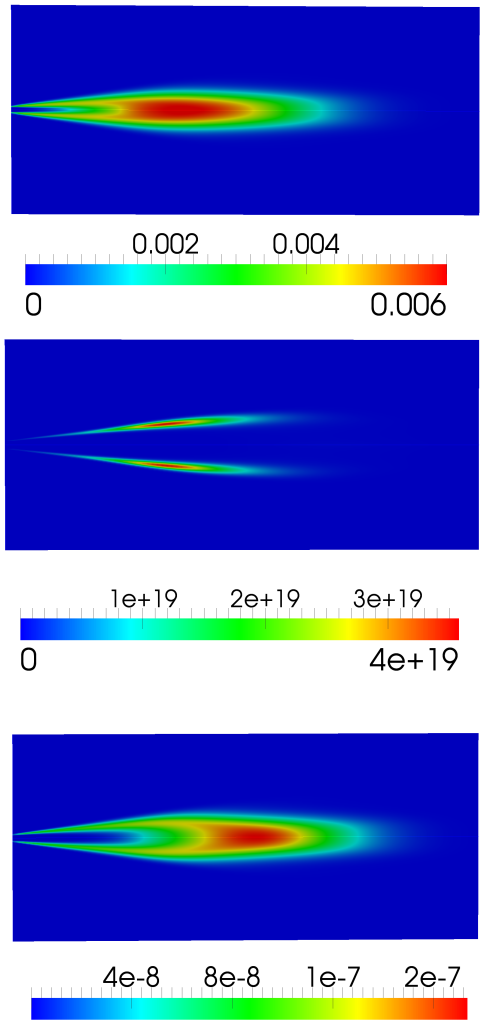

Figure 5.10: From top: Contour plots of acetylene mass fraction, soot nucleation (J, in $\#/m^3$) and growth (G, in m/s) respectively for Flame I [50] with optimal model

fraction (in ppm) for flame III with the optimal model. Once again, the qualitative and quantitave trend is similar to the experimental observations from literature as described in axial profiles of temperature and f_v. Contours of mean particle diameter (in nm) for flame III are depicted in Fig. 5.15. As seen, the mean particle diameter is lower in the first part of the flame, increases rapidly in the upper portion of the flame and reaches maximum mostly due to aggregation. The observed peak value of 322 nm could be even higher in reality (experimental data is not available for the comparison further downstream).

Recent experimental studies on turbulent non-premixed ethylene/air flames

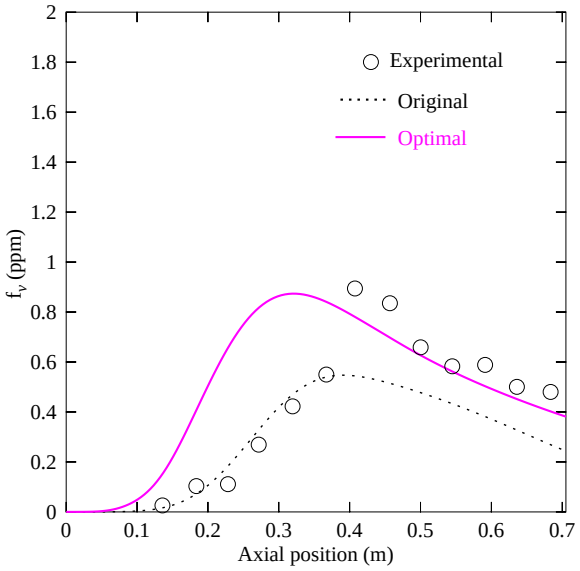

Figure 5.11: Profiles of f_v along the flame axis for Flame II [51]. The dotted line represents the original model while the thick continuous line represents the optimal model of Case I

have been published with varying fuel flow rates ($\mathrm{Re} = 4\,000 - 23\,200$) but for fixed burner diameter [53]. It is not possible to compare all published results here. We therefore retain one single flame configuration at which ethylene is fed into atmospheric air with a velocity of 48.7 m/s, leading to $\mathrm{Re} = 12\,000$.

Comparisons of axial profiles for f_v are shown in Fig. 5.16. Corroborating previous observations, the optimal set of parameters leads to a much better prediction of peak soot volume fraction compared to the original model. Again, this peak is shifted towards fuel inlet compared to the original parameter set with both results documenting a faster soot production compared to the experimental measurements.

In order to complement the qualitative comparisons introduced up to now, a quantitative measure of the differences between experimental data and simulation results would be helpful. For this purpose, three different criteria have been computed, as shown in Table 5.3. The relative norm of the difference is first computed for instance for temperature as the sum over all measurement points $\Sigma \left|T_{sim} - T_{exp}\right| / \Sigma T_{exp}$, where the index *sim* denotes simulation results and *exp* is used for experimental data. The relative difference in peak values is computed for instance for temperature as $\Delta H = \left|T_{sim,peak} - T_{exp,peak}\right| / T_{exp,peak}$.

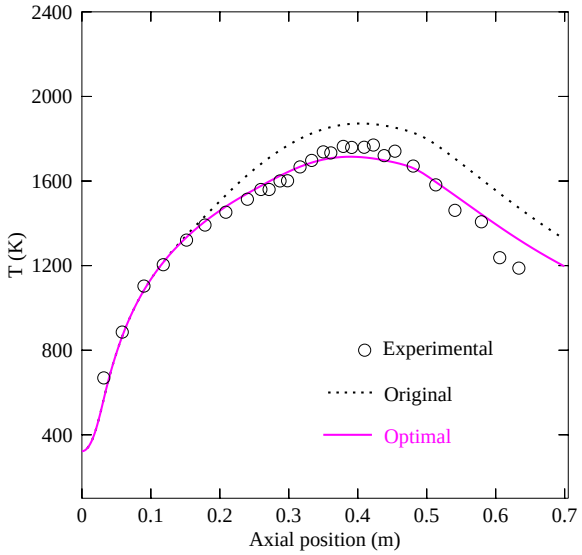

Figure 5.12: Profiles of temperature along the flame axis for Flame III [52]. The dotted line represents the original model while the thick continuous line represents the optimal model of Case I

It can be clearly observed from Table 5.3 that the optimal set of parameters leads to a systematic improvement concerning the prediction of peak temperature but also of peak soot volume fraction, the essential criterion for practical applications. Furthermore, the full profiles are also in better agreement for Flame I and Flame III concerning temperature as well as soot volume fraction. Concerning Flames II and IV, the improvement is not as clear, since temperature fields are not known and due to the observed shift towards the burner induced by the optimal set of model parameters. The shape of the profile for f_v is indeed better with the optimal set, but getting rid of the shift should be the next step towards an excellent prediction of soot particles. For this purpose, additional free parameters must be considered in the optimization process.

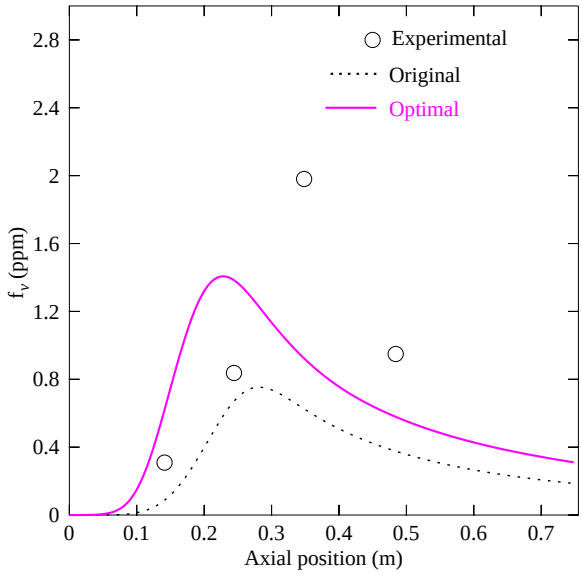

Figure 5.13: Profiles of soot volume fraction f_v along the flame axis for Flame III [52]. The dotted line represents the original model while the thick continuous line represents the optimal model of Case I

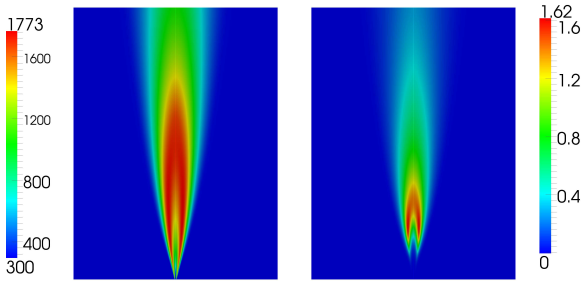

Figure 5.14: From left: Contour plots of temperature (in K) and soot volume fraction (in ppm) for flame III [52] with the optimal model

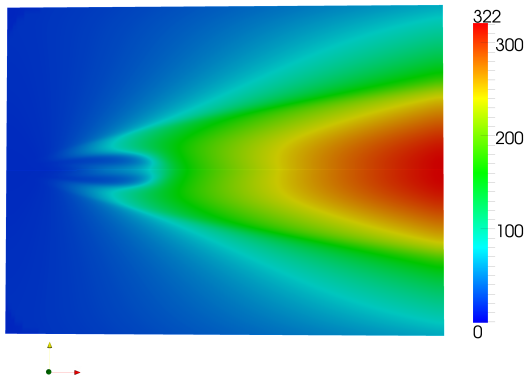

Figure 5.15: Contour plots of mean soot particle diameter (nm) for flame III [52] with the optimal model

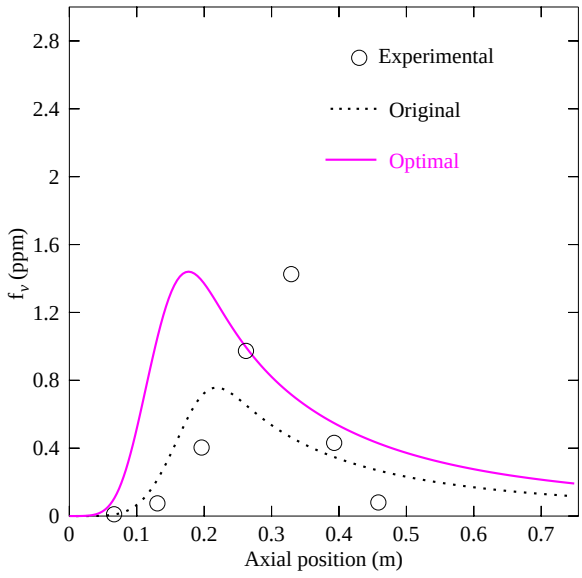

Figure 5.16: Profiles of f_v along the flame axis for Flame IV [53]. The dotted line represents the original model while the thick continuous line represents the optimal model of Case I

Table 5.3: Quantitative comparison (Optimization-Case I) of the results obtained for temperature T and soot volume fraction f_v by comparison with published experimental data. Here, Norm denotes a comparison of the full profile while ΔH is the relative difference in peak values.

Flame	Profile	Norm %		ΔH %	
		Original	Optimal	Original	Optimal
I	T	8.9	3.8	10.7	3.1
	f_v	35.3	32.4	41.9	6.1
II	f_v	32.1	43.7	38.5	2.2
III	T	8.5	2.7	5.8	3.2
	f_v	56.8	56.0	62.0	29.3
IV	f_v	58.8	95.6	47.0	1.0

5.4 Optimization-Case II

5.5 Parameters and objective functions

In the second optimization step, there were several changes and improvements compared to the earlier optimization (Optimization-Case I) in an effort to remove the undesirable profile shift towards the burner. This study is in-turn divided in to two different cases as described below (Case II-1 and Case II-2).

Case II-1: 3 objective functions ($OF1, OF2, OF3$), 3 model parameters

- $OF2$ is evaluated with respect to LE measurement only instead of average between LE and TEM (see again Fig. 5.9, on page 77).
- An additional objective function ($OF3$) has been included from the f_v exmperimental data of flame IV similarly to $OF2$.
- Combustion is represented again with equilibrium chemistry

Case II-2: 2 objective functions ($OF1, OF2$), 4 model parameters

- $OF2$ is again evaluated with respect to LE measurement points only.
- Combustion is now modeled with a more accurate laminar flamelet modeling
- An additional optimization parameter (T_g) has been added.

The objective functions are evaluated exactly in the same manner as earlier (see Chapter 4), i.e., based on the difference between the obtained simulation results and experimental measurements of temperature and soot volume fraction (from LE). After obtaining an optimal parameter set, the resulting models are further tested against the three independent experimental configurations in order to check generality.

5.5.1 Results & discussion

Some numerical details of the two optimization runs are first discussed. For Case II-1, CFD-based optimization has been carried out during 11 genera-

tions, after which no noticeable change could be observed in the objective function values, leading to an automatic interruption. As a whole, 120 sets of model parameters have been tested (i.e., 120 individual CFD simulations). In Fig. 5.17 the two objective functions ($OF1$ and $OF2$) are plotted for the best individuals. Remember that $OF1$ is the absolute error for temperature and $OF2$ the absolute error for f_v as shown in Eq. (4.1) and Eq.(4.2) respectively; both should be minimized simultaneously. As shown in Fig. 5.17, for such a concurrent multiobjective optimization, multiple equally optimal solutions (the so-called Pareto set) are frequently obtained. In such a case, improving one objective function leads to a worse result for the other one. All the points around the black line in Fig. 5.17 are hence equally optimal and constitute the Pareto set of all optimal solutions. The user must finally select one of these sets using another, independent criterion. For the present case the finally retained solution (marked with a circle in Fig. 5.17) corresponds to putting more emphasis on temperature T (experimentally known with a good accuracy) than on f_v (associated with a larger measurement uncertainty).

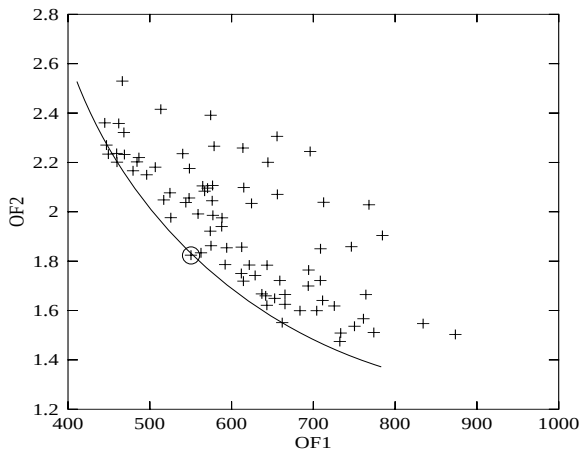

Figure 5.17: Values of objective functions $OF1$ and $OF2$ for the best individuals (i.e., model parameters) for Case II-1. The Pareto optimal solutions lie along the black curve.

Obviously, the results of the optimization depend on the selected, reference configuration (here, Flame I). It is therefore interesting to check the impact of this (arbitrary) choice. For this purpose, Figure 5.18 shows objective function values called $OF2$ and $OF3$ plotted against each other. Objective function

$OF2$ is computed as usual (Eq. 4.2 with reference to experimental results for Flame I). For comparison, $OF3$ is computed following exactly the same procedure but considering now the experimental results of Flame IV for f_v, obtained by another research group in a different setup. As can be seen in Fig. 5.18, both objective functions behave exactly in the same manner. This is a very good news, since it demonstrates that the experimental results carefully obtained by different groups fully coincide from the point of view of the optimization process. As a consequence, it should be possible to develop a general model combination, valid for a variety of configurations, by considering a single set of experimental results. Hence, Flame I is further considered as the single reference for what follows.

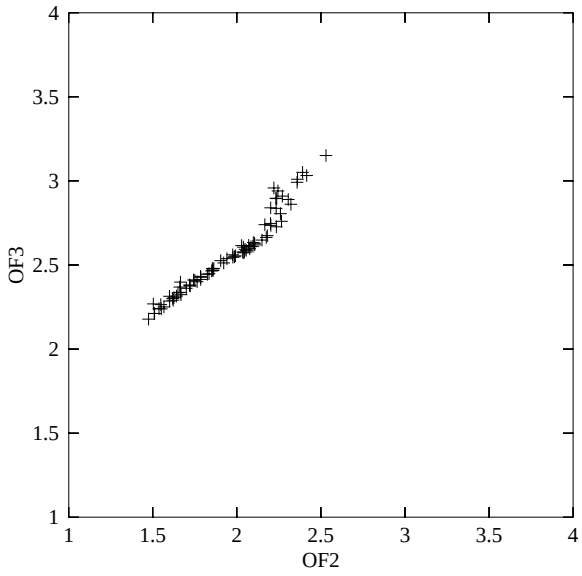

Figure 5.18: Values of objective functions $OF2$ and $OF3$ for the best individuals (i.e., model parameters) for Case II-1. These two objective functions are not concurrent and can thus be minimized simultaneously.

Concerning now the second optimization step (Case II-2), Figure 5.19 shows both objective function values. As discussed earlier, turbulence/chemistry interactions are represented in this case with a flamelet approach. An additional optimization parameter, T_g is introduced along with T_n, T_o, C_0. This last optimization step has been run for a longer time, in particular due to the fact that the parameter space is now much larger compared to optimization Case II-1. Finally, 15 generations and a total number of 160 individuals have

been evaluated by CFD. As seen in Fig. 5.19, the optimization in Case II-2 has been able to find considerably better (i.e., lower) objective functions, in particular for the soot volume fraction. Furthermore, the situation evolves from a clear Pareto set in Fig. 5.17 with concurrent objectives almost toward a single optimal solution in Fig. 5.19. This solution (marked with a circle in Fig. 5.19) is finally retained here. This behavior cannot be predicted a priori and is simply a result of the different choice of physico-chemical models.

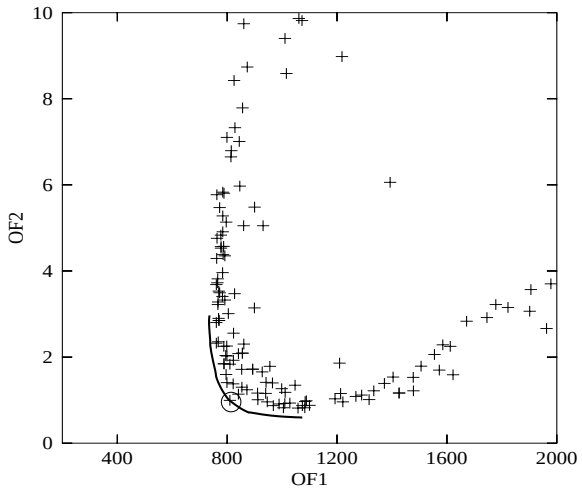

Figure 5.19: Values of objective functions $OF1$ and $OF2$ for the best individuals (i.e., model parameters) for Case II-2. 160 individuals have been evaluated as a whole. The Pareto optimal solutions lie along the black curve.

5.5.1.1 Optimal soot models for optimization Case II-1

The optimal model values obtained in Case II-1 are listed in Table 5.4 along with the relative change compared to the original model. The most obvious change is a strong increase of the radiation coefficient.

Table 5.4: Original and optimal model parameters for optimization Case II-1

Parameter	Original	Optimal	% Rel. change
T_n [K]	46 100	42 897	−6.94
T_o [K]	26 500	26 318	−0.07
C_0 [$m^{-1}K^{-1}$]	2 485	3 860	+55.33

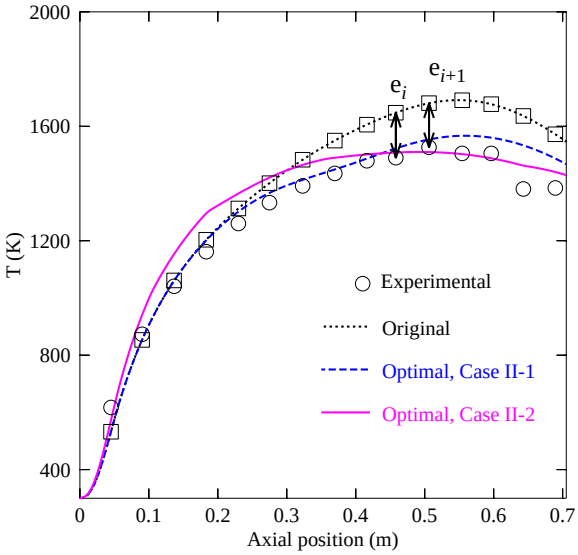

Figure 5.20: Comparison of experimental temperature along flame axis with original and optimal soot models (Case II) for Flame I. Measurements by [50].

Comparisons are shown in Figs. 5.20 and 5.21 concerning Flame I which is always used to optimize the models. With the original models, temperature of Flame I, was considerably overpredicted while at the same time f_v was severely underpredicted. The results are considerably improved for both quantities with the optimized model parameters. However, since Flame I was used for the optimization, the obtained progress is of course not a surprise. It is now necessary to check that the predictions improve also for other, independent cases. For this purpose, the flames of

Please note that the inclusion of a 3rd objective function ($OF3$) has not improved the models any further, since $OF2$ and $OF3$ describe the same physical quantity (f_v) and are corelated (see Fig. 5.18). Therefore, in Case II-2 only 2 objective functions were considered.

In Fig. 5.22 axial profiles of soot volume fraction are shown for Flame II. Experimental data (symbols) are compared with simulation results both with the original and with the optimal model parameters of Case II-1. Using the original models, the predicted peak value of f_v is nearly 40% lower than the experimental data. The predictions with the optimal models improve considerably the peak soot volume fraction, but a slight shift in peak position towards the burner is again observed, similar to that already visible in Fig. 5.9.

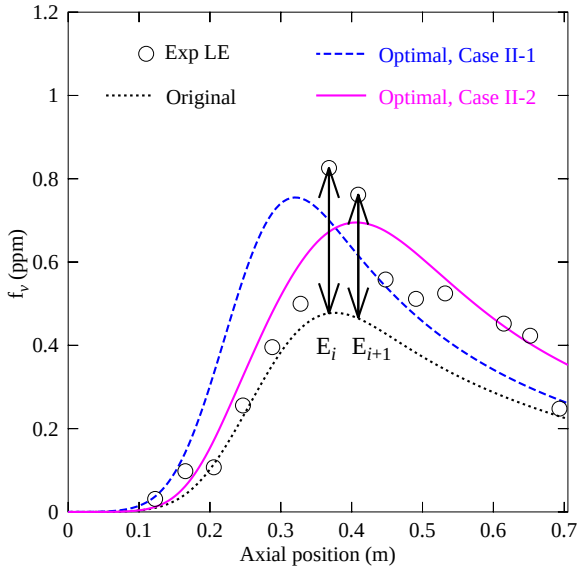

Figure 5.21: Comparison of experimental soot volume fraction f_v along flame axis with original and optimal soot models (Case II) for Flame I. Measurements by [50].

Axial profiles of soot volume fraction are shown for Flame III in Fig. 5.23. It is clear that the peak soot volume fraction is considerably better predicted with the optimal parameter sets. However, a slight shift for the profile of f_v towards the burner is again found. At the same time, the agreement concerning temperature is tremendously better with the optimal models compared to the original formulation (figure not shown).

For Flame IV one single flame configuration at which ethylene is fed into atmospheric air with a velocity of 48.7 m/s has been retained (see Table 5.1, on page 69), leading to Re = 12 000. Comparisons of axial profiles for f_v are shown in Fig. 5.24. Corroborating previous observations, the optimal set of parameters leads to a much better prediction of peak soot volume fraction compared to the original models. But again, this peak is slightly shifted towards fuel inlet compared to the original parameter set. Both original and optimal model parameters lead to a faster soot production compared to the experimental measurements.

In order to complement the purely qualitative comparisons introduced up to now, a quantitative measure of the differences between experimental data and simulation results is helpful. For this purpose, the same criteria have been

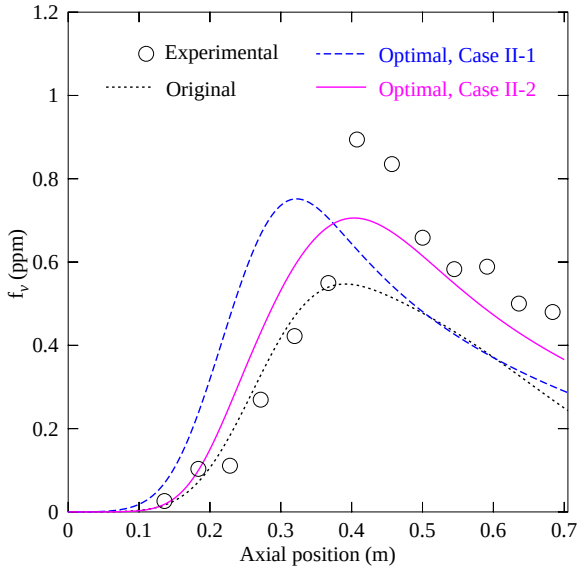

Figure 5.22: Comparison of experimental soot volume fraction f_v along flame axis with original and optimal soot models (Case II) for Flame II. Measurements by [51].

again computed and are presented in Table 5.5.

It can be clearly observed from Table 5.5 that the optimal set of parameters leads in all cases to a considerable improvement concerning not only the prediction of peak temperature but also of peak soot volume fraction, the essential criterion for practical applications. Furthermore, the full profiles are also in better agreement for Flame I and Flame III concerning temperature as well as soot volume fraction. Concerning Flames II and IV, the improvement is again not as clear, since temperature fields are not known and due to the observed, slight shift towards the burner induced by the optimal set of model parameters. The shape of the profile for f_v looks indeed considerably closer to the measurements with the optimal set, but getting rid of the shift must be the final step towards an excellent prediction of soot emissions, as discussed in the last section.

5.5.1.2 Optimal soot models for optimization Case II-2

Based on the results of the previous section, it appears that the observed shift cannot be removed completely by modifying only the particle phase models. In order to get a better prediction, it seems hence necessary to refine the

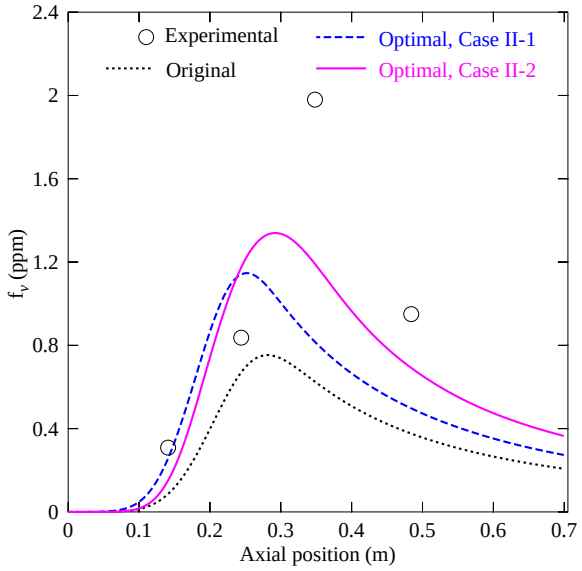

Figure 5.23: Comparison of experimental soot volume fraction f_v along flame axis with original and optimal soot models (Case II) for Flame III. Measurements by [52].

description of the physico-chemical processes in the gas phase. This is why turbulence/chemistry coupling is now realized with a flamelet model. A suitable set of model parameters can then hopefully be identified by adding the activation temperature for growth as an optimization parameter and by prescribing a very large parameter space. The model parameter values finally obtained by the optimization in Case II-2 are listed in Table 5.6 (see, page 93). Compared to the results of Table 5.4 (see, page 87), it is clear that much larger deviations have been tolerated in this final optimization step, compared to the original models of the literature. Radiation and particle growth are very strongly impacted. But, since the corresponding parameters appear in an exponential function, nucleation and even oxidation are also strongly modified. Since all models are coupled and all parameters are relevant for the objective functions, it seems logical that the optimizer will have to play on all parameters simultaneously in order to improve the predictions.

Considering first Flame I, the corresponding comparisons with the experimental data for temperature and f_v have been already shown in Figs. 5.20 and 5.21 respectively. The agreement is nearly perfect for soot volume fraction and as good as before for temperature, being in particular closer to the

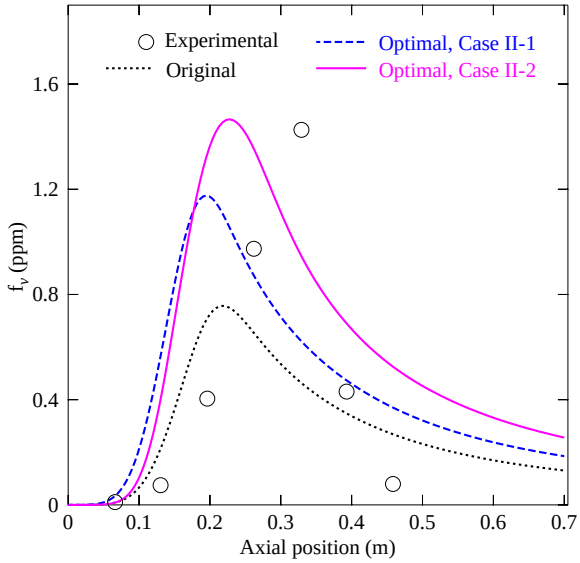

Figure 5.24: Comparison of experimental soot volume fraction f_v along flame axis with original and optimal soot models (Case II) for Flame IV. Measurements by [53].

measurements for the second half of the domain.

Figures 5.22-5.24 have shown selected results for soot volume fraction used to check the generality of the optimal models by further comparisons with Flames II, III and IV. While temperature predictions are comparable to that obtained in the first step of the optimization (Case II-1, see also Table 5.5), f_v is now much better predicted. In particular, the peak position of soot volume fraction is now almost identical with the experimental observations. The shift towards burner exit has been systematically removed or at least strongly reduced, demonstrating the importance of a better description of finite-rate chemistry interacting with turbulence.

Beyond such qualitative comparisons, a quantitative measure of the discrepancies has been shown again in Table 5.5. It can be observed from this table that the agreement concerning temperature is very high and comparable to that previously achieved in Case II-1, with slight fluctuations. The agreement concerning soot volume fraction is better throughout, even if this is not always obvious from Table 5.5. For instance, the relative norm for f_v concerning Flame IV (look back at Fig. 5.24) is higher for both optimal models compared to the original one, while a direct visual examination shows clearly

Table 5.5: Quantitative comparison (Case II-1 and II-2) of the results obtained for temperature T and soot volume fraction f_v by comparison with published experimental data. Here, Norm denotes a comparison of the full profile while ΔH is the relative difference in peak values.

Flame	Profile	Norm %			ΔH %		
		Original	Optimal Case II-1	Optimal Case II-2	Original	Optimal Case II-1	Optimal Case II-2
I	T	8.9	3.7	4.6	10.7	2.6	1.1
	f_v	35.3	32.7	17.5	41.9	8.6	15.2
II	f_v	32.1	43.8	22.8	38.5	15.9	21.1
III	T	8.5	2.9	6.2	5.8	1.8	6.8
	f_v	56.8	48.3	37.8	62.0	42.1	32.4
IV	f_v	58.8	74.3	83.1	47.0	17.5	2.8

Table 5.6: Original and optimal model parameters for optimization Case II-2

Parameter	Original	Optimal	% Rel. change
T_n [K]	46 100	51 266	11.20
T_g [K]	6 038	14 369	137.97
T_o [K]	26 500	25 872	−2.37
C_0 [$\mathrm{m^{-1}K^{-1}}$]	2 485	4 318	73.76

that the optimal models of Case II-2 indeed lead to a much closer prediction of the experiments. It is difficult to define a quantitative measure of the observed discrepancies comparable to an intuitive analysis. As a whole, it can be seen that the key quantity for all practical applications, f_v can be predicted with a high accuracy and a very good generality using the optimal models of Case II-2 (parameters of Table 5.6).

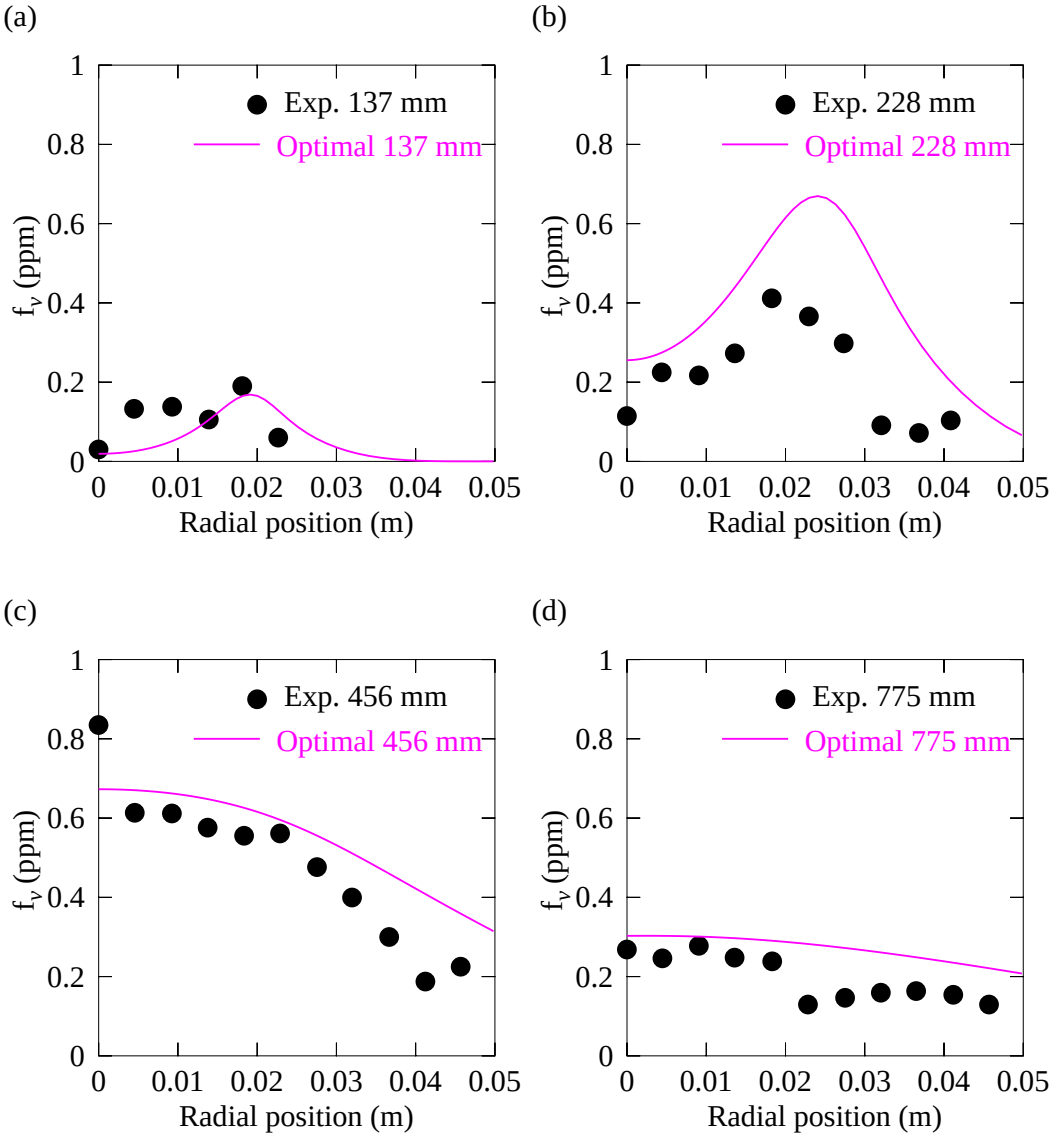

Figure 5.25: Comparison of radial profiles of soot volume fraction f_v as a function of distance from burner exit with original and optimal soot models (Case II-2) for Flame II. Measurements by [51].

Up to now, only axial profiles along the symmetry line have been considered. In a few cases, radial profiles have been also measured experimentally. Corresponding comparisons of experimental data in the radial direction with the predictions of the optimal models are presented concerning soot volume fraction f_v for Flame II at four different heights above the burner in Fig. 5.25. The symbols correspond to experimental data while the lines are simulation results. Here again, the comparisons show very good agreement for three of these four profiles, with slight discrepancies only at 228 mm above burner exit.

The developed model combination appears therefore to be valid for many different configurations.

An even better agreement with experimental measurements might however be perhaps possible by changing the radiation model, since radiative heat transfer has a major impact on flame and soot properties.

5.6 Optimization-Case III

5.6.1 Models for radiative heat transfer

Radiative heat transfer is highly significant in combustion processes involving soot. Due to the tight coupling of employed semi-empirical soot models with temperature, it is essential to take into account radiative heat transfer associated with soot particles as well as with key gaseous species while keeping acceptable numerical complexity. In the present section, three simple soot radiation models are analyzed, compared and optimized in an effort to reproduce as well as possible published experimental results while keeping intact the particulate models previously developed.

Please refer to Chapter 3 for a detailed description of the soot radiation models. C_0, C_1 and C_2 are the three proportionality constants associated with each radiation model, respectively. Therefore, the only optimization parameter is C_0, C_1 or C_2, respectively. Three independent optimizations have been carried out, one for each model. In each case the two concurrent objective functions are the absolute errors of temperature and of f_v obtained from simulation and compared to the experimental data of Flame I, as explained in Chapter 4.

For a start, Figs. 5.26 and 5.27 illustrate the impact of gas and soot radiative heat transfer on temperature and f_v in Flame I, respectively. Without any radiation, the final temperature is about 800 K too high (Fig. 5.26). Taking into account soot radiation, a much better agreement is found with the experimental measurements (shown as circles). When taking additionally into account gas-phase radiation (solid line), a further decrease of temperature by $\approx 50 - 80$ K is observed at the end of the computational domain and the

comparison improves slightly. Due to the already discussed coupling, these temperature changes have also a considerable effect on f_v (Fig. 5.27). As seen in the figures, the effect of radiation becomes significant after ≈ 200 mm from fuel inlet, i.e. where soot fraction reaches sufficiently high values, highlighting again the coupling between predictions for T and f_v.

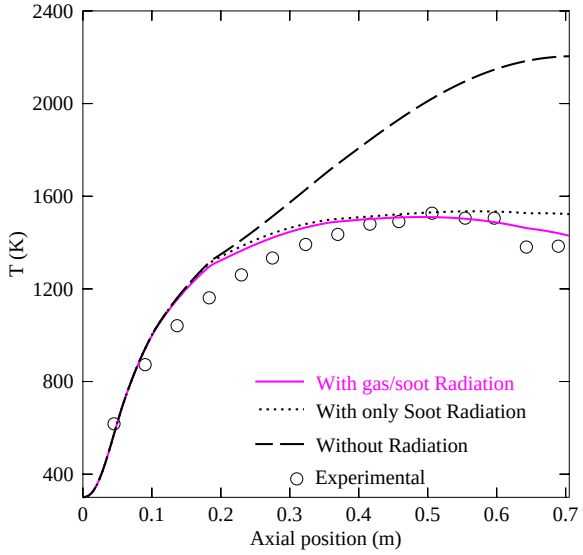

Figure 5.26: Axial profile of temperature for Flame I without any radiation model ($---$), with soot radiation only ($\cdots$), and additionally including radiation from gaseous CO_2, H_2O (solid line), compared to experiments (symbols)

It is generally accepted that radiation models based on the assumption of grey and optically thin media overpredict the radiative heat loss [34, 120] and hence underpredict flame temperatures. However, this might not be a major issue in what follows, since the proportionality constant of the models will be optimized and hence adapted by comparison to the experimental values. Therefore, the resulting global model involving both particle phase and radiation might be able to reproduce the experimental measurements with a sufficient accuracy.

5.6.2 Results & Discussion

Three separate CFD-based optimizations were finally performed using the 3 radiation models and Flame I as a reference. The obtained optimal set of parameters is then tested by further comparisons with Flames II to IV in

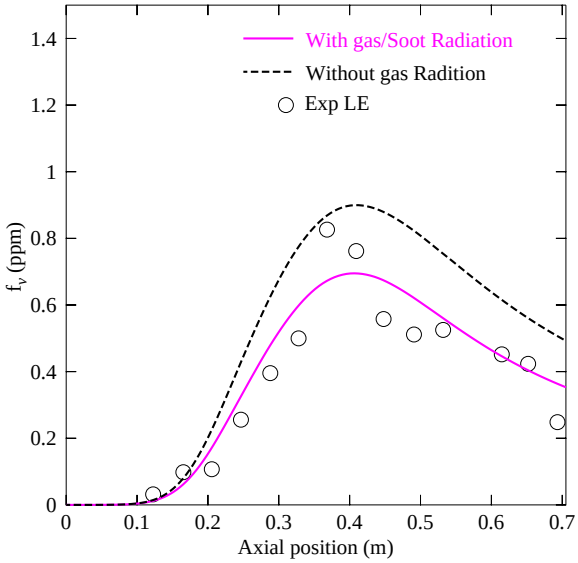

Figure 5.27: Axial profile of f_v for Flame I without and with gas radiation from CO_2 and H_2O , compared to experiments (symbols)

order to check the generality of the results.

5.6.2.1 Radiation model I (Eq. 3.29)

Since Radiation model I and the associated parameter C_0 have been already included in earlier optimization studies, we did not expect a large progress, even when concentrating now all computational resources on C_0. Indeed, the optimization is only able to improve very slightly the temperature profile, as shown in Fig. 5.28, keeping at the same time a similar agreement for f_v, as shown in Fig. 5.29, improved globally but slightly worse concerning peak value. When checking generality using Flames II to IV (not shown), the same conclusion applies; modifications are very slight and do not lead to a clear improvement compared to the experimental measurements. It is indeed possible to get a better agreement for temperature, $OF1$, by increasing the radiation parameter C_0. However, the associated impact on f_v ($OF2$) is then mostly negative. As seen in the Pareto optimal set, since the radiational proportionality constant, C_0 was already included in the earlier optimization, further optimization cannot deliver a significant improvement. The increase in parameter value decreases $OF1$ (Fig. 5.30) but the trend for $OF2$ is not uniform (Figure 5.31).

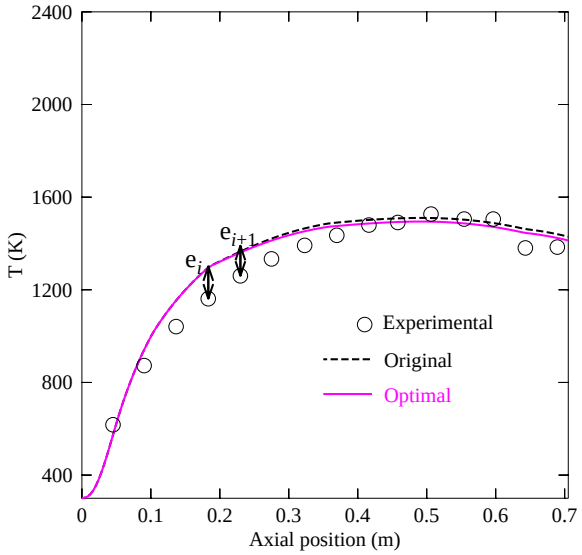

Figure 5.28: Comparison of temperature along flame axis with original model and after optimizing Radiation model I for Flame I

5.6.2.2 Radiation model II (Eq. 3.30)

The optimization results for Radiation model II are documented in Figs. 5.32 and 5.33. Here, it is possible to improve simultaneously the agreement for temperature and f_v, but the progress is very slight. This means that the originally published value for the radiation factor is directly suitable for the present application. The same behavior is observed for all other flames as well (not shown).

5.6.2.3 Radiation model III (Eq. 3.31)

At the difference of the two previous cases, the optimization relying on Radiation model III leads to considerable modifications. The original model parameter leads to a strong overprediction of f_v as exemplified in Fig. 5.34. The optimization leads to a best possible value of $C_2 = 5\,292$ m^{2}kg^{-1}. Figure 5.35 shows the resulting temperature for Flame I. Similar changes are observed for all other flames as well (not shown).

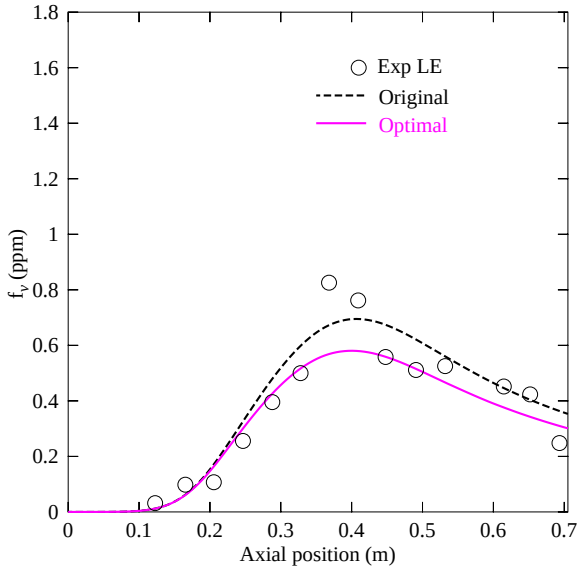

Figure 5.29: Comparison of experimental f_v with original and optimal soot model for Flame I, with soot radiative heat loss evaluated from model I

5.6.2.4 Optimal model combination

In order to complement the previous comparisons, a quantitative measure of the differences between experimental data and simulation results is again helpful. Hence, the relative norm of the difference is computed for instance for temperature as the sum over all measurement points $\Sigma\left|T_{sim}-T_{exp}\right|/\Sigma T_{exp}$, where the index *sim* denotes simulation results and *exp* is used for experimental data. Since the first radiation model has been considered extensively in previous optimization works, the corresponding results are not shown. Looking at Table 5.7 (on page 103), it is clear that the optimal versions of model II and model III are almost identical. Only very slight differences are observed.

Finally, there is unfortunately no convincing progress for all four flames when changing the soot radiation model. Therefore, the model combination proposed in previous publications and involving Radiation model I is still recommended for further studies. If, for some reason, Radiation model II or III is preferred, the corresponding set of recommended parameters is summarized in Table 5.8 (see on page 103).

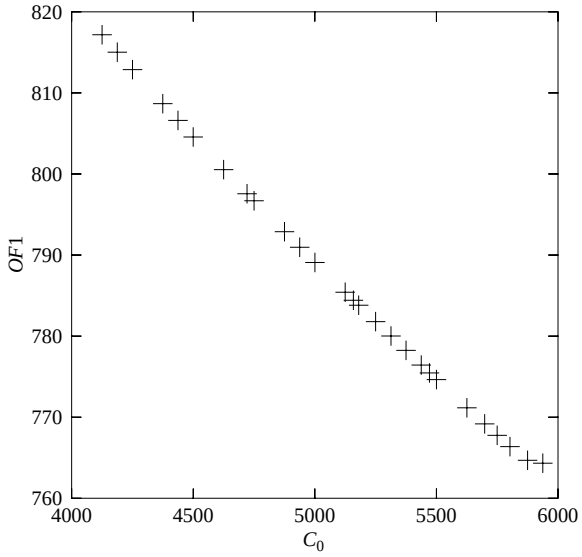

Figure 5.30: Effect of radiation proportinality constant C_0 on $OF1$ in the given range

5.7 Summary

Numerical optimization has been carried out in three steps starting from existing soot models in an effort to improve them. These optimization cases differ in the number of parameters, objective functions and also in the representation of the gas-phase chemistry. Flame I experimental data has been considered to calculate the objective functions. Once the optimal models are found, they are further validated by comparison with three other flames. The finally derived optimal combination obtained in optimization Case II-2 with radiation model I is able to predict all temperature and soot volume fraction profiles accurately and is recommended for all further studies. Changing the radiation model does not lead to a noticeable improvement and is therefore not recommended.

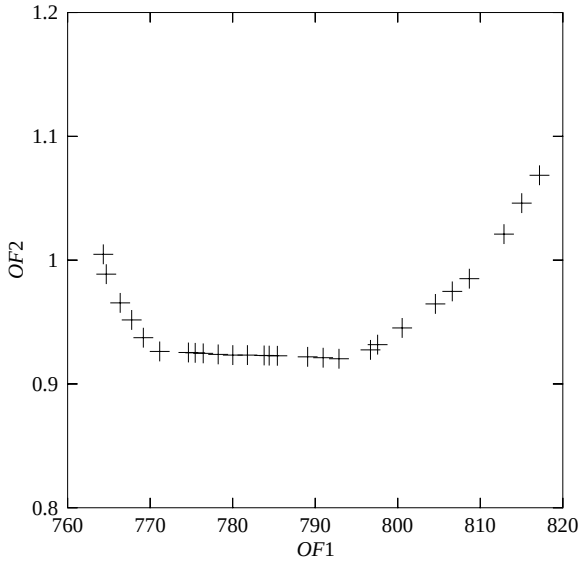

Figure 5.31: Values of objective functions $OF1$ and $OF2$ for the best individuals (i.e., model parameters)

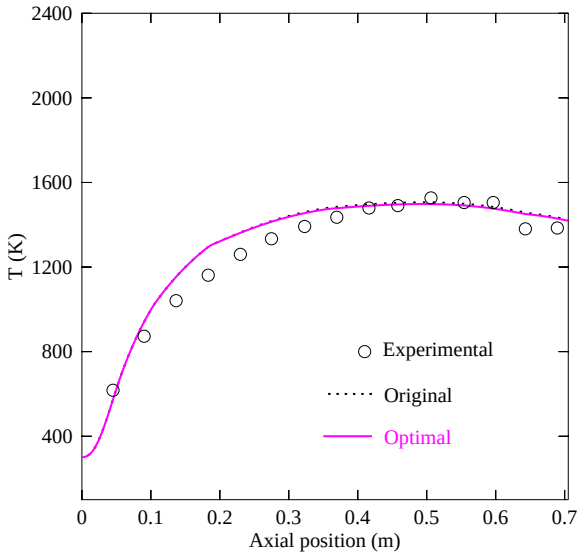

Figure 5.32: Comparison of experimental temperature with original and optimal soot model for Flame I, with soot radiative heat loss evaluated from model II

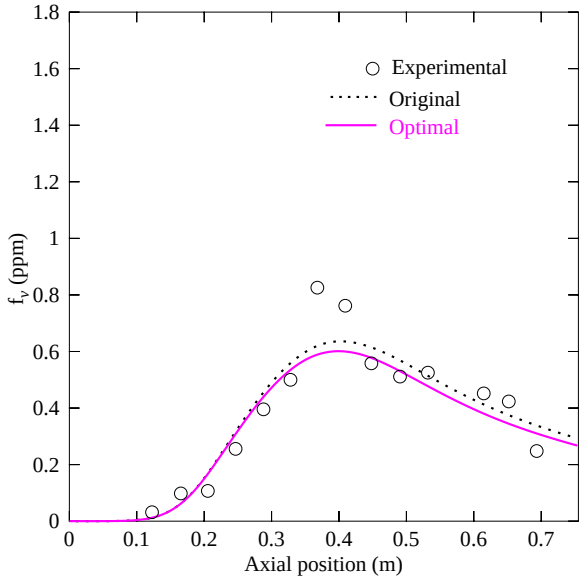

Figure 5.33: Comparison of experimental f_v with original and optimal soot model for Flame I, with soot radiative heat loss evaluated from model II

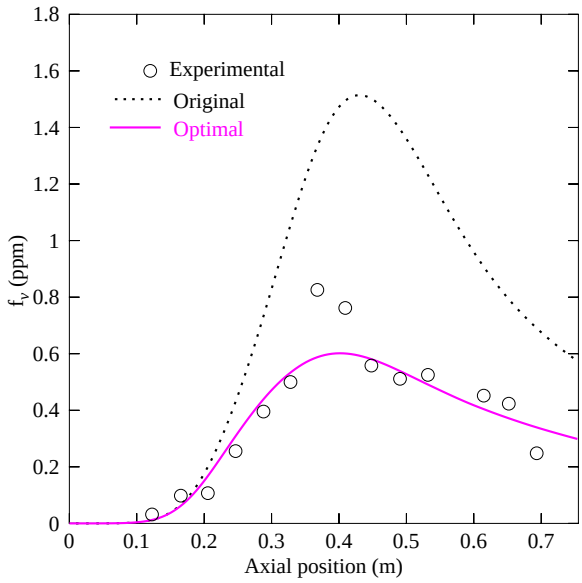

Figure 5.34: Comparison of experimental f_v with original and optimal soot model for Flame I, with soot radiative heat loss evaluated from model III

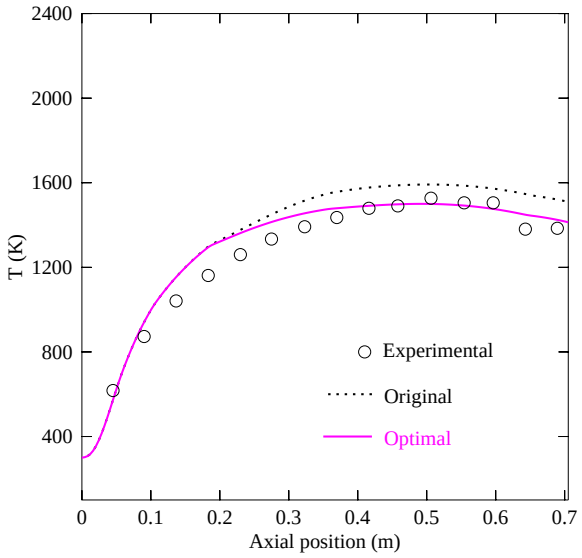

Figure 5.35: Comparison of experimental temperature with original and optimal soot model for Flame I, with soot radiative heat loss evaluated from model III

Table 5.7: Quantitative comparison of the results obtained for T and f_v with experimental data.

Case	Var.	Norm %			
		Rad. model II		Rad. model III	
		Original	Optimal	Original	Optimal
I	T	4.5	4.4	8.0	4.3
	f_v	16.4	16.6	109.8	16.1
II	f_v	25.8	27.4	107.7	27.5
III	T	6.3	6.4	5.8	6.4
	f_v	40.0	41.4	70.8	41.3
IV	f_v	76.1	71.4	222	71.6

Parameter	Optimal Value
T_n [K]	51 266
T_g [K]	14 369
T_o [K]	25 872
C_0 [m^{-1} K^{-1}]	4 318
C_1 [W m^{-3} K^{-5}]	$2.77\,10^{-4}$
C_2 [m^2 kg^{-1}]	5 292

Table 5.8: Optimal parameters

Chapter 6

Modeling TiO_2 nanoparticle formation in CH_4-O_2 diffusion flames

6.1 Introduction

The present chapter aims at modeling as accurately as possible TiO_2 nanoparticle formation in turbulent flames. Due to the vast applications of TiO_2 particles (pigments, cosmetics, photocatalysis) understanding its formation and evolution is very important. Two different precursors are typically used in the production of TiO_2 nanoparticles, titanium tetra-isopropoxide (TTIP) and titanium tetra-chloride ($TiCl_4$). We decided to concentrate here on TTIP. Detailed analysis of literature shows that the chemistry behind formation of nanoparticle nuclei from precursor solution and subsequent growth process are not satisfactorily well-known or understood yet. Physico-chemical models describing the formation of TiO_2 nanoparticles are very limited in the literature. Therefore, developing prediction models is very challenging, but relevant for many applications.

6.2 Configuration

The typical configuration employed for all simulations involves a CH_4-O_2 diffusion flame with TTIP as precursor and Ar as carrier gas. Figure 6.1 shows

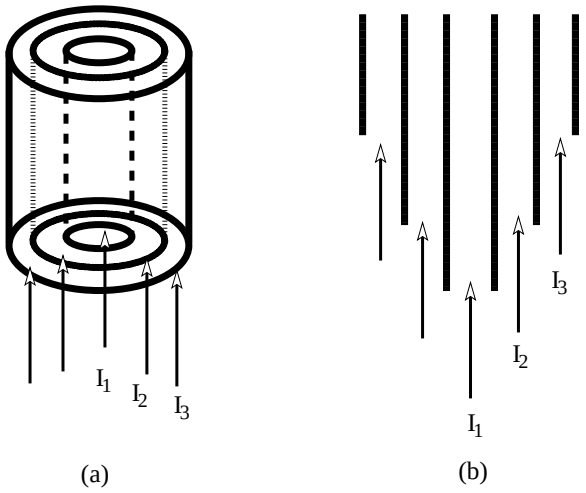

Figure 6.1: Configuration of the burner employed for all numerical simulations [1]

such a diffusion flame burner, involving three concentric circular tubes, as employed in [1, 59]. The inner diameters of the tubes are first $D_{1i} = 1.8$ mm, $D_{2i} = 3.5$ mm and $D_{3i} = 4.8$ mm, respectively. The tube wall thickness is kept constant at 0.3 mm. I_1, I_2 and I_3 denote the three inlets through which Ar, CH_4 and O_2 are injected respectively in the initial configuration. The combustion takes always place at atmospheric pressure. The TTIP precursor is mixed with Ar and then injected into the flame zone where it decomposes to generate subsequently TiO_2 nanoparticles. The flow rates of Ar ($\dot{Q}_a$), CH_4 ($\dot{Q}_m$) and TTIP ($\dot{m}_{ttip}$) are fixed during all the study at 0.75 L/min, 0.5 L/min and 6.5 g/h respectively. The temperature of all the gases at injection and all burner walls (included in the simulation) are kept constant at 450 K. All these values are in accordance with the experimental data discussed in [1].

6.3 Computational details

An axisymmetric flame configuration has been considered, as highlighted with dash-dotted lines in Fig. 6.2. After checking the possible influence of the numerical boundary conditions on the process results, a large computational domain of fixed size (800 mm streamwise length × 300 mm radius) has been retained. The generation of a structured grid has always been done using *Gambit* and involves about 25 000 nodes. A grid independence study shows

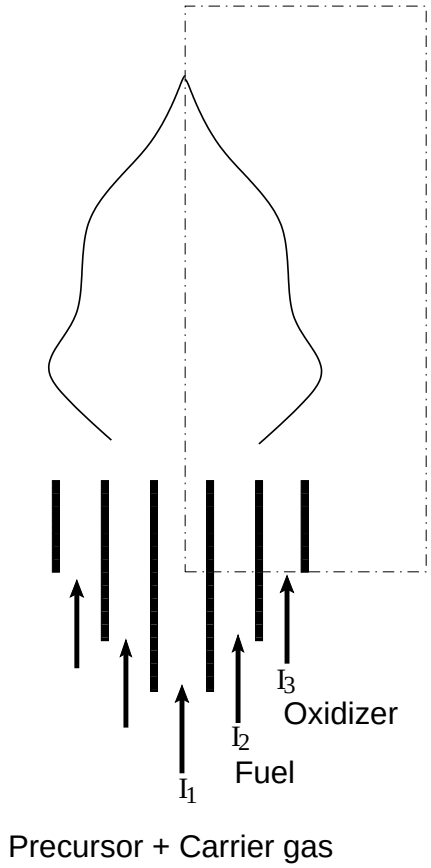

Figure 6.2: Typical configuration and employed computational domain (axisymmetric), shown with dashed-dotted lines

that dividing further each cell into four subcells leads to negligible changes in peak temperature and mean particle size, below 1%.

The investigations involve two steps. First, the simulations are performed with the exact process and burner configuration described in [1, 59]. Here, three different oxygen flow rates $\dot{Q}_o$ of 2, 4 and 6 L/min (referred as Case I to Case III) are considered. Once all employed physicochemical models and numerical techniques have been validated in this manner using published results from the literature, they are kept intact for the further parametric analysis.

In the second step the flow configuration and the burner diameters are varied while keeping unchanged all the mass flow rates (of Ar, CH_4, TTIP and O_2). The inlets of Ar, CH_4 and O_2 are first interchanged to find out the best configuration. It is finally observed that the originally retained experimental configuration delivers indeed the best results and it is retained for the most important set of simulations, i.e., for burner geometry variation. In this

third and last part, the internal diameters of the 3 burners (D_{1i}, D_{2i}, D_{3i}) are systematically varied (increased or decreased) by ± 10% or ± 20%. Considering construction constraints, this finally delivers twelve different burner geometries.

Then, the properties of the obtained flames are investigated. Out of the twelve configurations, the six cases leading to stable combustion are gathered in Table 6.1 along with the corresponding burner dimensions. Please note that in this table a superscript of 10 or 20 indicates an increase in inner diameter by 10 or 20%, while a subscript of 10 or 20 indicates a decrease in inner diameter by 10 or 20%. Hereafter these cases are systematically referred to as Case 1 to Case 6. Once the resulting flame fields have been determined, the computation of the PSD can be started, as described later. For one configuration, the typical computational time using 8 computing cores of a Linux-based PC cluster in parallel is approximately 16 hours.

Table 6.1: Configurations finally considered during the numerical simulation since they can be constructed and lead to stable combustion (Note: superscript 10 and subscript 10 indicates (+) and (-) 10% change from the initial inner diameters listed in the first line; similarly for 20). The corresponding injection velocities (in m/s) are given in the last three columns

Case	Description	D_{1i}	D_{2i}	D_{3i}	v_{1i} (Ar)	v_{2i} (CH_4)	v_{3i} (O_2)
Initial	$D_{1i}D_{2i}D_{3i}$	1.80	3.50	4.80	4.91	1.63	6.81
Case 1	$D_{1i^{10}}D_{2i^{10}}D_{3i^{10}}$	1.98	3.85	5.28	4.06	1.29	5.25
Case 2	$D_{1i^{10}}D_{2i_{10}}D_{3i^{10}}$	1.98	3.15	5.28	4.06	3.25	3.07
Case 3	$D_{1i_{10}}D_{2i^{10}}D_{3i^{10}}$	1.62	3.85	5.28	6.06	1.07	5.25
Case 4	$D_{1i_{20}}D_{2i^{20}}D_{3i^{20}}$	1.44	4.20	5.76	7.67	0.78	4.18
Case 5	$D_{1i_{20}}D_{2i_{20}}D_{3i^{20}}$	1.44	2.80	5.76	7.67	2.88	1.96
Case 6	$D_{1i_{20}}D_{2i_{20}}D_{3i_{20}}$	1.44	2.80	3.84	7.67	2.88	13.31

6.4 Employed models

The industrial CFD solver *Ansys-Fluent* has been again used to solve the gas-phase governing equations, considering a detailed CH_4-O_2 combustion mechanism with 17 species and 41 reactions. The turbulence is still modeled with the standard $k-\epsilon$ model. The Eddy Dissipation Concept (EDC) model is used to handle the turbulence-chemistry interactions, which is different from our ear-

lier modeling apporach for soot. In *Ansys-Fluent* the equilibrium and laminar flamelet models can only be used with a single fuel and oxidizer inlet [124]. Therefore, EDC combustion model is employed here even though it demands a higher computational time. Particle phase PBE has been solved using QMOM accounting for particle nucleation, growth and aggregation. Please see Chapter 3 for details concerning the employed models and Chapter 2 for details concerning PBE and QMOM.

The EDC model involves two key parameters, volume fraction constant (C_γ) and time scale constant (C_τ). Using the standard values of these model parameters, a considerable over prediction of the temperature field was obtained for the initial configuration. In several published studies those model parameters had also to be modified in order to obtain agreement with experimental data, see for instance [123]. Therefore, a parameter analysis has been first carried out to find optimal values for the present problem. The best agreement with experimental data has been finally obtained for $C_\gamma = 2.1377$ and $C_\tau = 3.4$, as discussed later, and these values have been afterwards kept constant during all the study.

6.5 Results & Discussion

As explained previously, the first simulations are carried out for 3 different O_2 flow rates, $\dot{Q}_o$ at 2, 4 and 6 L/min (denoted as Case I to Case III), reproducing directly the experimental conditions of Wegner and Pratsinis [1] outlined in Section 6.2.

These first simulations have been carried out using the default EDC parameters ($C_\tau = 0.4083$ and $C_\gamma = 2.1377$). When comparing with the published experimental measurements, showing a peak temperature always below 2300 K (before injecting TTIP), the CFD results lead to a large over prediction of the temperature fields, since a peak value of roughly 2700 K is obtained. Furthermore, the temperature peaks are found very far away from the injection, in complete disagreement with the experimental data. In order to find an explanation for this unacceptable discrepancy, the over prediction of temperature has been thoroughly analyzed. First, the influence of the reaction

mechanism (number of chemical species, number of reactions, parameters) has been systematically checked. Increasing the complexity of the chemical scheme indeed leads to a slight decrease in temperature. The most complex formulation tested (37 species, 166 reactions) still delivers a peak temperature of 2620 K. This is only a small progress, in particular when compared to the rapidly increasing computational cost. Hence, using a more complex chemical scheme does not appear to be a solution. As an alternative explanation, the impact of the EDC model parameter C_τ has been analyzed, since it is the most significant parameter of the model.

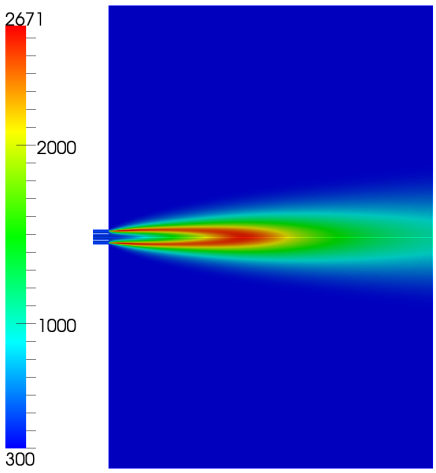

Figure 6.3: Contours of temperature field evaluated with default EDC parameters in *Ansys-Fluent*

6.5.1 Effect of reaction mechanism

In order to understand the effect of reaction mechanisms on final temperature, we have considered different chemical schemes. The four different mechanisms with the involved number of species and reactions, along with the obtained peak temperatures for two different O_2 oxygen flowrates (Case I, Case II) are shown in Table 6.2. Gas phase radiation has not been considered here. TTIP is not injected into the flame yet. Hence, the heat of reaction is also not included in the calculations. As the number of species and reactions increases the peak temperature decreases, but not drastically. The decrease in peak temperature

from mechanism 1 to 4 is approximately 50 K for Case I and 100 K for Case II. Considering the drastic increase in computational time with the increase in the number of species, mechanism 1 has been retained for all further calculations.

Mechanism	# Species	# Reactions	Peak temperature in K (O_2, 2L/min)	Peak temperature in K (O_2, 4L/min)
1	17	41	2670	2887
2	18	58	2640	2805
3	21	84	2630	2800
4	37	166	2620	2770

Table 6.2: Influence of reaction mechanisms on peak temperature for Case I and Case II

6.5.2 Effect of EDC model parameter (C_τ)

Axial profiles of temperature for various values of C_τ are shown in Fig. 6.4. For the flame configuration considered, it is obvious that C_τ has a strong impact on the temperature field, as expected from the literature. Increasing the value of C_τ from its default value (0.4083) to 3.4, the peak temperature rapidly decreases and is switched towards the burner. Both evolutions coincide well with the published experimental data for this configuration. For a value of $C_\tau = 3.4$ (keeping the default value of C_γ) the obtained temperature field finally reproduces in an acceptable manner all available experimental measurements. Hence, for all later simulations, the EDC model parameters have been fixed at $C_\tau = 3.4$ and $C_\gamma = 2.1377$. Note that modifications of the EDC model parameters are often needed, as discussed recently in [123].

6.5.3 Results with TiO_2 nanoparticles

In this section the numerical results concerning gas and particle phase fields are analysed during the decomposition of TTIP to form TiO_2 nanoparticles. Radiation occuring from key gaseous species (CO_2, H_2O, CO and CH_4) has been considered. As the TTIP decomposition reaction is endothermic in nature, the heat of reaction is also included in the calculations. Both these terms are added into energy balance equation of *Ansys-Fluent* as negative source terms. Please note that in all cases the particle phase properties are obtained

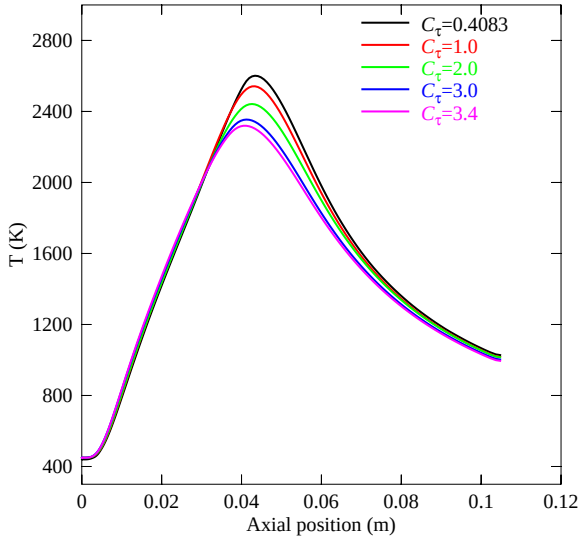

Figure 6.4: Axial profiles of temperature (in K) for various values of C_τ with reaction mechanism 1.

through Quadrature Method of Moments (QMOM) with 2 quadrature nodes. DQMOM was not retained here due to stability issues.

Figure 6.5 now shows the obtained profiles of temperature (a)-(c), TTIP concentration (d)-(f) and TiO_2 concentration (g)-(i) for Case I, Case II and Case III respectively. Due to lower O_2 flow rate in Case I the mixing of fuel/oxidizer is poor. As a result the temperature fields and consequently the overall decomposition rate of TTIP extend far from the burner (see Figs.(a) and (d)). Whereas, the decomposition is faster and closer to the burner in Case III as temperature is higher near the burner (see Figs.(c) and (f)). The same behavior is observed for TiO_2. Figures 6.5 (g), (h) and (i) show the contour plots of overall titania molar concentrations for the 3 different oxygen flow rates. As the oxygen flow rates increase, the decomposition of TTIP shifts towards the burner, subsequently TiO_2 production also shifts towards the burner. Please note that the particle phase PBE solver (QMOM) is not activated yet. For Case I (Fig. 6.5 (g)) and Case II (Fig. 6.5 (h)) the overall TiO_2 formation is higher than that of Case III (Fig. 6.5 (i)). Once the TiO_2 molar concentration is known, corresponding nucleation and surface growth terms can be evaluated from Eq. (3.25) and Eq. (3.26), respectively. In the case of nucleation a uniform distribution of particles in the particle volume range $0 \leq \xi \leq \varepsilon$ (ξ being the internal co-ordinate, in this case particle volume)

has been considered. For the present case, ε is assumed to be 1 nm^3, a little higher than the volume of a TiO_2 monomer ($\approx$ 0.0332 nm^3). Nucleation forms a uniform distribution of particles in the particle volume range $[0, 1]$ nm^3 (please see Chapter 2 for a detailed description).

Figure 6.6 shows the corresponding comparison of axial profiles of temperature with experimental data for two different O_2 flow rates (Case II and Case III), since no experimental data is available for Case I. Please note that, the gas radiation from the key species and the heat of reaction for TTIP decomposition have been included in the simulations. As the flow rate of O_2 increases, the peak temperatures are reduced and shifted towards the burner, due to a faster mixing induced by higher turbulence levels. The temperature profiles predicted by simulation are slightly lower and shifted away from the burner when compared to the experimental data. However, the comparison is quite fair and the changes between Case II and Case III are very well reproduced by CFD.

6.6 Parametric study

Obtaining as far as possible a monodisperse distribution of nanoparticles with a low diameter and in a large quantity would be very desirable for practical applications. Hence, the influence of different parameters is now considered in order to achieve the best possible conditions: minimize d_{mean}, maximize f_v, and minimize σ_g (the width of the distribution), if possible simultaneously.

6.6.1 Exchanging injections for a fixed geometry

In a first step, we have tried interchanging systematically the gas injections (Ar, CH_4 and O_2) within the three available tubes (Inlet I_1, I_2, I_3, shown in Table 6.3), all other parameters between fixed. After computing all configurations, it appeared that the initial configuration (inlet I_1: Ar, Inlet I_2: CH_4, Inlet I_3: O_2) is the only one leading to a stable flame. In all other cases, it was either impossible to start the combustion or to stabilize the flame.

Config.No.	Inlet-I_1	Inlet-I_2	Inlet-I_3
1	CH_4	O_2	Ar
2	CH_4	Ar	O_2
3	O_2	CH_4	Ar
4	O_2	Ar	CH_4
5	Ar	CH_4	O_2
6	Ar	O_2	CH_4

Table 6.3: Different configurations considered in the numerical simulation to study the impact on the PSD

6.6.2 Effect of change in burner diameter

Keeping now these injections and all mass flow rates constant, the burner geometry has been systematically varied by increasing or decreasing the inner diameters by 10 or 20%. The results for Case 1 to Case 6 (already presented in Table 6.1, on page 107) are now analyzed in detail.

Figure 6.7 shows all corresponding temperature profiles along the burner axis. The simulation data for the initial configuration is shown with a solid curve, while different symbols are used for Case 1 to Case 6. As seen in the figure, even with fixed mass flow rates and injections, considerable differences are observed in the obtained temperature fields, both in terms of peak value and of spatial distribution. The peak values range from $\approx$ 1900 K for Case 6 to $\approx$ 2300 K for Case 5. These differences are best seen in the inset plot in the top-right corner. The slopes and width of the high temperature regions differ as well. For instance, Case 6 shows only a short span with high temperatures compared to Case 5. When compared to the initial configuration (solid curve) the obtained differences are as expected more significant for Cases 4, 5 and 6 (variations of internal diameters by $\pm$ 20%), while differences are less pronounced for Cases 1, 2 and 3 (variations of diameters by only $\pm$ 10%). Since it is known from the literature that process temperature is the most significant parameter to control particle properties, large variations are now expected concerning the PSD of produced TiO_2 particles.

Axial profiles of TiO_2 molar concentration in gas phase are depicted in Fig. 6.8. The injection velocities are highest for Case 6, hence the temperatures and correspondingly TTIP decomposition and TiO_2 conversion are higher close

to the burner. In contrast, for Case 2, the injection velocities are very low, inducing low turbulence (see Table 6.1 for the injection velocities). Therefore, the peak value is shifted away from the burner.

Figure 6.9 shows the obtained profiles of volume fraction f_v along the central axis of the burner. The peak volume fraction is maximum for Case 1, slightly higher than for the initial configuration, and minimum for Case 5. In spite of its lowest peak temperature, Case 6 also leads to a high peak in volume fraction ($\approx$ 6.5 ppm), illustrating the complexity of the coupled physicochemical processes controlling particle formation. As already discussed for flame temperature, an increase in injection velocities (decrease in injection slot diameter) leads to a shift of all quantities (temperature, TTIP, TiO_2) towards the burner (compare Case 6, where all profiles reach peak values close to the burner, to Case 2 for which the evolutions are delayed). To summarize concerning TiO_2 molar concentration and peak volume fraction, the highest values are observed for Case 1, initial configuration, and Case 6, in decreasing order.

One major particle quantity of interest is the mean diameter, d_{mean} of the TiO_2 nanoparticles. Figure 6.10 shows d_{mean} along the burner central axis for all cases. At first, d_{mean} increases rapidly close to the burner, it then decreases before increasing again gradually until the end of the computational domain. This complex evolution is a consequence of the competition between nucleation, growth and aggregation. When looking in details at the source terms of the moment transport equations and at the corresponding rate equations (k_g, k_s and β), two separate regions (one directly behind the burner, one considerably further downstream) are found with intense nucleation. After the first nucleation burst, the nanoparticle diameter increases rapidly due to aggregation. After reaching its peak mean diameter, the impact of aggregation decreases and molecular growth dominates, until reaching the second region of nucleation. Later, the mean particle size increases gradually till the end of the computational domain due to aggregation. As a whole, it is observed that the largest particles are produced for Case 2, where the injection velocities are smaller leading to slow evolutions. The smallest mean diameter d_{mean} is obtained for Case 6 where the injection velocities are large, leading to very

fast evolutions directly after injection. The initial configuration is once again second best, this time after Case 6, concerning d_{mean}.

The standard deviation (σ_g) quantifying the width of the PSD is shown in Fig. 6.11. It is seen in this picture that all cases produce the same qualitative trend. σ_g increases rapidly up to about 2.3 close to the inlet, then drops rapidly to ≈ 1.3. This indicates again that, as soon as the particles are formed, they rapidly grow due to aggregation, broadening the PSD ($\sigma_g \rightarrow 2.3$). Following this phase, with mostly nucleation and very little effect from molecular growth and aggregation, a value of σ_g close to 1.3 is obtained, indicating a nearly monodisperse distribution in this region. Later on, σ_g gradually increases again, goes through a smaller secondary peak, then slowly decreases before reaching finally a nearly constant value in the range $\approx 1.5 - 1.7$. Considering that σ_g should be minimized, the initial configuration and Case 1 are now the worst cases, while Case 3 and Case 4 deliver optimal conditions.

The peak values of temperature, of d_{mean}, of f_v and the value of σ_g at the outlet are presented for all Cases in Table 6.4. Remembering that the objective was to minimize d_{mean}, maximize f_v and minimize σ_g, the best three cases are associated in this Table respectively with $+++$ (best), $++$ (second best) and $+$ (third best). Similarly, the three worst cases are associated with $---/--/-$. Case 6 shows the lowest peak temperature and leads to nanoparticles with the lowest mean diameter d_{mean} (46.6 nm), together with a high volume fraction ($f_v \approx 6.4$ ppm). When compared to the initial burner configuration the geometric standard deviation at the outlet is also less (1.61) for Case 6, compared to 1.66 for the initial configuration. Case 1 leads to the highest volume fraction ($f_v \approx 6.4$ ppm), which is positive, but unfortunately also to the largest standard deviation.

Looking again at Table 6.4, it is difficult to identify a clear winner for all three objectives. Indeed, the analysis confirms the quality of the original experimental work, since the initial configuration belongs to the very best in terms of volume fraction and particle diameter. However, it is the worst one concerning the width of the PSD. This negative correlation appears to be a general rule. Hence, future analysis will have to consider a concurrent optimization process, since the objectives cannot be fulfilled simultaneously.

Table 6.4: Peak values of temperature, of d_{mean}, of f_v, and of σ_g at outlet

Case	Temperature (K)	d_{mean} (nm)	f_v (ppm)	σ_g (at outlet)
Initial	1991	52.9 (++)	6.7 (++)	1.66 (−−−)
Case 1	2008	56.4 (+)	6.8 (+++)	1.66 (−−)
Case 2	2065	64.4 (−−)	5.7 (−)	1.59
Case 3	2108	64.4 (−−)	5.8	1.51 (+++)
Case 4	2224	62.7 (−)	5.3 (−−)	1.52 (++)
Case 5	2319	61.1	5.1 (−−−)	1.57 (+)
Case 6	1893	46.6 (+++)	6.4 (+)	1.61 (−)

The presented analysis already shows that it should be possible to obtain a larger amount of particles (Case 6), a smaller diameter (Case 1), or a more peaky PSD (any case, in particular Case 3), if needed for a particular process. As a whole, Case 6 and Case 1 appear as promising alternatives to the initial configuration.

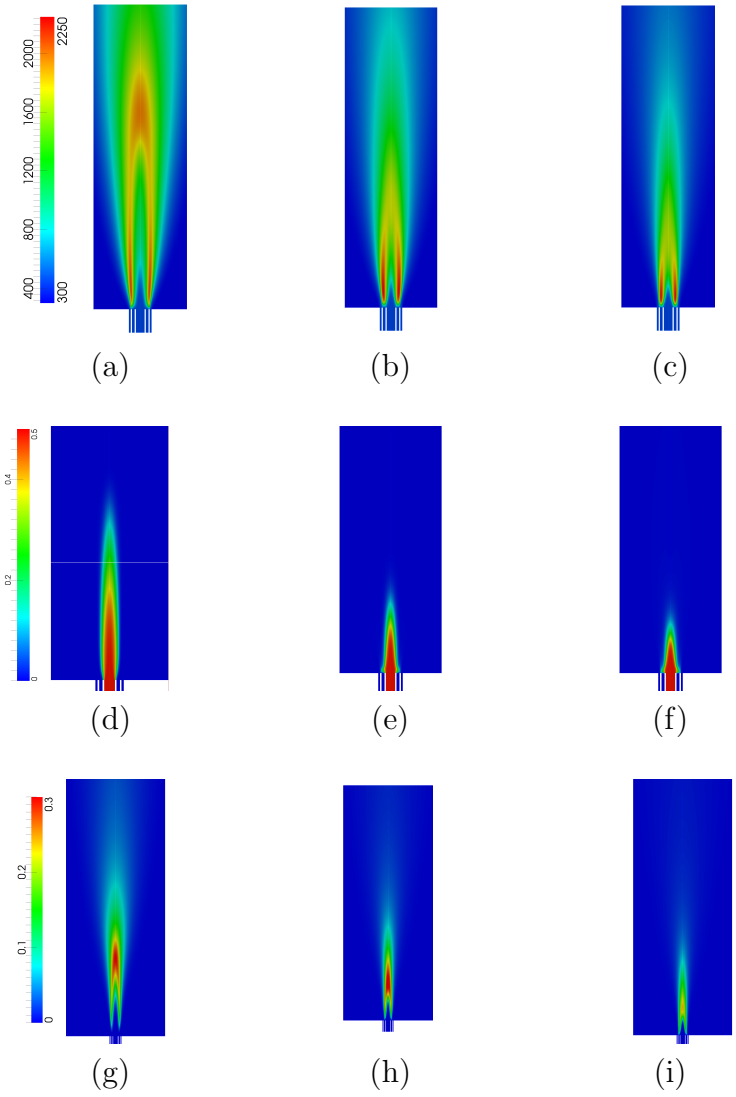

Figure 6.5: Contour plots of temperature (a, b, c) in K, TTIP (d, e, f) and TiO_2 (g, h, i) concentrations in mol/m^3 for Case I, Case II and Case III (from left to right). The same color scale is employed for all three Cases.

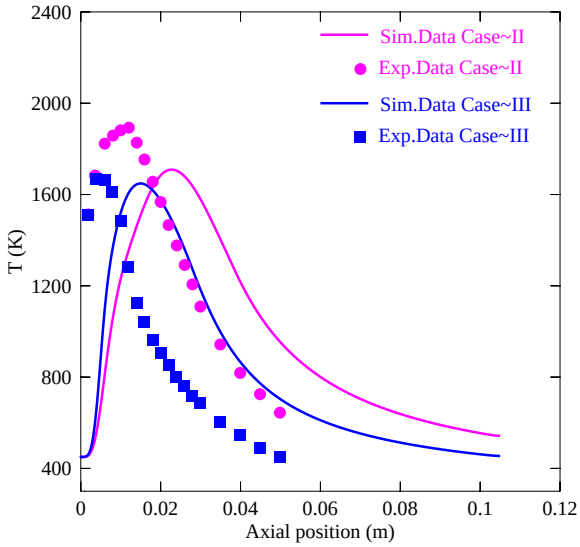

Figure 6.6: Axial profiles of temperature for 2 different oxygen flow rates (Case II and Case III). Continuous lines are simulation data, symbols are experimental data.

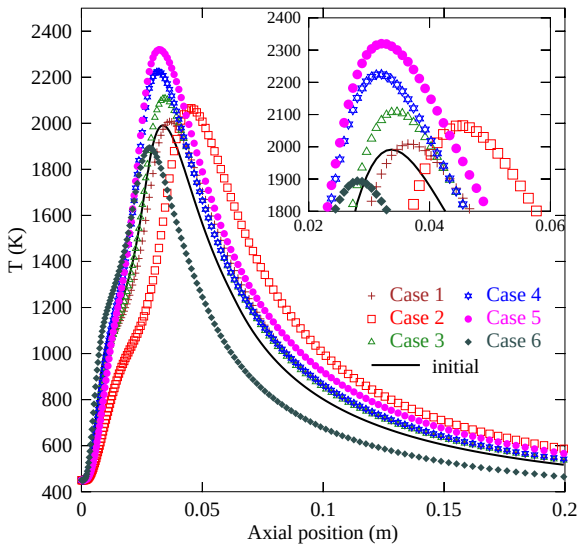

Figure 6.7: Comparison of the temperature profiles along the burner axis close to the injection for all cases considered. The black solid curve corresponds to the initial configuration. The inset plot in the top-right corner is a zoom on the peak temperature region.

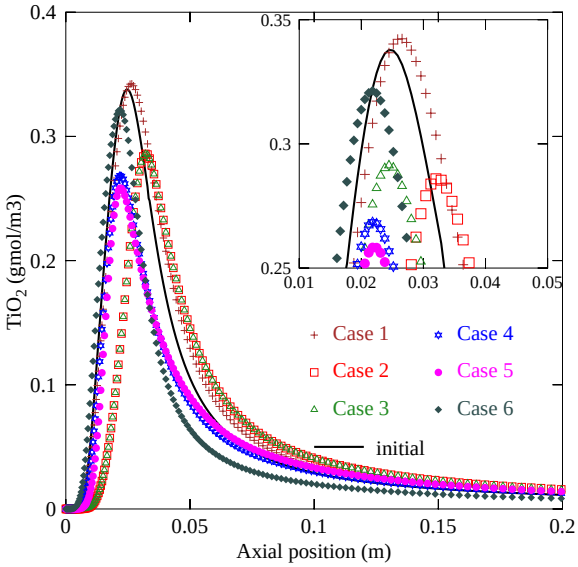

Figure 6.8: Comparison of the profiles of TiO_2 concentration (in gmol/m^3) along the flame axis for all the cases considered. Black solid curve is with original configuration.

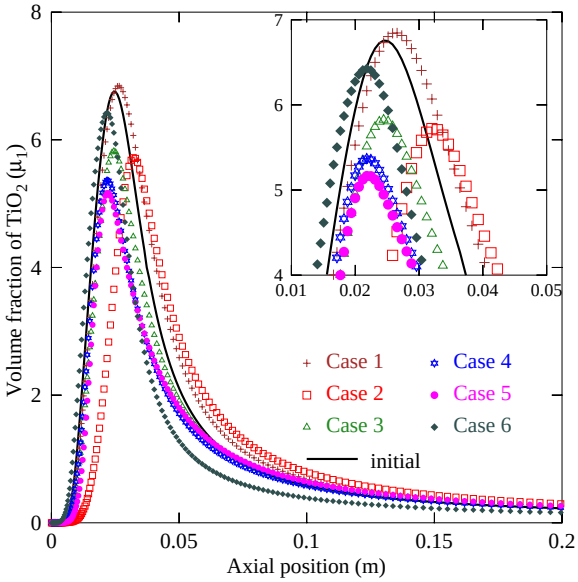

Figure 6.9: Comparison of the volume fraction profiles of TiO_2 (f_v, in ppm) along the burner axis close to the injection for all cases considered.

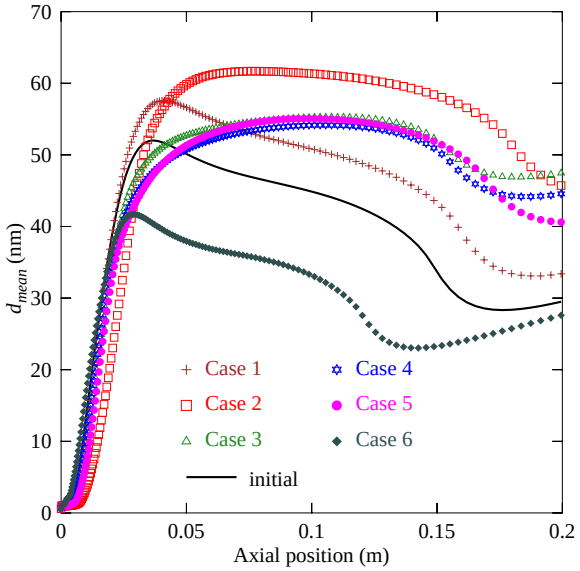

Figure 6.10: Comparison of the profiles of mean particle diameter (d_{mean}, in nm) along the burner axis close to the injection for all cases considered.

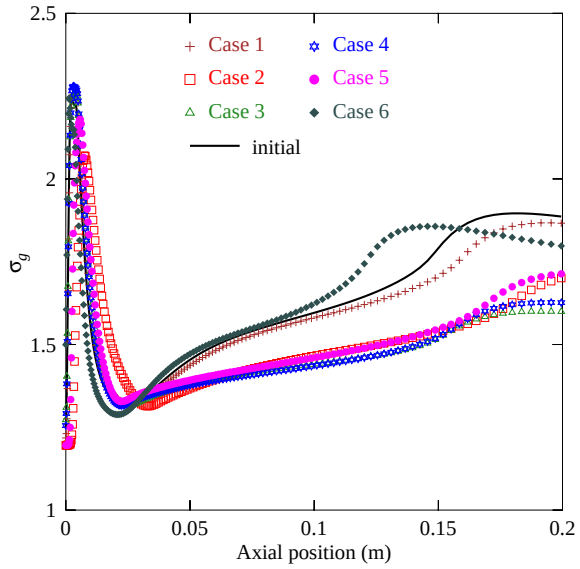

Figure 6.11: Comparison of the profiles of standard deviation (σ_g) along the burner axis close to the injection for all cases considered.

Chapter 7

Conclusions

The first objective of the present study was to develop an improved soot prediction model for turbulent non-premixed ethylene/air flames. Optimization relying on Genetic Algorithms coupled with evaluations of the solution by CFD coupled with DQMOM have been carried out for this purpose. The two objective functions of the optimization problem are the absolute differences concerning temperature (T) and soot volume fraction (f_v) as obtained by CFD and by published experiments. A sensitivity analysis revealed that the three main parameters describing the evolution of the soot particles are the activation temperature of nucleation T_n and of oxidation T_o, together with radiation constant C_0. They have therefore been chosen as parameters of the first optimization. The optimal parameter set identified by the procedure leads indeed to a considerable improvement for the target flame [50].

The generality of the optimal set of parameters has then been further tested by comparison with three additional flames, investigated experimentally in the literature. The results show a systematic improvement concerning the most important value for practical applications, i.e., the peak soot volume fraction. The temperature fields are also always improved. Nevertheless, even if the form of the axial profile for soot volume fraction also improves, it is however simultaneously shifted towards the burner.

To solve this undesirable shift, turbulence/chemistry coupling has been described in the final optimization step using a more accurate flamelet model. Optimization considering four model parameters of the particulate phase (in the final step, activation temperature of nucleation T_n, of oxidation T_o, of

particle growth T_g and radiation constant C_0) and two concurrent objective functions (for T and f_v evaluated similar to the earlier case) has been carried out successfully. The optimal parameter set finally identified by the procedure leads to a considerable improvement for all measured quantities. After optimization, the generality of the obtained models has been checked by computing further separate flames. A very good agreement is obtained for all cases, both for axial and radial profiles. As a consequence, the model combination presented in this work appears to be generally suitable for predicting soot formation in turbulent non-premixed ethylene/air flames.

Due to the tight coupling of soot particulate models with temperature it is necessary to take into account in a suitable manner radiative heat transfer. When computational costs are important, for instance when considering practical burners, only very simple models can be employed to describe radiation. In the present study, three such models have been considered. The importance of gas (CO_2 and H_2O) and soot radiation has been first shown. Using already optimized soot particulate models, the best possible radiation proportionality constant (C_0, C_1 and C_2) have been determined. The generality of the results has been checked. Unfortunately, it is observed that the previously employed Radiation model I can not be beaten by the alternative models II and III. All three models, being very similar in their structure, finally lead almost to the same optimum for the conditions considered here. Therefore, it appears that noticeable progress would only be possible by considering much more complex (and numerically expensive) models to describe radiative heat loss, since grey gas and optically thin approximation obviously constitute a major simplification of the true physics.

A numerical analysis of TiO_2 nanoparticle production has been carried out in the second part of this work, considering CH_4-O_2 diffusion flames with TTIP as precursor. Different combinations of flow configurations and burner geometries have been tested with the aim of obtaining nanoparticles with desired properties (minimum diameter d_{mean}, maximum volume fraction f_v and minimum width of the PSD σ_g). A detailed gas phase chemistry is taken into account with 17 species and 41 reactions. The EDC combustion model is used to handle turbulence-chemistry interaction. Aerosol evolution is tracked

with a population balance equation taking into account nucleation, molecular growth and aggregation. The Quadrature Method of Moments is used with two quadrature nodes to solve the PBE. Gas radiation and heat of reaction of TTIP decomposition have been taken into account. Initial test results performed for three different O_2 flow rates have been used to validate against experimental data from literature, adapting the EDC model parameters. Then, an optimal configuration is searched for, first by interchanging the fuel, oxidizer and carrier gas inlets. The initial configuration is found to be the most suitable to produce a stable flame. Selecting then this flow configuration and fixing the mass flow rates of CH_4, O_2, Ar and TTIP, geometric variations have been considered by increasing/decreasing the internal diameters (D_{1i}, D_{2i} and D_{3i}) of the diffusion burner by up to $\pm$ 20%. The numerical results carried out in 6 cases (Case 1 to Case 6) show a significant difference in temperatures, and therefore also in resulting particle properties. Case 1, initial configuration and Case 6 produce highest TiO_2 nanoparticle volume fraction, whereas mean particle diameter (d_{mean}) is lowest for Case 6. In the future, an automatic and concurrent optimization should be carried out in order to refine the analysis and to identify even better configuration.

Bibliography

[1] K. Wegner and S. E. Pratsinis, "Nozzle-quenching process for controlled flame synthesis of titania nanoparticles," *AIChE Journal*, vol. 49, no. 7, pp. 1667–1675, 2003.

[2] D. B. Kittelson, "Engines and nanoparticles: a review," *Journal of Aerosol Science*, vol. 29, no. 5-6, pp. 575–588, 1998.

[3] T. C. Bond, "Black carbon: Emission sources and prioritization," in *International Workshop on Black Carbon, London, UK*, 2009.

[4] E. Auer, A. Freund, J. Pietsch, and T. Tacke, "Carbons as supports for industrial precious metal catalysts," *Applied Catalysis A: General*, vol. 173, no. 2, pp. 259–271, 1998.

[5] UNEP and WMO, "Integrated assessment of black carbon and tropospheric ozone summary for decision makers," *Report: Integrated Assessment of Black Carbon and Tropospheric Ozone: Summary for Decision Makers*, 2011.

[6] V. Ramanathan, "Non-CO_2 emissions: Options for a way forward," *Black Carbon e-Bulletin*, vol. 1, pp. 1–4, July 2009.

[7] V. Ramanathan, "Black carbon & India." Environmental Ministry Meeting, New Delhi, India, Oct 2009.

[8] H. Wang, "Formation of nascent soot and other condensed-phase materials in flames," *Proceedings of the Combustion Institute*, vol. 33, no. 1, pp. 41–67, 2011.

[9] J. P. Cain, J. Camacho, D. J. Phares, H. Wang, and A. Laskin, "Evidence of aliphatics in nascent soot particles in premixed ethylene flames," *Proceedings of the Combustion Institute*, vol. 33, no. 1, pp. 533–540, 2011.

[10] D. Thévenin and G. Janiga, *Optimization and Computational Fluid Dynamics*. Springer, 2008.

[11] R. Hilbert, G. Janiga, R. Baron, and D. Thévenin, "Multi-objective shape optimization of a heat exchanger using parallel genetic algorithms," *International Journal of Heat and Mass Transfer*, vol. 49, pp. 2567–2577, 2006.

[12] G. Janiga and D. Thévenin, "Reducing the CO emissions in a laminar burner using different numerical optimization methods," *Journal of Power and Energy*, vol. 221, pp. 647–655, 2007.

[13] W. Stöber and U. R. Abel, "Lung cancer due to diesel soot particles in ambient air?," *International Archives of Occupational and Environmental Health*, vol. 68, pp. 3–61, 1996.

[14] J. J. Sauvain, T. V. Duc, and M. Guillemin, "Exposure to carcinogenic polycyclic aromatic compounds and health risk assessment for diesel-exhaust exposed workers," *International Archives of Occupational and Environmental Health*, vol. 76, pp. 443–455, 2003.

[15] V. Ramanathan and G. Carmichael, "Global and regional climate changes due to black carbon," *Nature Geoscience*, vol. 1, pp. 221–227, 2008.

[16] S. Menon, J. Hansen, L. Nazarenko, and Y. Luo, "Climate effects of black carbon aerosols in China and India," *Science*, vol. 297, pp. 2250–2253, 2002.

[17] Y. J. Kaufman and I. Koren, "Smoke and pollution aerosol effect on cloud cover," *Science*, vol. 313, pp. 655–658, 2006.

[18] M. Frenklach and H. Wang, "Aromatics growth beyond the first ring and the nucleation of soot particles," tech. rep., Department of Materials Science and Engineering, The Pennsylvania State University, 1991.

[19] H. Pitsch, E. Riesmeier, and N. Peters, "Unsteady flamelet modeling of soot formation in turbulent diffusion flames," *Combustion Science and Technology*, vol. 158, no. 1, pp. 389–406, 2000.

[20] F. Mauss, K. Netzell, and H. Lehtiniemi, "Aspects of modeling soot formation in turbulent diffusion flames," *Combustion Science and Technology*, vol. 178, pp. 1871–1885, 2006.

[21] L. Wang, D. C. Haworth, S. R. Turns, and M. F. Modest, "Interactions among soot, thermal radiation, and NOx emissions in oxygen-enriched turbulent nonpremixed flames: a computational fluid dynamics modeling study," *Combustion and Flame*, vol. 141, pp. 170–179, 2005.

[22] J. Appel, H. Bockhorn, and M. Wulkow, "A detailed numerical study of the evolution of soot particle size distributions in laminar premixed flames," *Chemosphere*, vol. 42, pp. 635–645, 2001.

[23] M. Balthasar, F. Mauss, M. Pfitzner, and A. Mack, "Implementation and validation of a new soot model and application to aeroengine combustors," *Journal of Engineering for Gas Turbines and Power*, vol. 124, no. 1, pp. 66–74, 2002.

[24] I. M. Aksit and J. B. Moss, "A hybrid scalar model for sooting turbulent flames," *Combustion and Flame*, vol. 145, pp. 231–244, 2006.

[25] D. O. Lignell, J. H. Chen, P. J. Smith, T. Lu, and C. K. Law, "The effect of flame structure on soot formation and transport in turbulent nonpremixed flames using direct numerical simulation," *Combustion and Flame*, vol. 151, pp. 2–28, 2007.

[26] G. Ma, J. Z. Wen, M. F. Lightstone, and M. J. Thomson, "Optimization of soot modelling in turbulent non-premixed ethylene/air jet flames," *Combustion Science and Technology*, vol. 177, pp. 1567–1602, 2005.

[27] F. Tao, V. I. Golovitchev, and J. Chomiak, "A phenomenological model for the prediction of soot formation in diesel spray combustion," *Combustion and Flame*, vol. 136, no. 3, pp. 270–282, 2004.

[28] B. S. Haynes and H. G. Wagner, "Soot formation," *Progress in Energy and Combustion Science*, vol. 7, pp. 229–273, 1981.

[29] H. Richter and J. B. Howard, "Formation of polycyclic aromatic hydrocarbons and their growth to soot: a review of chemical reaction pathways," *Progress in Energy and Combustion Science*, vol. 26, pp. 565–608, 2000.

[30] A. Zucca, D. L. Marchisio, A. A. Barresi, and R. O. Fox, "Implementation of the population balance equation in CFD codes for modelling soot formation in turbulent flames," *Chemical Engineering Science*, vol. 61, pp. 87–95, 2006.

[31] H. El-Asrag and S. Menon, "Large eddy simulation of soot formation in a turbulent non-premixed jet flame," *Combustion and Flame*, vol. 156, pp. 385–395, 2009.

[32] D. L. Marchisio and A. A. Barresi, "Investigation of soot formation in turbulent flames with a pseudo-bivariate population balance model," *Chemical Engineering Science*, vol. 64, pp. 294–303, 2009.

[33] A. Öncül, H. El-Rabii, and D. Thévenin, "Prediction of soot formation in non-premixed flames using DQMOM," in *International Conference on Multiphase Flow*, (Leipzig, Germany), pp. 67/1–67/7, 2007.

[34] R. Viskanta and M. P. Mengüc, "Radiation heat transfer in combustion systems," *Progress in Energy and Combustion Science*, vol. 13, no. 2, pp. 97–160, 1987.

[35] R. Siegel and J. R. Howell, *Thermal Radiation Heat Transfer*. Taylor and Francis, 1992.

[36] L. Wang, M. F. Modest, D. C. Haworth, and S. R. Turns, "Modeling nongray gas-phase and soot radiation in luminous turbulent non-

premixed jet flames," *Combustion Theory and Modelling*, vol. 9, pp. 479–498, 2005.

[37] S. C. Lee and C. L. Tien, "Effect of soot shape on soot radiation," *Journal of Quantitative Spectroscopy and Radiative Transfer*, vol. 29, pp. 259–265, 1983.

[38] R. Said, A. Garo, and R. Borghi, "Soot formation modeling for turbulent flames," *Combustion and Flame*, vol. 108, pp. 71–86, 1997.

[39] M. J. Zimberg, S. H. Frankel, J. P. Gore, and Y. R. Sivathanu, "A study of coupled turbulent mixing, soot chemistry, and radiation effects using the linear eddy model," *Combustion and Flame*, vol. 113, pp. 454–469, 1998.

[40] J. F. Widmann, "Evaluation of the Planck mean absorption coefficients for radiation transport through smoke," *Combustion Science and Technology*, vol. 175, pp. 2299–2308, 2003.

[41] K. Netzell, H. Lehtiniemi, and F. Mauss, "Calculating the soot particle size distribution function in turbulent diffusion flames using a sectional method," *Proceedings of the Combustion Institute*, vol. 31, pp. 667–674, 2007.

[42] J. Singh, M. Balthasar, M. Kraft, and W. Wagner, "Stochastic modeling of soot particle size and age distributions in laminar premixed flames," *Proceedings of the Combustion Institute*, vol. 30, no. 1, pp. 1457–1465, 2005.

[43] M. Celnik, R. Patterson, M. Kraft, and W. Wagner, "Coupling a stochastic soot population balance to gas-phase chemistry using operator splitting," *Combustion and Flame*, vol. 148, no. 3, pp. 158–176, 2007.

[44] J. Etheridge, S. Mosbach, M. Kraft, H. Wu, and N. Collings, "Modelling soot formation in a DISI engine," *Proceedings of the Combustion Institute*, vol. 33, no. 2, pp. 3159–3167, 2011.

[45] D. Grosschmidt, P. Habisreuther, and H. Bockhorn, "Calculation of the size distribution function of soot particles in turbulent diffusion flames," *Proceedings of the Combustion Institute*, vol. 31, pp. 657–665, 2007.

[46] A. Kazakov and M. Frenklach, "Dynamic modeling of soot particle coagulation and aggregation: Implementation with the method of moments and application to high-pressure laminar premixed flames," *Combustion and Flame*, vol. 114, pp. 484–501, 1998.

[47] M. Balthasar and M. Frenklach, "Detailed kinetic modeling of soot aggregate formation in laminar premixed flames," *Combustion and Flame*, vol. 140, pp. 130–145, 2005.

[48] R. McGraw, "Description of aerosol dynamics by the quadrature method of moments," *Aerosol Science and Technology*, vol. 27, pp. 255–265, 1997.

[49] D. L. Marchisio and R. O. Fox, "Solution of population balance equations using the direct quadrature method of moments," *Journal of Aerosol Science*, vol. 36, pp. 43–73, 2005.

[50] B. Yang, B. Hu, and U. O. Koylu, "Mean soot volume fractions in turbulent hydrocarbon flames: a comparison of sampling and laser measurements," *Combustion Science and Technology*, vol. 177, pp. 1603–1626, 2005.

[51] B. Yang and U. O. Koylu, "Detailed soot field in a turbulent nonpremixed ethylene/air flame from laser scattering and extinction experiments," *Combustion and Flame*, vol. 141, no. 3, pp. 55–65, 2005.

[52] J. H. Kent and D. Honnery, "Soot and mixture fraction in turbulent diffusion flames," *Combustion Science and Technology*, vol. 54, pp. 383–397, 1987.

[53] S.-Y. Lee, S. R. Turns, and R. J. Santoro, "Measurements of soot, OH, and PAH concentrations in turbulent ethylene/air jet flames," *Combustion and Flame*, vol. 156, pp. 2264–2275, 2009.

[54] P. Roth, "Particle synthesis in flames," *Proceedings of the Combustion Institute*, vol. 31, no. 2, pp. 1773–1788, 2007.

[55] P. V. Asharani, Y. Lianwu, Z. Gong, and S. Valiyaveettil, "Comparison of the toxicity of silver, gold and platinum nanoparticles in developing zebrafish embryos," *Nanotoxicology*, vol. 5, no. 1, pp. 43–54, 2011.

[56] M.-N. Croteau, A. D. Dybowska, S. N. Luoma, and E. Valsami-Jones, "A novel approach reveals that zinc oxide nanoparticles are bioavailable and toxic after dietary exposures," *Nanotoxicology*, vol. 5, no. 1, pp. 79–90, 2011.

[57] A. Sereemaspun, R. Rojanathanes, and V. Wiwanitkit, "Effect of gold nanoparticle on renal cell: An implication for exposure risk," *Renal Failure*, vol. 30, no. 3, pp. 323–325, 2008.

[58] D. E. Rosner, "Flame synthesis of valuable nanoparticles: Recent progress/current needs in areas of rate laws, population dynamics, and characterization," *Industrial & Engineering Chemistry Research*, vol. 44, no. 16, pp. 6045–6055, 2005.

[59] M. Yu, J. Lin, and T. Chan, "Numerical simulation of nanoparticle synthesis in diffusion flame reactor," *Powder Technology*, vol. 181, no. 1, pp. 9–20, 2008.

[60] S. E. Pratsinis, "Flame aerosol synthesis of ceramic powders," *Progress in Energy and Combustion Science*, vol. 24, pp. 197–219, 1998.

[61] Y. Xing, Ü. O. Köylü, and D. E. Rosner, "Synthesis and restructuring of inorganic nano-particles in counterflow diffusion flames," *Combustion and Flame*, vol. 107, pp. 85–102, 1996.

[62] K. Wegner, "Scale-up of nanoparticle synthesis in diffusion flame reactors," *Chemical Engineering Science*, vol. 58, no. 20, pp. 4581–4589, 2003.

[63] K. Wegner and S. E. Pratsinis, "Gas-phase synthesis of nanoparticles: scale-up and design of flame reactors," *Powder Technology*, vol. 150, pp. 117–122, 2005.

[64] H. Oha and S. Kim, "Synthesis of ceria nanoparticles by flame electrospray pyrolysis," *Journal of Aerosol Science*, vol. 38, no. 12, pp. 1185–1196, 2007.

[65] C. Janzen and P. Roth, "Formation and characteristics of Fe_2O_3 nanoparticles in doped low pressure H_2/O_2/Ar flames," *Combustion and Flame*, vol. 125, pp. 1150–1161, 2001.

[66] P. S. Fennell, J. S. Dennis, and A. N. Hayhurst, "The sampling of nanoparticles of MgO formed when doping an oxygen-rich flame with magnesium: The measurement of the concentrations and size-distributions of these nanoparticles," *Combustion and Flame*, vol. 151, pp. 560–572, 2007.

[67] S. Panda, D. Mishra, and A. Upadhyaya, "Effect of varying gas-flow conditions on the characteristics of the diffusion flame and silica powders prepared using flame combustion synthesis," *Powder Technology*, vol. 191, pp. 164 – 169, 2009.

[68] K. K. Akurati, A. Vital, U. E. Klotz, B. Bommer, T. Graule, and M. Winterer, "Synthesis of non-aggregated titania nanoparticles in atmospheric pressure diffusion flames," *Powder Technology*, vol. 165, pp. 73–82, 2006.

[69] H.-K. Ma and H.-A. Yang, "Combustion synthesis of titania nanoparticles in a premixed methane flame," *Journal of Alloys and Compounds*, vol. 504, no. 1, pp. 115–122, 2010.

[70] H.-K. Ma and H.-A. Yang, "A comparative study of TiO_2 nanoparticles synthesized in premixed and diffusion flames," *Journal of Thermal Science*, vol. 19, pp. 567–575, 2010.

[71] K. Wegner and S. E. Pratsinis, "Gas-phase synthesis of nanoparticles: scale-up and design of flame reactors," *Powder Technology*, vol. 150, no. 2, pp. 117–122, 2005.

[72] H. Zhao, X. Liu, and S. D. Tse, "Effects of pressure and precursor loading in the flame synthesis of titania nanoparticles," *J. Aerosol Sci.*, vol. 40, no. 11, pp. 919–937, 2009.

[73] P. Sunsap, D.-J. Kim, and K.-S. Kim, "Characterization of TiO_2 particles synthesized in diffusion flame reactor," *Industrial & Engineering Chemistry Research*, vol. 47, no. 7, pp. 2308–2313, 2008.

[74] A. Kowalik, P. Ifeacho, H. Wiggers, C. Schulz, and P. Roth, "TiO_2 nanoparticle formation in a premixed flame and a plasma reactor: Comparison between experiment and numerical simulation," in 3^{rd} *European Combustion Meeting*, 2007.

[75] T. Johannessen, S. E. Pratsinis, and H. Livbjerg, "Computational analysis of coagulation and coalescence in the flame synthesis of titania particles," *Powder Technology*, vol. 118, pp. 242–250, 2001.

[76] S. Tsantilis, H. K. Kammler, and S. E. Pratsinis, "Population balance modeling of flame synthesis of titania nanoparticles," *Chemical Engineering Science*, vol. 57, pp. 2139–2156, 2002.

[77] C. Artelt, H. J. Schmid, and W. Peukert, "Modelling titania formation at typical industrial process conditions: effect of surface shielding and surface energy on relevant growth mechanisms," *Chemical Engineering Science*, vol. 61, pp. 18–32, 2006.

[78] M.-Z. Yu, J.-Z. Lin, and T.-L. Chan, "Effect of precursor loading on non-spherical TiO_2 nanoparticle synthesis in a diffusion flame reactor," *Chemical Engineering Science*, vol. 63, no. 9, pp. 2317–2329, 2008.

[79] Y. Sung, V. Raman, and R. O. Fox, "Large-eddy-simulation-based multiscale modeling of TiO_2 nanoparticle synthesis in a turbulent flame reactor using detailed nucleation chemistry," *Chemical Engineering Science*, 2011. In Press.

[80] S. Tsantilis and S. E. Pratsinis, "Narrowing the size distribution of aerosol-made titania by surface growth and coagulation," *J. Aerosol Sci.*, vol. 35, no. 3, pp. 405–420, 2004.

[81] R. Fan, D. L. Marchisio, and R. O. Fox, "Application of the direct quadrature method of moments to polydisperse gas-solid fluidized beds," *Powder Technology*, vol. 139, no. 1, pp. 7–20, 2004.

[82] R. Fan and R. O. Fox, "Segregation in polydisperse fluidized beds: Validation of a multi-fluid model," *Chemical Engineering Science*, vol. 63, no. 1, pp. 272–285, 2008.

[83] L. Mazzei, "Limitations of quadrature-based moment methods for modeling inhomogeneous polydisperse fluidized powders," *Chemical Engineering Science*, vol. 66, no. 16, pp. 3628–3640, 2011.

[84] A. Zucca, D. L. Marchisio, M. Vanni, and A. A. Barresi, "Validation of bivariate DQMOM for nanoparticle processes simulation," *AIChE Journal*, vol. 53, pp. 918–931, 2007.

[85] R. Upadhyay and O. Ezekoye, "Treatment of size-dependent aerosol transport processes using quadrature based moment methods," *Journal of Aerosol Science*, vol. 37, no. 7, pp. 799–819, 2006.

[86] R. O. Fox, "Optimal moment sets for multivariate direct quadrature method of moments," *Industrial & Engineering Chemistry Research*, vol. 48, no. 21, pp. 9686–9696, 2009.

[87] D. L. Wright, R. McGraw, and D. E. Rosner, "Bivariate extension of the quadrature method of moments for modeling simultaneous coagulation and sintering of particle populations.," *Journal of Colloid and Interface Science*, vol. 236, no. 2, pp. 242–251, 2001.

[88] R. Fox, "Bivariate direct quadrature method of moments for coagulation and sintering of particle populations," *Journal of Aerosol Science*, vol. 37, no. 11, pp. 1562–1580, 2006.

[89] R. O. Fox, F. Laurent, and M. Massot, "Numerical simulation of spray coalescence in an eulerian framework: Direct quadrature method of moments and multi-fluid method," *Journal of Computational Physics*, vol. 227, pp. 3058–3088, 2008.

[90] M. Massot, F. Laurent, D. Kah, and S. de Chaisemartin, "A robust moment method for evaluation of the disappearance rate of evaporating sprays," *SIAM Journal on Applied Mathematics*, vol. 70, no. 8, pp. 3203–3234, 2010.

[91] D. E. Rosner and M. Arias-Zugasti, "Bivariate population balance model of ethanol-fueled spray combustors," *AIChE Journal*, 2011. In Press.

[92] A. Öncül, K. Sundmacher, A. Seidel-Morgenstern, and D. Thévenin, "Numerical and analytical investigation of barium sulphate crystallization," *Chemical Engineering Science*, vol. 61, no. 2, pp. 652–664, 2006.

[93] B. Wan and T. A. Ring, "Verification of SMOM and QMOM population balance modeling in CFD code using analytical solutions for batch particulate processes," *China Particuology*, vol. 4, pp. 243–249, 2006.

[94] S. Qamar, S. Mukhtar, Q. Ali, and A. Seidel-Morgenstern, "A gaussian quadrature method for solving batch crystallization models," *AIChE Journal*, vol. 57, no. 1, pp. 149–159, 2011.

[95] H. Wang and M. Frenklach, "Detailed reduction of reaction mechanisms for flame modeling," *Combustion and Flame*, vol. 87, no. 3-4, pp. 365–370, 1991.

[96] M. Frenklach, "Method of moments with interpolative closure," *Chemical Engineering Science*, vol. 57, no. 12, pp. 2229–2239, 2002.

[97] J. Appel, H. Bockhorn, and M. Frenklach, "Kinetic modeling of soot formation with detailed chemistry and physics: laminar premixed flames of C_2 hydrocarbons," *Combustion and Flame*, vol. 121, no. 1-2, pp. 122–136, 2000.

[98] J. Akroyd, A. J. Smith, R. Shirley, L. R. McGlashan, and M. Kraft, "A coupled CFD-population balance approach for nanoparticle synthesis in turbulent reacting flows," *Chemical Engineering Science*, 2011. In Press.

[99] M. Strumendo and H. Arastoopour, "Solution of PBE by MOM in finite size domains," *Chemical Engineering Science*, vol. 63, no. 10, pp. 2624–2640, 2008.

[100] M. Strumendo and H. Arastoopour, "Solution of population balance equations by the finite size domain complete set of trial functions method of moments (FCMOM) for inhomogeneous systems," *Industrial & Engineering Chemistry Research*, vol. 49, no. 11, pp. 5222–5230, 2010.

[101] M. Strumendo and H. Arastoopour, "Solution of bivariate population balance equations using the finite size domain complete set of trial functions method of moments (FCMOM)," *Industrial & Engineering Chemistry Research*, vol. 48, no. 1, pp. 262–273, 2009.

[102] D. Ramkrishna, *Population Balances: Theory and Applications to Particulate Systems in Engineering*. Academic Press, 2000.

[103] H. Hulburt and S. Katz, "Some problems in particle technology: A statistical mechanical formulation," *Chemical Engineering Science*, vol. 19, no. 8, pp. 555 – 574, 1964.

[104] V. John, I. Angelov, A. Öncül, and D. Thévenin, "Techniques for the reconstruction of a distribution from a finite number of its moments," *Chemical Engineering Science*, vol. 62, no. 11, pp. 2890 – 2904, 2007.

[105] L. de Souza, G. Janiga, V. John, and D. Thévenin, "Reconstruction of a distribution from a finite number of moments with an adaptive spline-based algorithm," *Chemical Engineering Science*, vol. 65, no. 9, pp. 2741 – 2750, 2010.

[106] D. L. Marchisio, J. T. Pikturna, R. O. Fox, R. D. Vigil, and A. A. Barresi, "Quadrature method of moments for population-balance equations," *AIChE Journal*, vol. 49, no. 5, pp. 1266–1276, 2003.

[107] D. L. Marchisio, R. D. Vigil, and R. O. Fox, "Quadrature method of moments for aggregation-breakage processes," *Journal of Colloid and Interface Science*, vol. 258, no. 2, pp. 322–334, 2003.

[108] D. L. Marchisio, R. D. Vigil, and R. O. Fox, "Implementation of the quadrature method of moments in CFD codes for aggregation-breakage problems," *Chemical Engineering Science*, vol. 58, no. 15, pp. 3337–3351, 2003.

[109] J. Sanyal, D. L. Marchisio, R. O. Fox, and K. Dhanasekharan, "On the comparison between population balance models for CFD simulation of bubble columns," *Industrial & Engineering Chemistry Research*, vol. 44, no. 14, pp. 5063–5072, 2005.

[110] D. L. Marchisio, *Quadrature Method of Moments for Poly-Disperse Flows*. Springer, 2007.

[111] R. O. Fox, "A quadrature-based third-order moment method for dilute gas-particle flows," *Journal of Computational Physics*, vol. 227, pp. 6313–6350, June 2008.

[112] C. Drumm, *Coupling of Computational Fluid Dynamics and Population Balance Modelling for Liquid-Liquid Extraction*. PhD thesis, Fachbereich Maschinenbau und Verfahrenstechnik der Technischen Universität Kaiserslautern, 2010.

[113] R. L. V. Wal, T. M. Ticich, and A. B. Stephens, "Can soot primary particle size be determined using laser-induced incandescence?," *Combustion and Flame*, vol. 116, no. 1-2, pp. 291–296, 1999.

[114] B. Hu, B. Yang, and U. O. Koylu, "Soot measurements at the axis of an ethylene/air non-premixed turbulent jet flame," *Combustion and Flame*, vol. 134, pp. 93–106, 2003.

[115] J. Reimann, S. A. Kuhlmann, and S. Will, "Improvement in soot concentration measurements by laser-induced incandescence (LII) through a particle size correction," *Combustion and Flame*, vol. 153, no. 4, pp. 650–654, 2008.

[116] A. Zucca, *Modelling of turbulence-chemistry interaction and soot formation in turbulent flames*. PhD thesis, Politecnico of Torino, 2005.

[117] D. Veynante and L. Vervisch, "Turbulent combustion modeling," *Progress in Energy and Combustion Science*, vol. 28, no. 3, pp. 193–266, 2002.

[118] S. B. Pope, "Simple models of turbulent flows," *Physics of Fluids*, vol. 23, no. 1, pp. 011301/1–011301/20, 2011.

[119] N. Peters, *Turbulent Combustion*. Cambridge University Press, 2000.

[120] F. Liu, H. Guo, G. J. Smallwood, and O. Gulder, "Effects of gas and soot radiation on soot formation in a coflow laminar ethylene diffusion flame," *Journal of Quantitative Spectroscopy and Radiative Transfer*, vol. 73, pp. 409–421, 2002.

[121] B. F. Magnussen, "On the structure of turbulence and a generalized eddy dissipation concept for chemical reaction in turbulent flow," in *19th AIAA Aerospace Science Meeting, St. Louis, Missouri*, 1981.

[122] R. O. Fox, *Computational models for turbulent reacting flows*. Cambridge University Press, 2003.

[123] M. Rehm, P. Seifert, and B. Meyer, "Theoretical and numerical investigation on the EDC-model for turbulence-chemistry interaction at gasification conditions," *Computers and Chemical Engineering*, vol. 33, no. 2, pp. 402–407, 2009.

[124] Ansys, *Ansys Fluent 12.0, Theory Guide*, 2009.

[125] B. F. Magnussen, "A model for flame extinction in turbulent flows," in *4th Symposium on Turbulent Shear Flows, Karlsruhe, Germany*, 1983.

[126] J. B. Moss, C. D. Stewart, and K. J. Young, "Modelling soot formation and burnout in a high temperature laminar diffusion flame burning under oxygen-enriched conditions," *Combustion and Flame*, vol. 101, pp. 491–500, 1995.

[127] F. Liu, H. Guo, G. J. Smallwood, and O. Gulder, "Numerical modelling of soot formation and oxidation in laminar coflow non-smoking and smoking ethylene diffusion flames," *Combustion Theory and Modelling*, vol. 7, pp. 301–315, 2003.

[128] C. Artelt, H. J. Schmid, and W. Peukert, "On the relevance of accounting for the evolution of the fractal dimension in aerosol process simulations," *Aerosol Science*, vol. 34, pp. 511–534, 2003.

[129] K. Okuyama, R. Ushio, Y. Kousaka, R. C. Flagan, and J. H. Seinfeld, "Particle generation in a chemical vapor deposition process with seed particles," *AIChE Journal*, vol. 36, no. 3, pp. 409–419, 1990.

[130] G. A. Battiston, R. Gerbasi, M. Porchia, and A. Gasparotto, "Metal organic CVD of nanostructured composite TiO_2-Pt thin films: A kinetic approach," *Chemical Vapor Deposition*, vol. 5, no. 1, pp. 13–20, 1999.

[131] N. Baguer, E. Neyts, S. Van Gils, and A. Bogaerts, "Study of atmospheric MOCVD of TiO_2 thin films by means of computational fluid dynamics simulations," *Chemical Vapor Deposition*, vol. 14, no. 11-12, pp. 339–346, 2008.

[132] A. Atreya and S. Agrawal, "Effect of radiative heat loss on diffusion flames in quiescent microgravity atmosphere," *Combustion and Flame*, vol. 115, no. 3, pp. 372–382, 1998.

[133] G. L. Hubbard and C. L. Tien, "Infrared mean absorption coefficients of luminous flames and smoke," *Journal of Heat Transfer*, vol. 100, pp. 235–239, 1978.

[134] H. Zhang and M. F. Modest, "Evaluation of the Planck-mean absorption coefficients from HITRAN and HITEMP databases," *Journal of Quantitative Spectroscopy and Radiative Transfer*, vol. 73, no. 6, pp. 649–653, 2002.

[135] S. Sazhin, "An approximation for the absorption coefficient of soot in a radiating gas," *Manuscript, Fluent Europe, Ltd*, 1994.

[136] T. Chittipotula, G. Janiga, and D. Thévenin, "Soot radiation models for turbulent nonpremixed ethylene/air flames," in *5th European Combustion Meeting, Cardiff, U.K.*, p. 367, 2011.

[137] R. Lindstedt, S. Louloudi, J. Driscoll, and V. Sick, "Finite rate chemistry effects in turbulent reacting flows," *Flow, Turbulence and Combustion*, vol. 72, pp. 407–426, 2004.